STUDIES OF THE MEASUREMENT OF TEMPERATURE IN SHOCK COMPRESSED CRYSTALLINE SOLIDS USING X-RAY DIFFRACTION

Ashley John Poole

Doctor of Philosophy

University of York

Physics

September 2019

Abstract

Temperature measurement in opaque laser-shocked solids is a long-standing research problem. The diagnosis of temperature using x-ray diffraction, in particular the Debye-Waller effect, has long been proposed as a potential solution, though no experimental measurement has ever been published. This thesis investigates the obstacles present in such a temperature measurement scheme.

A code was developed to efficiently analyse simulated x-ray diffraction patterns from molecular dynamics simulations so as to observe the Debye-Waller effect. This code was used to critically assess previous work performed in this area of research. It was found that material strength has a distinct impact on the behaviour of the Debye-Waller effect, though the impact on temperature measurement is minimal. It was also found that dislocations cause a significant error in temperature measurement, in conflict with the long-standing Wilkens theory of dislocations and x-ray diffraction.

An experiment was performed at the Orion laser facility to assess the experimental limits of Debye-Waller temperature measurement. The diffuse nature of the x-ray diffraction signal from shocked samples inhibited efforts to remove background while leaving signal intact. Brighter x-ray sources with narrower energy spectra are recommended to treat this problem.

Acknowledgements

My family are an endless source of encouragement. Their perspective has been invaluable over the past four years: their patience doubly so. Thank you for helping me see the bigger picture.

Finally, I will thank Annabel. Her extreme intellect and competence are inspiring. I am so thankful for her companionship.

Declaration

I declare that this thesis is a presentation of original work and I am the sole author. Much of the work would not have been possible without valuable contributions from others. Acknowledgement is always given when results derived by anyone but the author are reproduced. This work has not previously been presented for an award at this, or any other, University. All sources are acknowledged as References.

Contents

6

Chapter 1

Introduction

1.1 Matter under extreme conditions

The Earth's surface is composed of atomic material existing in a narrow range of pressure and temperature. The average human occupies a 1-atmospheric-pressure world. A climber on the summit of Mount Everest, usually aided by substantial breathing apparatus, survives in pressures of 0.33 atmospheres [1]. The scuba diving world record depth stands at 332 m [2], corresponding to a pressure of approximately 30 atmospheres. The climber and the diver represent the extreme boundaries of human pressure experience, a mere two orders of magnitude apart. The story is much the same regarding temperature; the highest and lowest temperatures experienced by most people are the products of their oven and fridge-freezer.

In stark contrast, the vast majority of matter in the universe exists in conditions totally alien to the human experience. Jupiter is thought to harbour diamond synthesising oceans of liquid methane [3] and the Sun's core temperature is in the

tens of millions of degrees [4]. These extreme conditions produce a dense plasma formed from the separation of nuclei from their electrons, constantly undergoing nuclear fusion.

The boundaries of human experience have shaped our civilisation. With a sliver of accessible materials, tools have been invented to extend and enrich life. In the modern era, materials science has expanded the breadth and depth of technologically relevant materials. The invention of semiconductors has brought with it an explosion of innovation, including electricity-generating photovoltaics and the ubiquitous home computer. Additionally, harnessed plasmas are an essential ingredient in the mass manufacture of computer chips. The microprocessor would not exist without plasmas and semiconductors, and so materials science is the vanguard of technology.

Before exotic states of matter can be of any use, they must first be understood. Since the conditions that generate these states are so far removed from the conditions at Earth's surface, their study demands considerable effort. This thesis concerns itself with solid materials created under high-pressures. The generation of these states in the lab will now be discussed.

1.2 Methods in high pressure solid state physics

The latter half of the twentieth century has seen much ground gained in the pursuit of lab-based high-pressure experiments. All methodologies can be grouped into either static or dynamic compression.

Static compression has the advantage of indefinite containment, allowing long timescale observations to be made. The premier tool for static compression is
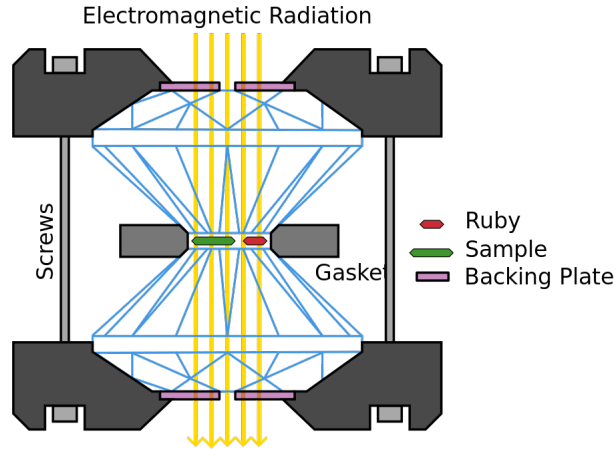
Figure 1.1: *The Diamond Anvil Cell (DAC). This image was created by Wikipedian Tobias1984 and is reproduced with permission under the GNU Free Documentation License.*

the diamond anvil cell (DAC). Two carefully cut slabs of diamond are assembled with a subject material clasped between, as in figure 1.1. A compressive force is delivered via a screw mechanism, causing the tapered ends of the diamonds to press into the sample. By inserting a small ruby alongside the material of interest, the pressure-sensitive ruby fluorescence can be probed and therefore used as a pressure sensor [5].

The DAC method has its drawbacks. The high pressures achieved can initiate undesirable diffusion between the diamond atoms and the sample. This can be counteracted somewhat by carefully coating the surface of the diamond with a diffusion-resistant layer [6]. Additionally, the whole system is very delicately balanced; temperature perturbations can destabilise the whole system, causing catastrophic failure. As a result DAC experiments are typically cooled to near-zero temperatures in order to reach high pressures. It is this method that resulted in the controversial

first observation of solid metallic hydrogen, at pressures over 500 GPa [7]. If the observation of higher pressures and temperatures is desired, a dynamic compression technique must be used.

The earliest dynamic compression techniques involved the detonation of explosives mounted on the side of materials. Through the use of an explosive lens, a planar compression wave is imparted to the sample. This setup was the primary method of generating high-pressure solids when the field was still in its infancy [8]. Perhaps the most spectacular variation of this technique uses nuclear explosives as the shock driving mechanism [9].

Later, gas gun experiments were fielded, launching high-speed projectiles into the sides of solid objects [10]. In this method, the projectile is loaded into a launch tube. Just behind the launch tube, a chamber of light gas is compressed by a piston. When the desired gas pressure is reached, the chamber is opened into the launch tube, accelerating the projectile into the sample. Due to an increase in deliverable energy density, this development allowed experimentalists to achieve pressures previously inaccessible with conventional explosives.

Non-impact compression schemes have been more recently developed. Pulsed power machines such as the Z accelerator were developed to compress materials radially by passing a large current through a metal cylinder [11]. The cylinder becomes ionised and the resulting Lorentz forces drive the cylinder inwards, crushing any material contained within. The cylindrical compression front results in higher peak pressures than can be achieved with planar shocks. This high degree of compression can be used to generate bright x-ray sources used for driving nuclear fusion experiments in the lab [12].

The final method of compression discussed here is laser shock compression [13]. The advent of high power lasers has opened up higher pressure ranges in the tens of TPa [14]. High power lasers impart their energy into a thin layer of material on a short timescale, typically of the order of nanoseconds. The surface of the irradiated material is ablated, driving a shock wave that traverses the sample. By arranging the lasers spherically, extremely high pressures can be generated; the pressures are such that heavy hydrogen fuel can be compressed to conditions necessary for nuclear fusion [15]. Due to their high energy densities, high power laser systems have been used to create states otherwise observed only in energetic astrophysical systems [16].

The subject of this thesis is concerned with the development of diagnostics capable of investigating solids under laser-shock compression. The following section discusses some current diagnostics commonly implemented on large laser systems.

1.3 Temperature measurement in laser shocked solids

High power laser investigations have exposed new phases of solid material otherwise inaccessible, though the timescale of the experiments is such that actually observing the material becomes challenging. The compressed state is only maintained for a short period of time of the order of a few nanoseconds, after which the high-pressure material rarefies [17, 18]. Specialised diagnostics are therefore required with the capability of making measurements in this small timing window.

Of particular interest are the thermodynamic state variables such as specific volume, pressure, and temperature. Measurements of these quantities leads to an

13

understanding of the material equation of state, revealing the relationships between the state variables. The equation of state can then be used to infer material characteristics [19]. While techniques indirectly measuring pressure and volume [20] are routine, methods of temperature measurement have largely been under-developed, especially in relation to opaque solids. The lack of a reliable temperature measurement has frustrated investigations into material equation of state [21].

The existing thermometry schemes are either limited by scope, practicality, or result in large measurement uncertainties. A selection of these thermometry techniques are discussed here, and their limitations discussed.

Extended X-ray Absorption Fine Structure (EXAFS)

When a photon is incident on a material it may be absorbed by a bound electron, which is then excited to a higher energy state. Whether the photon is absorbed is dependent on the energy of the photon and the difference in energy between electronic states. Once a photon has the required energy to promote an electron, the tendency of the material to absorb the photon increases dramatically. This sudden increase in absorption gives rise to an absorption edge. When a photon liberates a core electron from an atom, the photoelectron will go on to interact with neighbouring atoms. These neighbouring atoms act as scatterers, and so the backscattered photoelectron can interact with its own wavefunction. This self interaction gives rise to energy dependent oscillations, known as fine structure [22]. Since temperature causes atoms to move from their lattice sites, the character of this self-interaction is altered and observed as changes in fine structure. This is the basis of the EXAFS thermometry technique used in laser-shock experiments, though

14

uncertainty in the measurement often exceeds 50% [23].

Streaked Optical Pyrometry (SOP)

SOP is a mature temperature measurement technique, though its scope is limited to strongly radiating materials at high temperatures [24]. When a shock wave passes through a sample, the shocked material self-emits [25]. The spectrum of emitted radiation is compared to a Plankian spectrum to infer temperature [26].

This method has been used successfully on materials with high transmission [27], but for materials that are largely opaque, such as metals, the optical skin-depth is typically much less than 100 nm [28]. This restricts use of the technique to transparent materials (such as quartz or NaCl), or to backscatter measurements from material surfaces. The accuracy of the technique is dependent upon knowledge of the emissivity of the material, which is often unknown. Additionally, many transparent media undergo phase transitions to opaque states at high pressures, further limiting the technique [5].

Raman Scattering

Raman scattering can be used to measure the temperature of shocked materials by analysing the vibrational properties of the sample [29]. A laser, typically in the visible spectrum, is shone on the target and the spectrum of transmitted or backscattered light is analysed; here, backscattered refers to photons that are reflected from the sample and detected on the same side of the sample as the incident beam. The spectrum will show one large central peak called the Rayleigh line, produced by elastically scattered radiation, and many more peaks offset from the Rayleigh line.

These offset peaks, known as Stokes and anti-Stokes lines, are caused by interactions between the incident photons and the vibrational energy states of the material. When a photon is incident upon the material, it may be absorbed by a phonon and subsequently re-emitted when the phonon de-excites. If the phonon is in its ground state when it absorbs a photon, it may de-excite to an energy level above ground state, resulting in the emission of a photon at a lower frequency than the incident radiation. This radiation manifests as a Stokes line in the Raman spectrum. Similarly, the phonon may initially be in an excited state, and after excitation may decay to the ground state, emitting a photon of higher energy. Emissions of this type present as anti-Stokes lines in the Raman spectrum.

For temperature measurement, the most commonly used technique simply looks at the intensity ratio of the anti-Stokes lines to Stokes lines. This ratio contains information about the temperature-dependent occupation of vibrational states within the material [30], although more sophisticated methodologies are also in use [31].

The accuracy of the technique is dependent on knowledge of the emissivity of the material being probed. What's more, bulk temperatures can only be obtained from transparent materials. In the case of opaque solids, only the edge temperature is measured; since the edge temperature of a material is not reliably linked to bulk temperature on laser shock timescales, this technique is incompatible with high power laser experiments involving opaque solids.

Neutron Resonance Spectroscopy (NRS)

NRS uses temperature sensitive nuclear transitions of heavy elements to measure temperature [32, 33]. It involves the bombardment of a material with neutrons of

16

energies 1 - 100 eV. At these energies, many nuclei exhibit resonant states. The incident neutron is absorbed by the nucleus, forming a compound nucleus, which then re-emits the neutron with an altered energy. The neutron resonance peaks will be Doppler shifted by a certain amount, providing a velocity distribution which is then linked to temperature. NRS has been used to successfully measure the temperature of W-doped Mo which has been shock compressed with an explosively driven flyer plate; the temperature was measured with an error of approximately 4% [34].

Neutron beams are typically inconvenient to work with, requiring infrastructure that is not usually available at a large laser facility. Laser generated neutron beams exist [35], and intentions have been stated to use such beams on laser shock experiments [36], but no results are published demonstrating the implementation of NRS on a high power laser experiment. In addition, the technique is mostly applicable to heavier metals with high proton number, ruling out the majority of materials of interest; materials of interest are typically lower mass metals such as Cu and Fe. The use of NRS on doped materials has been performed [34], but the effect of such doping may significantly alter the behaviour of the shocked material.

1.4 X-ray diffraction as a temperature diagnostic

None of the above techniques are currently suitable for the routine measurement of temperature in opaque laser-shocked solids. In this thesis, it is proposed that a technique involving x-ray diffraction may be suitable. The intensities of diffracted x-rays are dependent on temperature via the Debye-Waller effect, as will be discussed

in section 2.3.2. The exploitation of the Debye-Waller effect as a temperature measurement tool on laser-shock experiments has previously been proposed [37], though no experiment has ever been published showing its implementation.

The success of such a technique would mark a critical improvement in capability. Still outstanding are major questions surrounding the suitability of the technique to laser-shock experiments; these questions will be discussed in chapter 3. An experiment especially designed to test this technique is also required; this is the subject of chapter 4. The overall purpose of this thesis is to explore the limitations of the Debye-Waller effect and investigate its applicability to temperature measurement on high power laser facilities. The strengths and weaknesses of the technique will be highlighted and its suitability for laser-driven experiments adjudicated.

1.5   Thesis structure and the role of the author

The thesis is structured as follows, with acknowledgement given to contributors and collaborators where appropriate.

Chapter 2: Background Theory and Previous Work

This chapter lays the theoretical groundwork necessary for an understanding of the work undertaken in this thesis. All theory written in this section is drawn from previous work by others. Many images in this section were created by others and are reproduced with permission. Whenever an image is reproduced or altered, credit is appropriately given to the creator.

Chapter 3: Molecular Dynamics Simulations of Temperature Measurement using the Debye-Waller Effect

This chapter presents computational work undertaken by the author. A code written by Andrew Higginbotham was used to generate x-ray diffraction patterns. An analysis code was written by the author to reliably and efficiently analyse the Debye-Waller effect.

Chapter 4: Experimental Investigation of Temperature Measurement using the Debye-Waller Effect

An experiment was designed and led by the author, with substantial assistance from many other scientists. The main collaborators were Andrew Higginbotham, John Foster, David McGonegle, Andrew Comley, Steve Rothman, Emma Floyd, Anthony Meadowcroft, Caroline Lumsdon, and Justin Wark. The x-ray spectrum used in section 4.3.1 was made by Anthony Meadowcroft. The HYADES simulations in section 4.4 were performed by David McGonegle. The analysis of the experimental diffraction data was undertaken solely by the author, with the exception of section 4.6.2, which made use of a code written by Andrew Higginbotham, and section 4.6.7, which was heavily informed by the work of John Foster.

Chapter 5: Conclusions and Future Work

A summary of the main results of the full thesis are given here. Recommendations are given regarding the applicability of the Debye-Waller thermometry technique and suggestions are made for future implementations.

Chapter 2

Background Theory and Previous Work

The subject of this thesis is the use of x-ray diffraction to measure temperature in crystalline solids undergoing laser-shock compression. As with any work of science, this thesis benefits from the efforts of individuals that went before. The underlying theory, developed largely throughout the twentieth century, is laid out here so as to set the stage for the new work undertaken by the author. The relevant fields are solid state physics, shock-wave physics, x-ray crystallography, and computational molecular dynamics.

2.1   The crystalline structure of elemental solids

Solids typically come in two forms: amorphous, and crystalline. Amorphous solids are ordered in the short range by maintaining energetically favourable inter-atomic

(or molecular) distances, but they do not show any long range order. This is in contrast to crystalline solids which are composed of atoms and molecules arranged in a regular periodic fashion. This thesis is concerned with crystalline solids and so amorphous solids will not be discussed further.

A lattice is a set of points periodically arranged in space [38], as shown in fig 2.1. The origin may be defined at any point in the lattice. Positions within the lattice are described using a set of lattice vectors. A set of lattice vectors are said to be primitive if any integer combination of the lattice vectors, starting at the origin, will reproduce the whole lattice. Alternatively, the volume enclosed by the primitive lattice vectors, called the primitive unit cell, will contain exactly 1 lattice point. It is often more useful to define the lattice by a non-primitive set of vectors, called conventional lattice vectors. On the right hand side of figure 2.1, the conventional lattice vectors $\mathbf{a}_1$, $\mathbf{a}_2$, and $\mathbf{a}_3$ all conveniently coincide with the edges of the cube, but the number of lattice points enclosed within this conventional unit cell is 2. A potential primitive basis of vectors for this lattice might be $\mathbf{a}_1$, $\mathbf{a}_2$, and $\mathbf{p}_3$.

For any set of primitive lattice vectors $\mathbf{a}_1$, $\mathbf{a}_2$, and $\mathbf{a}_3$, the position of all lattice points relative to the origin can be written

$$\mathbf{r} = u\mathbf{a}_1 + v\mathbf{a}_2 + w\mathbf{a}_3 \tag{2.1}$$

where u, v, w are integers. Once the lattice is defined, the lattice points can be substituted with a set of atoms called a basis. By replacing every lattice point with the basis, the full crystal is generated.

A large number of crystalline structures are possible. The structure a particular material occupies is the result of a minimisation of free energy of the lattice, although

21
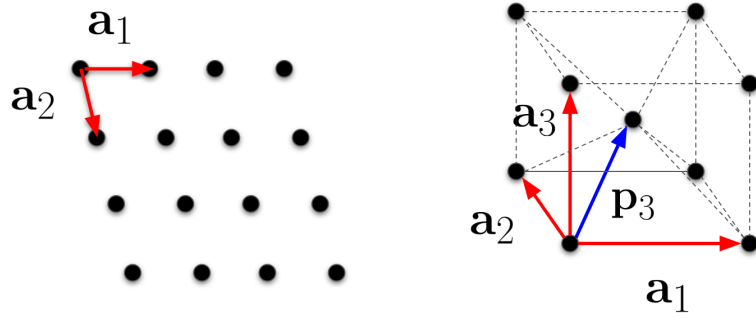
Figure 2.1: *A 2-dimensional lattice is shown on the left with lattice vectors a_1 and a_2. On the right is a 3-dimensional lattice. By the application of a basis to each lattice site, a full crystal structure is generated.*

a generally applicable prediction method is surprisingly elusive [39]. A number of structures are possible at the same pressure-temperature conditions due to the presence of multiple energy minima in the thermodynamic landscape. The stable existence of a structure at a local minima, but not the global minimum, is called metastability. The ability of a material to occupy different solid phases under identical conditions is called structural polymorphism. A famous example of this is elemental carbon, which can exist both as graphite and diamond under ambient conditions. Under the right conditions of temperature and pressure, crystals will undergo solid-solid phase transitions, swapping the previous structure for a new energetically favourable structure [40, 41, 42]. In the case of elemental crystalline solids, the number of possible structures is greatly simplified by the presence of a single type of atom.

In this section a selection of purely elemental cubic structures are described alongside their significant geometric characteristics. Only cubic structures are treated since other types of structure are not relevant to the present work, though much of

the following discussion is also applicable to non-cubic structures. The crystalline nature of solids results in vibrational properties that are central to the temperature measurement technique employed in this thesis. Finally, the change of the vibrational properties of a solid under compression are considered.

2.1.1 Cubic crystal structures

Many structures are said to be cubic; that is, they are easily conceptualised as a set of atoms arranged about a single cube. The cube can then be tessellated along x, y, and z to create an infinite periodic structure, or a crystal. The lattice constant a of a cubic solid is defined as the side length of the cube used to visualise the structure.

The simple cubic (SC) structure is depicted in figure 2.2. The SC structure is rare amongst elemental solids at standard temperature (0 °C) and pressure (1 Atm), though polonium takes this form [43]. In cubic structures the conventional lattice vectors are defined along the edges of the cube for convenience:

$$\mathbf{a_1} = [a, 0, 0] \tag{2.2}$$

$$\mathbf{a_2} = [0, a, 0] \tag{2.3}$$

$$\mathbf{a_3} = [0, 0, a] \tag{2.4}$$

By translating the unit cell by all possible integer sums of the lattice vectors, the full infinite crystal can be constructed. The lattice vectors can be normalised by dividing each vector by a to give

$$\mathbf{a_1}' = [1, 0, 0] \tag{2.5}$$

$$\mathbf{a_2}' = [0, 1, 0] \tag{2.6}$$

$$\mathbf{a_3}' = [0, 0, 1] \tag{2.7}$$

This convention is useful for discussing positions within the unit cell in general terms. A vector is now assigned to each of the atoms constituting the structure; in the case of a SC material, there is only one atom to define, which is found at $[0, 0, 0]$. Note how the atoms in the other corners are not specified; it is intended that by tessellating the basis along every integer combination of the lattice vectors the entire crystal can be generated. If the other corner atoms were specified, every atom would be generated multiple times at each location upon tessellation.

A more commonly observed structure is the body-centred cubic (BCC) structure. It is similar to the simple cubic structure, except now an additional atom is placed at the centre of the the cube, as depicted in fig 2.2. The atoms are found at $[0, 0, 0]$ and $[\frac{1}{2}, \frac{1}{2}, \frac{1}{2}]$. Examples of elements inhabiting this structure are iron, tantalum, and niobium.

Another commonly observed cubic structure is the face-centred cubic (FCC) structure. It can again be thought of as an augmented simple cubic structure, but this time the additional atoms are located in the centre of each face of the cube. The structure is also depicted in figure 2.2. The FCC structure is a close-packed structure; close-packed structures exhibit the most volume efficient packing of spheres. Spheres are efficiently packed when they are arranged in hexagonal layers, as in figure 2.3. There are multiple ways of stacking these layers. The base layer is referred to as
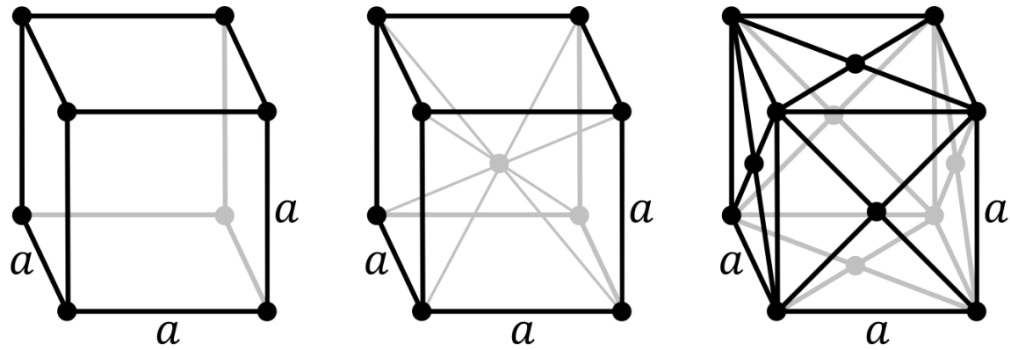
Figure 2.2: *The unit cells of three cubic crystalline structures, from left to right: simple cubic; body-centred cubic; face-centred cubic. These images were created by the Wikipedians Daniel Mayer and DrBob. They are reproduced here with permission under the Creative Commons Public License.*

layer A; a second layer B can be placed above A with atoms positioned between the atoms of A. The third layer can either be placed exactly overlapping layer A (creating an ABA structure, known as hexagonal close packed) or it can be placed such that the atoms do not overlap with either A or B; in this case the layering is ABC, and the structure produced is FCC. Common examples of elements with the FCC structure are copper, gold, and silver.

The structures discussed above are all examples of single crystals. Most natural materials do not take this form and are instead polycrystalline. Polycrystalline materials simply contain many small single crystal regions, called grains. These grains are packed together in a single sample, typically resulting in a patchwork composition of many different crystalline orientations.
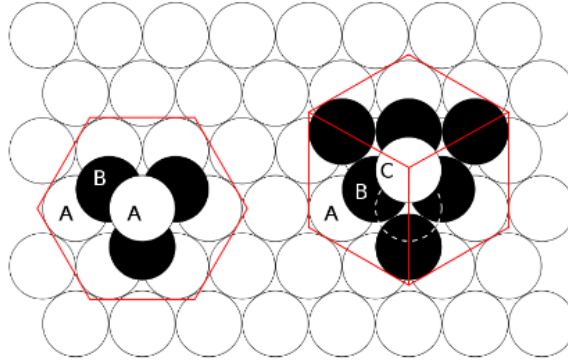
Figure 2.3: *Close-packed spheres consist of hexagonal layers. Two methods of stacking the hexagonal layers are shown; on the left is the hexagonal close packed (HCP) structure, and on the right is the FCC structure. This image was created by the Wikipedian Twisp. The image exists in the public domain and is reproduced here with permission.*

2.1.2   Crystal imperfections

Crystalline solids are rarely perfect in form. The lattice is often disrupted by imperfections known collectively as defects [44]. Defects come in many forms and each type has a different effect on the resulting material properties. Defects can be grouped by dimensionality into point defects, line defects, and plane defects. The lattice is distorted to the largest degree in the immediate vicinity of the defect; atoms that are far away from a defect are therefore screened from the distortions.

An example of a point defect is a vacancy, where an atom is simply missing from its usual structural position. The atoms around the vacancy relax into the space left by the missing atom, which causes a distortion of the structure in the vicinity of the void. Alternatively, an interstitial defect is formed when one or more atoms occupy additional non-structural positions. These interstitial atoms stiffen the crystal in the vicinity.

Line defects almost always take the form of dislocations [45]. Dislocations come in two flavours: edge dislocations and screw dislocations. Illustrations are presented in figure 2.4. An edge dislocation can be visualised by imagining a stack of paper; if a half of a piece of paper is now inserted into the stack, the stack of paper will be most noticeably disrupted at the centre of the stack. In an edge dislocation, the edge of the half-sheet of paper corresponds to the dislocation core. The crystal lattice is maximally distorted near the dislocation core.

A screw dislocation can be visualised with a stack of paper that is cut vertically, from the centre of the stack to the edge, resulting in two "legs" for each sheet. One of the stacks of legs is moved upwards by one sheet, so that each leg is now in line with the opposing leg of the next sheet. The result is a helical structure in the centre of the stack, propagating from top to bottom. In the case of a screw dislocation, the core runs vertically through the crystal. Again, the lattice is most distorted near the dislocation core.

The line vector $\mathbf{l}$ is oriented along the axis of the dislocation core. On its own, this is an incomplete description. A dislocation can be more fully described by including some measure of the lattice mismatch produced by the dislocation. In figure 2.4 a closed path MNOP is drawn on the initial crystal; this closed path consists of a series of translations. When the dislocation is present, the same series of translations no longer produces a closed circuit. In order to close the circuit, an additional translation must be introduced. This translation is called the Burgers vector $\mathbf{b}$, and it represents the lattice mismatch introduced by a dislocation. For an edge dislocation, $\mathbf{b}$ is perpendicular to $\mathbf{l}$, whereas for a screw dislocation, $\mathbf{b}$ is parallel to $\mathbf{l}$. In reality most dislocations manifest as a mixture of these two types

27
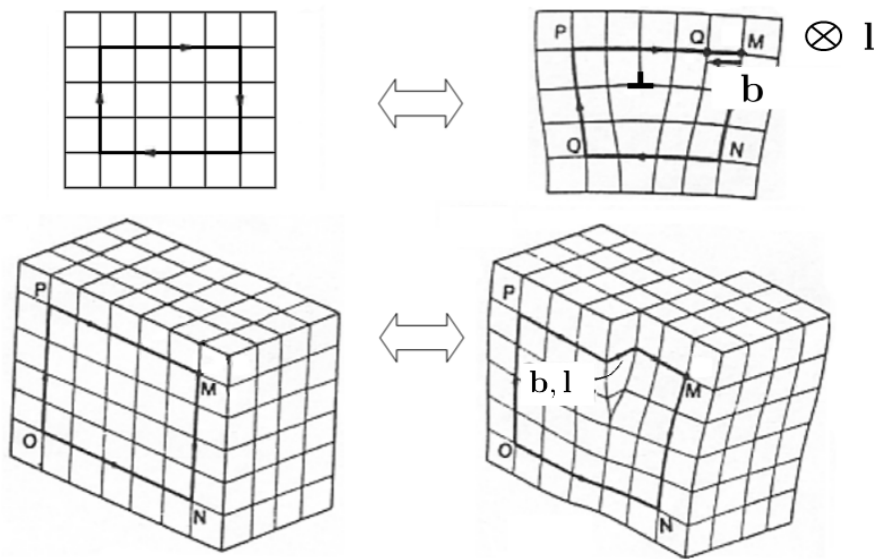
Figure 2.4: *An edge dislocation (upper) and a screw dislocation (lower). On both images a comparison is drawn between the perfect crystal and the dislocated crystal. The burgers vector of each dislocation is shown, as well as an example line vector. In the case of the edge dislocation, the line vector is shown entering the page. This image was created by Javier Bartolom Vlchez and is reproduced here with permission under the GNU Free Documentation License.*

of dislocation. They are said to have edge character and screw character, and the orientation between **b** and **l** is somewhere between perpendicular and parallel.

Dislocations can form in a number of ways. The spontaneous formation of dislocations in a perfect crystal is called homogeneous nucleation. This pathway is incredibly energetic, since a whole line of atomic bonds has to be broken and as a result this formation pathway is unlikely under normal conditions. Under shock conditions, however, homogeneous nucleation occurs at the boundary between shocked and unshocked material [46]. This occurs as a result of the large uniaxial pressures caused by the passage of a shock wave, as well as the lattice mismatch
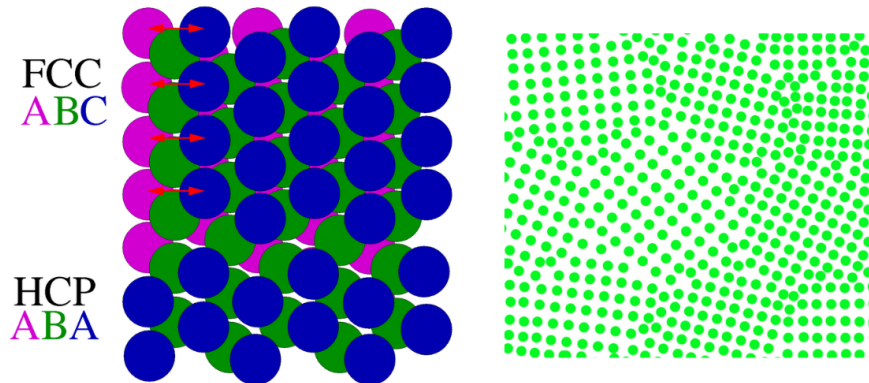
Figure 2.5: *Two types of planar defect are shown. On the left is a stacking fault, where the order of atomic layers is disrupted. On the right is a 2-dimensional representation of a grain boundary. These images were created by Gerolf Ziegenhain and Edward Pleshakov; they are reproduced here with permission under the GNU Free Documentation License.*

between compressed and uncompressed material. Another dislocation source is at the boundary between crystallites in a polycrsytalline material. The lattice mismatch of the surfaces between crystallites often result in the formation of a dislocation that propagates through the crystal. A similar effect is present at the edge of a material, though this is less relevant to polycrystalline materials.

An example of a plane defect is a stacking fault. These are formed when the order in which planes of atoms are stacked is altered. An example situation might involve an FCC metal, with stacking order ABCABCABC. A stacking fault has occurred if the plane order is now ABC<u>ABA</u>BC; the lattice now contains a component of hexagonal close packed structure. Another planar defect is caused by the mismatch of crystallite grains within a polycrystalline material. These boundaries between grains typically do not match up perfectly; the lattice mismatch therefore causes a distortion of the crystal structure in the vicinity of the grain boundary.

Defects play an important role in the properties displayed by a material. For example, the movement of dislocations when a crystal is exposed to high pressures is the medium of plasticity in a material [47]. Without dislocation movement, metals are not malleable. If dislocations were not there to alleviate applied pressures, a material would elastically compress until sudden catastrophic failure.

2.1.3   Crystalline directions, planes, and their significance

The arrangement of atoms has consequences for the overall properties of a material. Certain directions within a crystal will be associated with interesting phenomena, such as the onset of a structural phase transformation, or the stimulation of certain defect formation mechanisms. In cubic materials, directions are defined using the same Cartesian vector convention used in equations 2.5, 2.6, 2.7.

The $\mathbf{a_1}\prime = [1\ 0\ 0]$ direction in an SC, FCC, or BCC structure is symmetrically related to the $\mathbf{a_2}\prime$ direction. The interatomic distance is exactly the same along both $\mathbf{a_1}\prime$ and $\mathbf{a_2}\prime$; in fact the two atomic chains are indistinguishable from one another. This symmetry is important since the resultant behaviour of the atoms along both of these directions will be the same, given the same stimulus. Note that in crystallography, the type of bracket used has a precise meaning; a square bracket is used to represent a direction. Directions can be grouped into families according to their symmetry; in the case of the $\mathbf{a_1}\prime$ direction, the family of directions is denoted by $< 1\ 0\ 0 >$. Note that this is equivalent to $< 0\ 1\ 0 >$ and $< 0\ 0\ 1 >$. In addition, a line over a number indicates a negative value, so the family $< \bar{1}\ 0\ 0 >$ is written instead of $< -1\ 0\ 0 >$.

Another useful geometrical concept for crystalline solids is that of crystal planes.

A plane is described by the intersection it makes with the unit cell as shown in fig 2.6. The plane intersects the lattice vectors at the points $\frac{\mathbf{a_1}}{h}$, $\frac{\mathbf{a_2}}{k}$, and $\frac{\mathbf{a_3}}{l}$, where h, k, and l are known as the Miller indices. If the plane runs parallel to a lattice vector the intersection occurs at infinity, and so the Miller index for that lattice vector is 0. Once the intersections are established, the plane is then labelled $(h\ k\ l)$. Notice that this does not define a single plane; in fact the Miller indices define a set of parallel planes. These planes are all separated a set distance d apart. In cubic crystals, the interplanar distance is calculated as

$$d = \frac{a}{\sqrt{h^2 + k^2 + l^2}} \tag{2.8}$$

In the same way that families of directions can be defined, so too can families of planes. Take for example the $(0\ 0\ 1)$ and $(1\ 0\ 0)$ planes. When observed in isolation these planes look identical. They can therefore be grouped together; in this case the family of planes is written $\{1\ 0\ 0\}$. The number of symmetrical planes in a plane family is known as multiplicity, and it differs between plane families. To construct a list of multiplicities for a family of planes $\{h\ k\ l\}$, one must find every unique 3-component permutation of h, k, l, $\bar{h}$, $\bar{k}$, $\bar{l}$. For example, $\{1\ 0\ 0\}$ contains the planes $(1\ 0\ 0)$, $(0\ 1\ 0)$, $(0\ 0\ 1)$, $(\bar{1}\ 0\ 0)$, $(0\ \bar{1}\ 0)$, $(0\ 0\ \bar{1})$, and so the multiplicity is 6. The maximum possible multiplicity occurs when $h \neq k \neq l \neq 0$; in this case the multiplicity is 48. An example of a plane family that meets this condition is $\{1\ 2\ 3\}$. Curated lists of multiplicities in BCC and FCC structures are given in appendices A and B respectively.
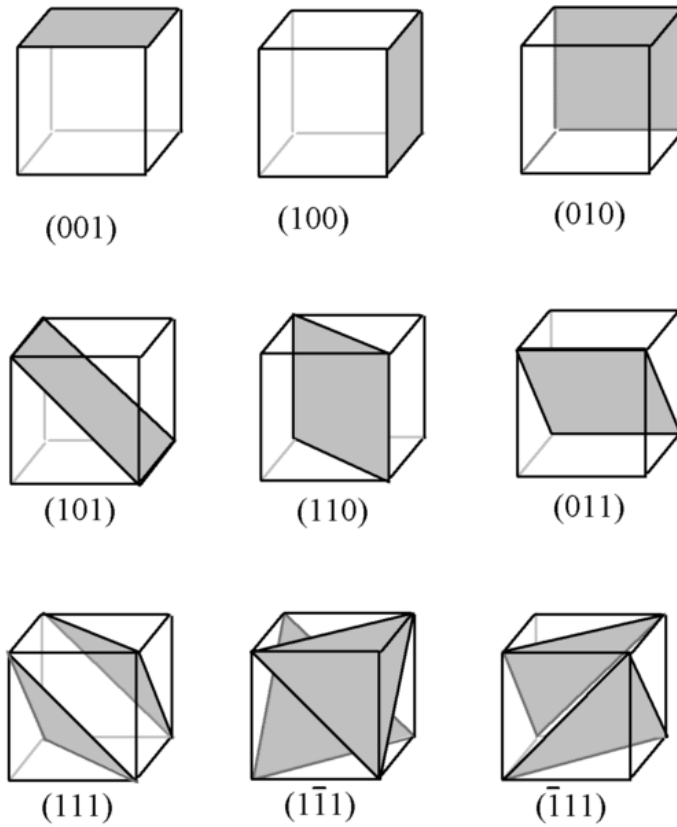
Figure 2.6: *A selection of commonly occurring planes in cubic structures. This image was created by Christophe Dang Ngoc Chan and is reproduced with permission under the GNU Free Documentation License.*

2.1.4   The reciprocal lattice

The Miller indices have a greater significance. The crystal lattices described in section 2.1.1 are given in terms of the three lattice vectors $\mathbf{a_1}$, $\mathbf{a_2}$, $\mathbf{a_3}$. These vectors can be manipulated to produce a new set of vectors, called the reciprocal lattice vectors [48].

$$\mathbf{b_1} = \frac{\mathbf{a_2} \times \mathbf{a_3}}{\mathbf{a_1} \bullet \mathbf{a_2} \times \mathbf{a_3}} \tag{2.9}$$

$$\mathbf{b_2} = \frac{\mathbf{a_3} \times \mathbf{a_1}}{\mathbf{a_1} \bullet \mathbf{a_2} \times \mathbf{a_3}} \tag{2.10}$$

$$\mathbf{b_3} = \frac{\mathbf{a_1} \times \mathbf{a_2}}{\mathbf{a_1} \bullet \mathbf{a_2} \times \mathbf{a_3}} \tag{2.11}$$

As with the real space lattice vectors, the reciprocal lattice vectors can be translated over every integer combination to produce an infinite lattice.

The vector that goes from the origin to any of the integer transformations is given the symbol $\mathbf{G}$.

$$\mathbf{G_{hkl}} = h\mathbf{b_1} + k\mathbf{b_2} + l\mathbf{b_3} \tag{2.12}$$

Here, h k and l are the same Miller indices used when defining planes in section 2.1.3. This is because the reciprocal lattice of a crystal structure is a representation of crystal planes.

The reciprocal lattice vectors presented above are valid for a single crystal. In the case of a polycrystal, the reciprocal lattice is an overlapping of all the reciprocal lattices of the constituent grains. For a sufficient number of grains, the reciprocal space representation is no longer a set of discrete points, but is instead complex object.

2.1.5 Crystallographic texture

As previously stated, most materials are not single crystal in nature. Instead they tend to be polycrystalline. The simplest polycrystal may be thought of as a powder consisting of grains oriented in a uniformly random manner. In such a powder, there is no preferential orientation of grains.

Most polycrystalline solids are not ideal powders. Instead the materials exhibit some preference to certain orientations. This preference arises from the mechanical pathway that produced the material. For example, if a sample is grown on a crystalline surface the orientation of crystals in the surface will seed the orientation of the growing crystal. This new crystal will similarly seed another preferred orientation on any subsequent crystals. A material that exhibits such orientational preferences is said to be textured.

The texture of materials, particularly industry relevant metals such as iron, has been well studied. The relative orientations of grains within a material are described using an orientation distribution function (ODF) [49]. The ODF is a four-dimensional mathematical object that describes fully the orientations present within a material; three dimensions define the orientation, and the fourth dimension describes the prevalence of that orientation.

To generate an ODF each crystal orientation is prescribed a set of relative Euler angles. The Euler angles, shown in figure 2.7, are defined as follows. A vector is first rotated about the z-axis by an angle α. The whole Cartesian system is also rotated with the vector such that the x-axis now lies along N. The z-axis does not move. Now, the vector and the co-ordinate system are rotated about the N-axis by an angle β, which moves the z-axis to Z. Finally the vector is rotated about the Z axis
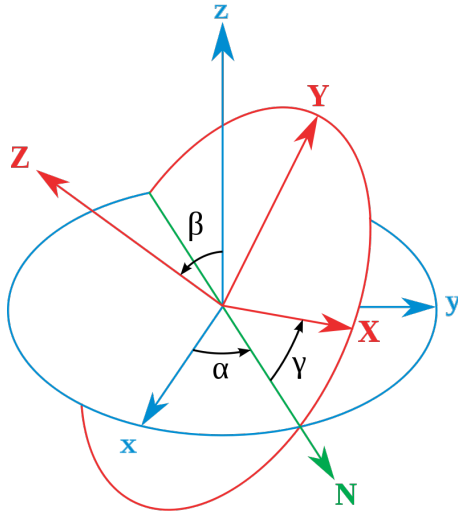
Figure 2.7: *The Euler angle definitions. This image was created by Lionel Brits and is reproduced with permission under the GNU Free Documentation License.*

by an angle γ. Every vector can now be described in terms of (α, β, γ), rather than using Cartesian co-ordinates. This has the benefit of defining the orientations with three components; a Cartesian system would require three components to define the direction and an additional component to define the rotation of the crystallite about the orientation axis.

Note that the ODF is typically not presented as a probability density function; probability density functions are normalised such that the sum of the probabilities of every orientation is 1.

Representing a four-dimensional object on a piece of paper is difficult to do in a useful way. A popular method is to drop one dimension by taking a cross-sectional slice through the ODF. For example one may take the cross-section described by the plane $z = 0$. By rotating the plane by several degrees at a time one may take cross-sections through the ODF at regular intervals creating an assay of cross-sections.
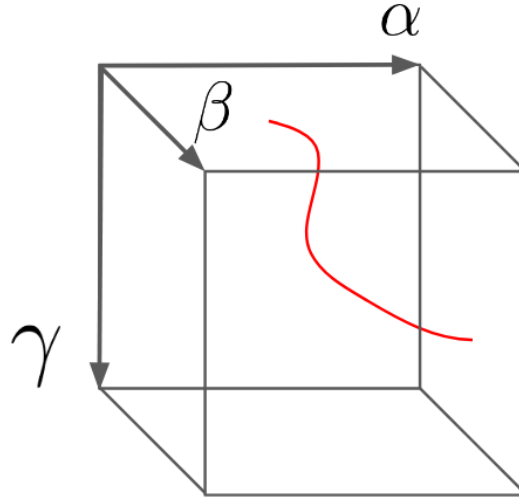
Figure 2.8: *A fibre (red) in Euler space. The axes shown are the Euler angles α, β, and γ. A fibre is any single curve that is drawn in this space.*

An alternative strategy is to stereographically project a single family of planes onto a flat surface, called a pole figure. This is similar to the way in which the globe is projected onto a flat map.

Some textures are characteristic of certain crystalline structures and material processes. One such example is the rolling process of BCC metals. Rolling involves the pressing of sheets of metal into thin foils with thickness of a few μm. When a BCC material is rolled in this way, a fibre texture is produced. A fibre texture is said to occur when the orientations populated in a sample map out a single curve in Euler space, as shown in figure 2.8. When a BCC material is subjected to the rolling technique described above, the material responds so as to form a fibre texture known as an α-fibre [50]. The form of the α-fibre will be explained more fully in section 4.6.7.

2.1.6 Crystal vibrations and the Debye temperature

Beyond the static structure of solids, there is dynamics. The temperature of a classical material with harmonic atomic potentials can be derived by starting with the energy relation

$$E = \frac{3}{2}k_B T = \frac{1}{2N}\sum_{n=1}^{N}m_n v_n^2 \tag{2.13}$$

where E is the average kinetic energy of atoms in the system, k_B is the Boltzmann constant, T is temperature, N is the number of atoms in the system, m_n is the mass of atom n and v_n is the velocity of atom n. The expression can be rearranged for temperature such that

$$T = \frac{1}{3Nk_B}\sum_{n=1}^{N}m_n v_n^2 \tag{2.14}$$

Thus, for a system containing atoms all of the same element, a temperature is defined by the average atomic speed $\bar{v} = \frac{1}{N}\sum_{n=1}^{N}|v_n|$. From classical theory, the atom speeds must obey a Maxwell-Boltzmann distribution. Only when this condition is satisfied can one use the temperature to make further inferences via equilibrium thermodynamic equations.

When a set of atoms on a crystal lattice exist at a non-zero temperature, they oscillate such that at any moment they may be instantaneously displaced from their central lattice positions. When considering a large population of atoms, the displacements from the lattice sites forms a distribution which is a function of temperature. This distribution can be calculated by considering models of vibrations in a solid.

The Einstein model of solids decouples the vibration of each individual atom, such that the instantaneous position of each atom has no effect on the surrounding atoms. In contrast, the Debye model of solids couples the atoms together. From the Debye model emerge phonons, the quasiparticle of lattice vibrations. This model yields the Debye temperature Θ_D which is defined as [38]

$$\Theta_D = \frac{hc_s}{2k_B} \sqrt[3]{\frac{6N}{\pi V}} \tag{2.15}$$

where h is the Planck constant, c_s is the sound speed of the solid, k_B is the Boltzmann constant, N is the number of atoms and V is the volume occupied by the atoms. The Debye temperature is the temperature at which the phonons of highest allowed frequency are excited; more than this, Θ_D indicates the temperature at which low-T quantum behaviour converges with high-T classical behaviour. Since Θ_D is proportional to c_s, it is also proportional to the stiffness of the inter-atomic potential.

The Debye model continues by giving the following expression for the heat capacity at constant volume C_V

$$\frac{C_V}{Nk_B} = 9\left(\frac{T}{\Theta_D}\right)^3 \int_0^{\Theta_D/T} \frac{x^4 e^x}{(e^x - 1)^2} dx \tag{2.16}$$

This equation shows the close entanglement of Θ_D and T; this relationship will be explored more fully in the work of section 3.8. In a compressed crystal Θ_D will change due to a "stiffening" of the interatomic potential. The Gruneisen parameter, Γ, can be used to describe the change in Θ_D as a function of V.

The Gruneisen parameter itself is a widely used thermodynamic quantity with

many interpretations. The Gruneisen parameter can be defined as

$$\Gamma = V \left(\frac{\partial P}{\partial E} \right)_V \tag{2.17}$$

where V is volume, P is pressure, and E is energy. In other words, the Gruneisen parameter details the pressure increase expected in a system when energy is added while maintaining a certain volume.

The characteristics of the system are important. Consider, for example, an ideal gas. Any extra energy input to the system would be used entirely as translational kinetic energy. The ideal gas equation of state is

$$PV = Nk_BT \tag{2.18}$$

and the total energy of the system is

$$E = \frac{3}{2}Nk_BT \tag{2.19}$$

where N is the number of gas particles and k_B is The Boltzmann constant. Combining these equations we get

$$PV = \frac{2}{3}E \tag{2.20}$$

thus the Gruneisen parameter is $\frac{2}{3}$. For a diatomic molecule

$$E = \frac{5}{2}Nk_BT \tag{2.21}$$

and so in this case $\Gamma = \frac{2}{5}$. This reduction in the increase of pressure with added

energy is simply explained by the fact that some of the energy has now been deposited in the vibrational motion of the molecules, thereby reducing the energy used for translational motion. It is evident, then, that one can work backwards to understand something of the vibrational properties of a material from its Gruneisen parameter.

Alternative but equivalent forms of the Gruneisen parameter are used in the field of shock compression. In the Mie-Gruneisen equation of state the Gruneisen parameter Γ is defined as

$$\Gamma(V) = -\frac{\partial ln\Theta_D}{\partial lnV} \qquad (2.22)$$

By rearranging this equation to the following form

$$\Theta_D = \Theta_0 exp\left(-\int_{V_0}^{V} \frac{\Gamma(V)}{V}dV\right) \qquad (2.23)$$

it can be used to give an estimate of Θ_D, given a value for Γ, and an initial uncompressed Debye temperature Θ_0.

2.2 Shock waves

In the ideal case, a shock wave is a travelling discontinuity in pressure. Figure 2.9 shows the formation of a shock front. A shock is formed when a pressure wave travels through a solid, causing compression of the material. The compressed material has an increased sound speed, causing subsequent pressure waves to propagate at a higher velocity. This next pressure wave catches up with the first, further compressing the material, and the cycle continues. The pressure profile steepens rapidly until there
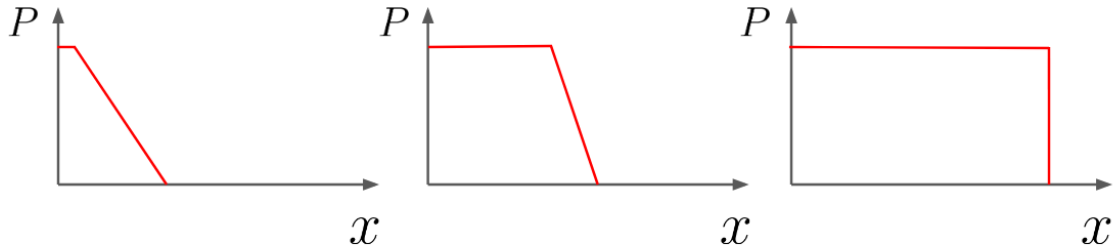
Figure 2.9: *An illustration of shock formation. A pressure wave is imparted into the solid. The increase in pressure leads to an increase in sound speed, resulting in subsequent pressure waves travelling faster than the initial pressure wave. Finally the latter pressure waves catch up to the initial disturbance, steepening the pressure front into a discontinuity in pressure a.k.a a shock wave.*

is a discontinuity in pressure, separating the material into shocked and unshocked regions. In the shocked region the pressure is very high, while in the unshocked region the pressure remains undisturbed from its initial value. Shock waves are transient, and so any solid exposed to a shock will necessarily decompress afterwards. For a short amount of time though, between shock arrival and material decompression, the sample will exist in a high pressure-temperature state, potentially long enough to reconstitute itself into an interesting, novel structure.

2.2.1 The Rankine-Hugoniot relations

The final state of a shocked material is given by the Rankine-Hugoniot relations, which themselves are derived from conservation of mass, momentum, and energy. The equations for an adiabatic shock are given below.

$$(u_s - u_p)\rho_1 = u_s\rho_0 \tag{2.24}$$

41

$$(P_1 - P_0) = u_s u_p \rho_0 \tag{2.25}$$

$$P_1 u_p = u_s \rho_0 \left(e_1 - e_0 + \frac{u_p^2}{2} \right) \tag{2.26}$$

Here u_s is the velocity of the shock wave, ρ_0, P_0, and e_0 are the density, pressure, and specific internal energy of the material before the shock wave has passed through the material, and ρ_1, P_1, and e_1 are the density, pressure, and internal energy of the material after the shock wave has passed through. u_p is the particle velocity; the particle velocity accounts for the translation of the bulk material upon being struck. This can also be thought of as a piston velocity, where a hypothetical piston pushes the material, generating a shock in the sample. Four of the quantities in the above equations are generally unknown: P_1, ρ_1, u_s, and u_p. Note that e_1 is not considered an unknown variable here. This is because e_1 can be expressed in terms of the other variables; in this adiabatic system, the increase in internal energy is produced entirely by the work done by the piston W_p. The work done is the force, $P_1 A$, multiplied by the distance travelled, $u_p \delta t$, where A is the cross-sectional area of the sample and δt is the time elapsed. Therefore $e_1 = e_0 + W_p = e_0 + P_1 A u_p \delta t$.

A material equation of state is required to close the Rankine-Hugoniot equations. By manipulating the equations and using the ideal gas approximation, the Hugoniot equation for an ideal gas is generated.

$$\frac{\rho_1}{\rho_0} = \frac{(\gamma + 1)\frac{P_1}{P_0} + (\gamma - 1)}{(\gamma + 1) + (\gamma - 1)\frac{P_1}{P_0}} \tag{2.27}$$

Here γ is the ratio of the heat capacity at constant pressure C_P to the heat capacity at

constant volume C_V. The Hugoniot equation defines the locus of all states resulting from any strength shock, given a unique starting state. Many experiments are often constrained to the states described by this equation, eliminating the need to measure all of the material properties. Until recently, the temperature of a shocked state has been inferred from these equations rather than measured; such an inference requires a heat capacity to be assumed, which is not necessarily well known in the shock regime.

In order to reach even higher pressure states, a sequence of shocks may be imparted to a target in a procedure known as multi-shock compression. In such experiments, the final state can be predicted by applying the Hugoniot relations repeatedly such that the initial state of the next shock wave is the final state of the previous shock. There are also efforts to produce off-Hugoniot states, especially lower temperature states; these states are closer to the isentrope and so more closely resemble planetary core conditions. These off-Hugoniot states can be achieved via ramp compression, where the energy deposition rate is too low to seed a mature shock wave. In such experiments the final state is no longer constrained to the Hugoniot as described above and so knowledge of temperature is no longer produced from the Hugoniot equations. In such a situation it is necessary to measure temperature so as to close the equation of state.

2.2.2 Laser-generated shock waves in crystalline materials

High power lasers are routinely employed to generate shocks in crystalline solids. A large amount of energy, often thousands of joules, is deposited into the material of interest in the space of a few nanoseconds. This energy deposition results in

the rapid ablation of material from the surface of the sample. Due to conservation of momentum, a shock wave is driven into the sample. The shock wave generates enormous pressures in the sample; a stress is said to be applied to the material.

Each material has a unique capacity to withstand stress. When a sufficiently high stress is applied to a crystal, the atoms will rearrange in some way; this is known as plastic deformation. If a relatively small stress is applied the crystal will maintain its structure while being compressed. This is called elastic deformation. The stress at which the deformation changes from elastic to plastic is called the elastic limit. The strength of a material is the ability of the material to withstand stresses without plastic deformation; a high strength material will thus have a high elastic limit.

2.3   X-ray diffraction

X-ray diffraction is a diagnostic technique that has been used for over a hundred years. It exploits the wave character of x-rays to probe the atomic structure of materials. It has enjoyed great success and has been employed in the discovery of many structures including the double-helix structure of DNA [51]. Nowadays it is routinely used to characterise the structure of proteins [52], pharmaceuticals [53], and alloy properties [54]. It is also employed on laser shock experiments to interrogate the transient structures present on nanosecond timescales [55, 56, 57, 58, 59].

2.3.1   Elementary theory of x-ray diffraction

When an x-ray interacts with an electron, the electron will oscillate exactly out of phase with the electric field of the x-ray. This oscillating charge then re-emits in

every direction. If the initial x-ray beam is unpolarised, with electric fields oriented uniformly about the x-ray beam, the electron will emit an electric field with intensity

$$I_e = I_0 \frac{e^4}{m_e^2 c^4 R^2} \left(\frac{1 + cos^2(2\theta)}{2} \right) \tag{2.28}$$

where I_0 is the intensity of the incident beam, e is the charge on an electron, c is the speed of light in a vacuum, R is the distance between the electron and the point of observation, and θ is half the angle between the incident beam and the scattered beam [48]. Recall that intensity is power per unit area; when detecting x-rays it is intensity that is measured, thus intensity is made the subject of all relevant equations.

Scattering from an atom is slightly more complicated. The electron cloud around an atom will not simply scatter as if from multiple isolated electrons. Instead each element has a unique x-ray diffraction fingerprint in the form of the atomic scattering factor f. The intensity of scattering from a single atom is

$$I_a = f^2 I_e \tag{2.29}$$

Now consider a crystal, where regularly spaced atoms are all scattering x-rays at the same time. Since x-rays have wave character, the scattered x-rays will interfere with each other. If a detector is placed some distance away from the crystal, it will detect bright spots of intensity where the x-rays constructively interfere, and large dim regions where this does not occur. The exact location of the bright spots is determined by the structure of the crystal. This is called the Laue picture.

The Bragg formulation is an alternative way of conceptualising diffraction, and
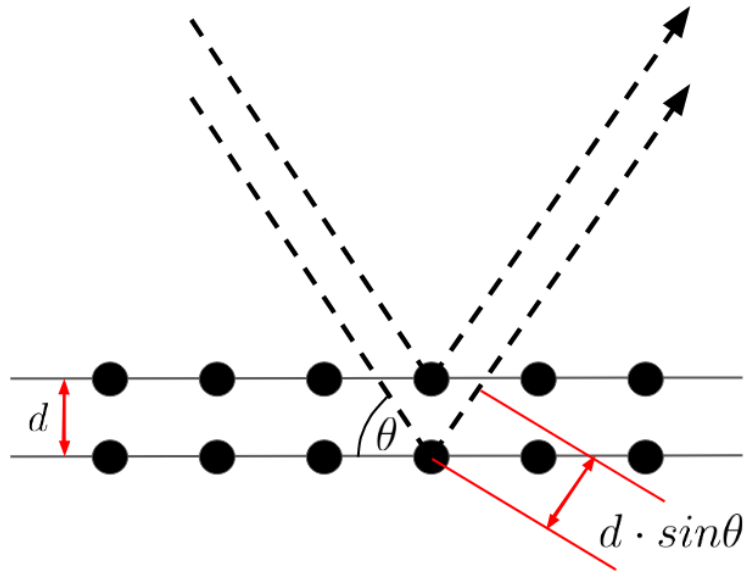
Figure 2.10: *The Bragg picture of diffraction.*

is depicted in figure 2.10. Instead of considering x-rays to be scattered by individual atoms, x-rays are specularly reflected by entire sets of atomic planes. At certain angles the reflected radiation from subsequent planes will be exactly in phase. The angle θ_B is the angle between the incident/reflected x-ray beam and the reflection plane, and is referred to as the Bragg angle. If a crystal undergoes diffraction, the Bragg condition is said to have been met. The Bragg condition is met when

$$\lambda = 2d_{hkl}sin\theta_B \tag{2.30}$$

where λ is the wavelength of the incident x-rays, and d_{hkl} is the interplanar spacing for the plane hkl.

For some structures there are planes for which a reflection is not "allowed", and so not every plane produces a viable reflection; this is due to destructive interference

specific to the structure. These missing reflections are dealt with more completely in the Laue picture, through the use of the structure factor F

$$F = \sum_{j=1}^{N} f_j e^{-2\pi i(h\mathbf{a_1}\prime + k\mathbf{a_2}\prime + l\mathbf{a_3}\prime)} \tag{2.31}$$

where f is the scattering factor of the jth atom, N is the number of scattering atoms, h k l are the Miller indices of the current reflection, and $\mathbf{a_1}\prime$ $\mathbf{a_2}\prime$ $\mathbf{a_3}\prime$ are the normalised lattice vectors of the crystal. Qualitatively, the structure factor and the reciprocal lattice are the same. Recall that the reciprocal lattice represents the planes present in a crystal. The reciprocal lattice already accounts for the disallowed reflections and so it is a useful construct when predicting the direction of diffraction from a crystal, as will now be shown.

The wavevector of an x-ray beam is given by

$$\mathbf{k} = \frac{2\pi}{\lambda} \tag{2.32}$$

If the tip of the incident beam wavevector $\mathbf{k}_0$ is placed on the origin of the reciprocal lattice as shown in figure 2.11, the reflected wavevector $\mathbf{k}_r$ may be placed at the same starting point as $\mathbf{k}_0$. By scanning $\mathbf{k}_r$ through every possible position it is found that $\mathbf{k}_r$ intersects the reciprocal lattice at specific orientations. These orientations represent the satisfaction of the Bragg condition and so indicate an orientation at which diffraction will be observed. The angle between $\mathbf{k}_0$ and $\mathbf{k}_r$ will be $2\theta_B$. The scattering vector is given by

$$\mathbf{G} = \mathbf{k}_r - \mathbf{k}_0 = \Delta\mathbf{k} \tag{2.33}$$
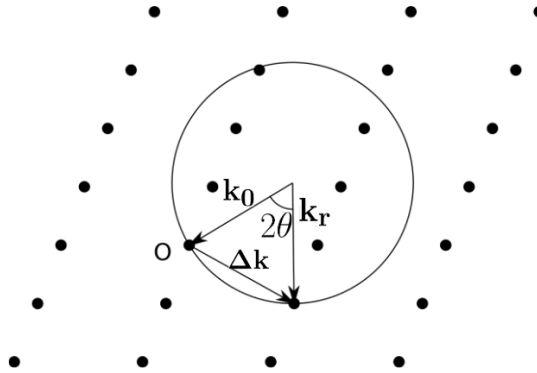
47

Figure 2.11: *The Ewald construction, showing the intersection of the Ewald "sphere" with the reciprocal lattice. This image is an altered version of the image created by the Wikipedian Wiso and is reproduced here with permission under the Creative Commons license.*

and diffraction occurs when

$$\mathbf{G} = h\mathbf{b}_1 + k\mathbf{b}_2 + l\mathbf{b}_3 \tag{2.34}$$

Diffraction from a single crystal will produce single beams of reflected x-rays. When these beams are intercepted by a detector they show up as bright spots. In contrast, diffraction from a polycrystal produces cones of diffraction. This is because the Bragg condition can be met by rotating a grain about the axis of the incident x-ray beam; in a polycrystal, it is possible for many grains to meet the Bragg condition in this way, resulting in a cone of diffraction. When a planar detector intercepts these cones, conic sections are observed, often termed "diffraction rings". If the polycrystal is an ideal powder, consisting of a perfectly uniform distribution of grains, the rings will be smooth and will have no variation in intensity arising from preferential crystallographic orientation. Note that there will still be variations

48

in intensity around the ring due to other geometrical effects to be discussed in section 2.3.3. Diffraction from a polycrystalline solid is often referred to as "powder diffraction", even when there is no powder but instead a single block of material containing many crystallites.

The multiplicity of crystal planes plays an important role in x-ray diffraction. In a typical powder x-ray diffraction experiment a family of planes will all reflect to the same positions on an x-ray detector, but each individual plane will contribute an equal amount to the overall intensity of the signal. The result is that some rings will be much brighter than others due to the larger number of planes contributing to the reflection.

In laser-shock experiments, the crystal structure is compressed. This results in a shortening of the lattice constant, and therefore an increase in the Bragg angle. By measuring the change in Bragg angle one also measures the compression of the sample. If the x-rays from the compressed material are not reflected in a perfect cone, one can conclude that the material is experiencing a non-uniform compression. This is evidence that the material is resisting plastic deformation; i.e. it is evidence of strength in the material. This fact has been exploited to make measurements of material strength under extreme loads [60] [61].

2.3.2 The effect of temperature on x-ray diffraction profiles

A crystal with some temperature T will consist of vibrating atoms. At any one instant the atoms will be displaced from their equilibrium lattice sites. When diffraction takes place the atoms are scattered from in their displaced positions. These small displacements cause a loss of coherence in the diffraction pattern, and

the result is a loss in diffraction peak intensity. This is called the Debye-Waller effect. If the phonons obey a Bose-Einstein distribution, the intensity of diffraction will be altered in the following way [48]:

$$I(T) = I_0 exp(-2M) \tag{2.35}$$

$$2M = \frac{12h^2 N_a sin^2(\theta)}{m\lambda^2 k_B \Theta_D} \left[\frac{T^2}{\Theta_D^2} \int_0^{\Theta_D/T} \frac{x}{e^x - 1} dx + \frac{1}{4} \right] \tag{2.36}$$

where I_0 is the intensity of diffraction at 0 K, N_a is Avogadro's number, and m is the molar mass of the material being probed. By substituting for $|\mathbf{G}| = 4\pi sin\theta/\lambda$, the following equation is formulated

$$2M = \frac{3h^2 N_a |\mathbf{G}|^2}{m k_B \Theta_D} \left[\frac{T^2}{\Theta_D^2} \int_0^{\Theta_D/T} \frac{x}{e^x - 1} dx + \frac{1}{4} \right] \tag{2.37}$$

where $\mathbf{G}$ is the reciprocal lattice vector associated with the reflection currently being considered. If the atoms instead follow a Boltzmann distribution, as in the case of a classical solid, the equation instead becomes

$$2M = \frac{3h^2 N_a |\mathbf{G}|^2}{m k_B \Theta_D} \left[\frac{T}{\Theta_D} \right] \tag{2.38}$$

A comparison of the classical model (equation 2.38) and the quantum model (2.37) is presented in figure 2.12. Since the equations share the same pre-factors, the functional form of the classical equation is given by c, and the functional form of the quantum equation is given by q, where

$$c = \frac{T}{\Theta_D} \tag{2.39}$$

$$q = \frac{T^2}{\Theta_D^2} \int_0^{\Theta_D/T} \frac{x}{e^x - 1} dx + \frac{1}{4} \tag{2.40}$$

For T above Θ_D, the ratio of the two models converges to 1. This reflects the fact that, at high temperatures, the occupation of states in a Bose-Einstein solid resembles the occupation of states in a Boltzmann solid. The two models only meaningfully disagree at temperatures below the Θ_D. It is therefore suitable to apply the simpler classical model to a quantum system at temperatures far above Θ_D. At temperatures near to or far below Θ_D, the more cumbersome quantum model should be used.
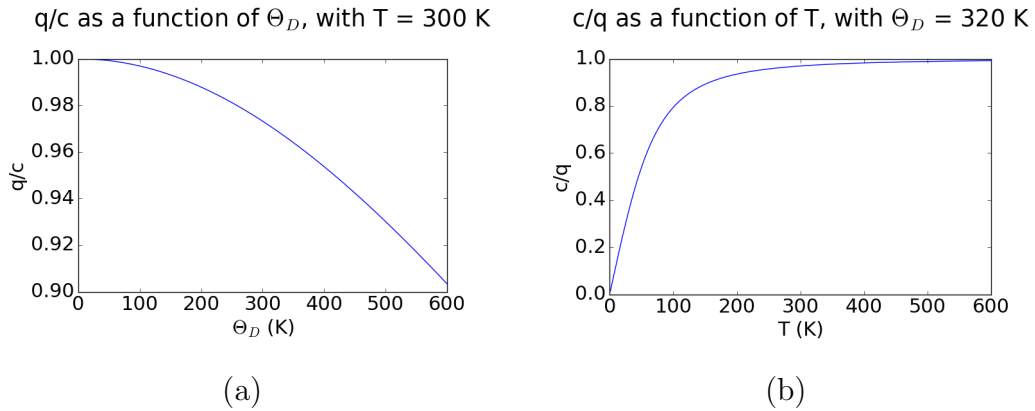

(a) (b)

Figure 2.12: *(a) The ratio of the quantum model for Debye-Waller factor to the classical model as a function of Θ_D. The temperature is kept at 300 K. (b) The ratio of the classical model for Debye-Waller factor to the quantum model as a function of T. The Debye temperature Θ_D is kept at 320 K.*

The vibrational properties of a solid are important in determining the mean

square distance of atoms from their equilibrium positions, hence the appearance of Θ_D here in the Debye-Waller equation. If a material has a high Θ_D, the atoms will be tightly bound and will have a relatively small amplitude of oscillation. The result will be a modest decrease in diffraction intensity due to temperature. Conversely, a low Debye temperature allows atoms to move further from the equilibrium lattice positions, and therefore the Debye-Waller effect will be more noticeable.

2.3.3 The Lorentz-polarisation intensity correction

When a beam of x-rays scatter from an atom, the light will become polarised as shown in figure 2.13. The electric field E from the incident x-ray beam originating at P_0 causes the electrons of atom A_0 to oscillate in the plane of the incident beam. If the atom is viewed from P_1, a direction perpendicular to the oscillating plane, all of the electron electric field oscillations are "visible". Since the detected intensity $I \propto E^2$, the detected intensity at P_1 receives contributions from every component of the electric field. If the oscillating electrons are observed from a direction within the plane of oscillation, such as P_3, only electric field components out of the line $|A_0P_3|$ contribute to the intensity, and so the intensity is reduced. In the case of an intermediate observation point such as P_2, the intensity will be reduced when compared to P_1, but will not be reduced as much as in P_3.

The effect is a reduction in the intensity of the form

$$I_D = I_0 \frac{1 + cos^2 2\theta_B}{2} \tag{2.41}$$

where I_0 is the corrected intensity, and I_D is the detected intensity [48]. Note that
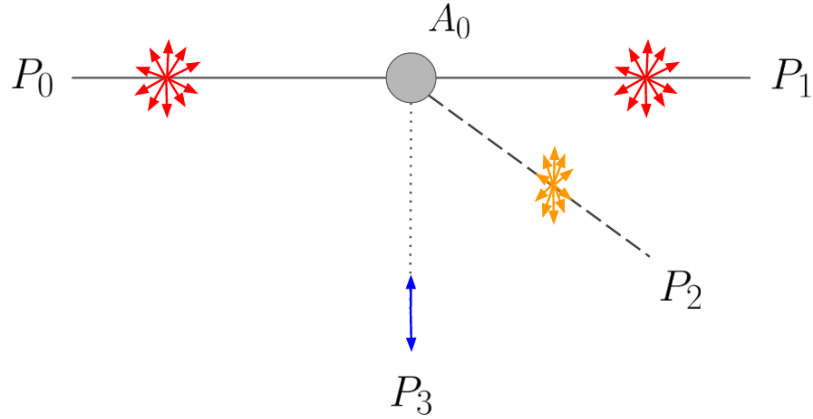
Figure 2.13: *Polarisation due to scattering from an atom. The incident beam approaches the atom from the left.*

the polarisation factor is already apparent in equation 2.28.

The Lorentz factor originates from a number of geometrical considerations which will now be discussed [62]. The first part of the correction arises from the fact that the reciprocal lattice for a real crystal is not a set of discrete delta functions. Instead, the reciprocal lattice has a finite width. Similarly, the probing x-ray beam is not perfectly monochromatic. Thus the intersection between the Ewald sphere and the reciprocal lattice will enclose a volume rather than intersect at a point. When the intersection angles are near-perpendicular, the enclosed volume will be smaller than when the intersection angles are near-parallel. These geometric features give rise to the first portion of the Lorentz factor.

$$L_1 \propto \frac{cos\theta_B}{sin2\theta_B} \tag{2.42}$$

Another fragment of the Lorentz factor arises from instrumental considerations,

where a detector of constant width is used to detect reflections. This correction applies when an intensity per unit length is measured; the correction does not apply to measurements of intensity per ϕ. The fraction of the intercepted diffraction cone varies with θ_B according to the following relationship.

$$L_2 = \frac{1}{sin2\theta_B} \tag{2.43}$$

The two Lorentz corrections are often given together with the polarisation correction in the form of the Lorentz-polarisation correction. Since relative diffraction intensities are often the goal, a proportional relationship showing the dependence of intensity on angle is sufficient.

$$LP \propto \frac{cos(\theta_B)(1 + cos^2(2\theta_B))}{sin(2\theta_B)} \tag{2.44}$$

2.3.4 Dislocations and x-ray diffraction

The effect of dislocations on x-ray diffraction profiles is described by the theory of Wilkens [63, 64, 65, 66]. To characterise the dislocations a cylinder is considered of area F_0 containing N_0 dislocations running parallel to the cylinder axis. The cylinder area is divided equally into p^2 sub-areas such that each area now contains $N_p = \frac{N_0}{p^2}$ dislocations. The dislocation density is given by

$$\rho = \frac{N_0}{F_0} = N_p F_p \tag{2.45}$$

and the radius of each of the sub-areas is

$$R_p = \sqrt{\frac{F_p}{\pi}} = \frac{1}{p}\sqrt{\frac{F_0}{\pi}}. \tag{2.46}$$

In this model, the dislocations are allowed to be randomly distributed within these sub-areas, but they are not allowed to interact with dislocations in other sub-areas. This setup is called "a restrictedly random distribution" of dislocations.

The angle ψ is the angle between the line vector $\mathbf{l}$ and the plane $\mathbf{G}$ from which the reflection is taking place. This angle determines the degree to which the lattice distortion from the dislocations affects the profile. This phenomenon enters the analysis in the form of the contrast factor. The contrast factor for a screw dislocation C_s is given by

$$C_s = sin^2(\psi)cos^2(\psi) \tag{2.47}$$

The intensity profile for a screw dislocation is given by

$$I(s) = 2\int_0^\infty exp\left[-\frac{\pi}{2}\mathbf{g}^2\mathbf{b}^2 C_s \rho n^2 f(\eta)\right]cos(2\pi nS)dn \tag{2.48}$$

where $\mathbf{b}$ is the burgers vector of the dislocation, n integrated variable, and $S = \frac{2}{\lambda}sin(\theta_B)$, with λ being the wavelength of the incident x-rays. The function $f(\eta)$ is typically called the Wilkens function [67], where

$$\eta = \frac{nsin(\psi)}{2R_p} \tag{2.49}$$

and $f(\eta)$, when $\eta < 1$, takes the form:

$$f(\eta) = -log(\eta) + (\frac{7}{4} - log(2))$$
$$+\frac{512}{90\pi\eta} + \frac{2}{\pi}\left[1 - \frac{1}{4\eta^2}\right]\int_0^\eta \frac{arcsin(V)}{V}dV$$
$$-\frac{1}{\pi}\left[\frac{769}{180\eta} + \frac{41\eta}{90} + \frac{2}{90}\eta^3\right]\sqrt{1-\eta^2}$$
$$-\frac{1}{\pi}\left[\frac{11}{12\eta^2} + \frac{7}{2} + \frac{\eta^2}{3}\right]arcsin(\eta) + \frac{\eta^2}{6}$$

(2.50)

and when $\eta > 1$:

$$f(\eta) = \frac{512}{90\pi\eta} - \left[\frac{11}{24} + \frac{log(2\eta)}{4}\right]\frac{1}{\eta^2} \qquad (2.51)$$

If one wishes to consider edge dislocations a different value for contrast factor C_e is used:

$$C_e = sin^4(\psi)\frac{1}{8(1-\nu^2)}[(1 - 4\nu + 8\nu^2) + 4(1 - 2\nu)cos^2(\Phi)] \qquad (2.52)$$

where ν is the Poisson ratio, and the angle Φ is defined by $\mathbf{g}\times\mathbf{l}\cdot\mathbf{b} = |\mathbf{g}||\mathbf{l}||\mathbf{b}|sin(\psi)sin(\Phi)$. Finally, if the desired dislocation has mixed character, an interaction term C_i is necessary:

$$C_i = sin^3(\psi)cos(\psi)cos(\Phi)\frac{3 - 7\nu + 4\nu^2}{2(1-\nu)^2} \qquad (2.53)$$

The three terms can be mixed so as to be applicable to any mixed-character dislocation:

$$C_\gamma = cos^2(\gamma C_s) + sin^2(\gamma C_e) + sin(\gamma)cos(\gamma)C_i \qquad (2.54)$$

where γ is the angle between $\mathbf{l}$ and $\mathbf{b}$. Equation 2.48 can be used for any type of dislocation by replacing C_s with an appropriate contrast factor given by equation 2.54.

2.4 Molecular dynamics simulations

While direct experimentation forms the bedrock of all scientific knowledge, computer simulations have arisen as important tools in the support of research. Simulations are often cheap and convenient counterparts to experiment.

In addition, simulations offer insight inaccessible to the experimentalist. In the case of molecular dynamics, a system of atoms is simulated undergoing a wide range of possible processes. Since every atom is accounted for in these simulations, an extreme level of detail is available for investigation.

Classical molecular dynamics simulations often involve the numerical evaluation of Newton's equations of motion for a many body system. These equations take the form

$$M\frac{\delta^2 \mathbf{x(t)}}{\delta t^2} = -\nabla V(\mathbf{x(t)}) \tag{2.55}$$

Here M is a matrix containing the masses of all atoms in the system, $\mathbf{x(t)}$ contains all the positions of atoms, and V is the potential that describes the system. In order to dynamically simulate the system, a numerical integrator such as the Verlet algorithm is implemented in order to iterate the system over a discrete number of timesteps [68]. A velocity Verlet is used to update velocities as a result of the surrounding atomic potentials. The following equation is then evaluated

$$\mathbf{x_1} = \mathbf{x_0} + \mathbf{v_0}\mathbf{\Delta t} + \frac{1}{2}\mathbf{a_0}\mathbf{\Delta t^2} \qquad (2.56)$$

where $\mathbf{x_o}$, $\mathbf{v_0}$, and $\mathbf{a_0}$ are the initial position, velocity, and acceleration of an atom, $\mathbf{x_1}$ is the new position, and Δt is the length of the time step. The acceleration $\mathbf{a_0}$ is calculated from the potential $V(\mathbf{x(t)})$. The forces are then updated according to the new atom positions.

The method of simulating material systems computationally has many unique advantages over traditional experimentation including microstructural knowledge and access to material parameters otherwise difficult to extract, such as temperature. The root of these advantages lies in the complete knowledge of atoms and their positions, allowing a bottom-up approach to measuring quantities in the system. It is important, however, to ensure any results from MD match what we observe in reality. Fundamentally, classical molecular dynamics misrepresents reality as we know it; no quantum effects are modelled in a classical MD simulation, and so material properties such as discretised phonon dispersions are overlooked. While it is interesting to use MD to probe regimes that are not currently accessible [69] the results without experimental verification are, at best, an indication of potentially interesting physics.

2.4.1 Simulated solids

The MD software used in this project is the Large-scale Atomic/Molecular Massively Parallel Simulator (LAMMPS), a popular software package that has been used widely to simulate shock-waves [70, 71]. LAMMPS creates a list of nearest neighbours for

each atom by using a cut-off radius around the atom in order to save computational time. Atoms that are outside this radius are deemed to have a negligible effect on the atom for which the neighbour list is constructed. The neighbour lists will be updated for each time step, as atoms will move in and out of the cut-off radius over the course of the simulation.

A simulation box is defined and the properties of the boundaries that hold the atoms in the simulation can be changed. A periodic boundary conditions allows atoms on opposite sides of the simulation box to interact with each other through the faces of the box, as if the atoms were next to each other. The purpose of this is to better approximate the behaviour of bulk material and eliminate edge effects. The situation is a little more complicated for a planar shock, since periodic boundary conditions are only desirable in two dimensions. In the case of a shock simulations, it is typical to simulate a piece of material in the shape of an elongated cuboid [72]. The extra length is given to the direction of travel of the shock wave with periodic boundary conditions enforced in the perpendicular directions.

2.4.2 The role of atomic potentials

Of utmost importance to MD is the careful selection of a potential, since it is the potential that determines the physics of simulated interactions. When MD was first used to study shocks, simple models such as the Lennard-Jones potential were used [73]. As research has progressed and emphasis placed on accurate large-scale modelling, more sophisticated potentials have been developed. There are numerous methods used to develop a potential, such as the embedded atom method (EAM). EAM potentials are derived from a combination of density-functional theory and

semi-empirical methods. This thesis is concerned with simulating metals, and EAM potentials have been shown to reasonably simulate metallic behaviour [74].

2.4.3 Thermostats

Suppose a lattice has already been defined and atoms placed at all of the designated atom locations, such that the atoms now all sit exactly on their lattice sites. To impose a temperature on the system, the atoms must be given a certain amount of energy at the beginning of the simulation.

Energy is distributed by assigning each atom a velocity. The velocities themselves are created in the manner of a user-defined distribution; in the case of this project a Gaussian velocity distribution has been used. Each velocity in the distribution is then assigned to a random atom. When the simulation begins to iterate, the atoms will move away from their lattice sites and some of the kinetic energy that was originally imparted to the atoms is converted to potential energy, resulting in a net loss of kinetic energy of the atoms in the system. As further iterations are computed, approximately half of the energy will be tied up in potential energy (via the equipartition theorem), and so the kinetic energy will also be halved, resulting in a halving of temperature.

To counteract this drop in temperature, a thermostat may be applied to the simulation. The thermostat will periodically review the kinetic energy of the system and determine if there is a change in temperature. If the system temperature has deviated from the desired temperature, kinetic energy will be added or removed so as to correct for the discrepancy.

Perhaps the most obvious way of doing this is to rescale the velocities of the

atoms according to the discrepancy between the current state and the desired state. This method is often avoided since it is a non-physical way of adding energy. Instead, a Nosé-Hoover thermostat can be implemented [75]. This works by introducing a new degree of freedom to the system which acts as a heat bath. Two commonly used thermostats are referred to as nvt and npt. An nvt thermostat keeps the number of particles (n), the volume (v), and the temperature (t) approximately constant. Similarly, an npt thermostat keeps the number of particles (n), the pressure (p), and the temperature (t) approximately constant

A specialised thermostat called the Hugoniostat is a popular tool for investigating shocked materials [76]. The Hugoniostat requires an input pressure from the user. The Hugoniostat then reshapes the simulation box to achieve the desired pressure conditions. The Rankine-Hugoniot equations from section 2.2.1 are solved to give the expected temperature along the Hugoniot; using this temperature, a thermostat is applied to the simulation box. The Hugoniostat is therefore a convenient tool for creating shocked simulated solids.

2.4.4 Simulating x-ray diffraction from molecular dynamics

The output of LAMMPS is a list of atom positions. With these atom positions we can simulate an x-ray diffraction pattern by performing a Fourier transform (FT) of the atom positions [72]. The discrete Fourier transform is

$$I(\mathbf{q}) \propto |F(\mathbf{q})|^2 \propto Z^2 |\sum_{j=1}^{N} exp(i\mathbf{q} \cdot \mathbf{r}_j)|^2 \tag{2.57}$$

where I is the intensity at the reciprocal space point $\mathbf{q}$, F is the structure factor

of the crystal, and $\mathbf{r}_j$ is the real space position of atom j. By summing over the positions of every atom, a single reciprocal space intensity can be generated. By calculating the reciprocal space intensities in the vicinity of a reciprocal lattice site, the x-ray diffraction profile of the crystal can be simulated. This procedure is used in the following chapter to generate x-ray diffraction profiles of a variety of atomic systems.

Chapter 3

Molecular Dynamics Simulations of Temperature Measurement using the Debye-Waller Effect

In this chapter, molecular dynamics (MD) simulations are used to investigate the feasibility of using the Debye-Waller effect to measure temperature in solids under shock compression. These investigations were first attempted by Murphy et al [37]. Murphy et al simulated a 60x60x60 box of FCC Cu under static conditions and were able to accurately measure the Debye-Waller factor. The work of Murphy et al also investigated the Debye-Waller response to compression due to a shock. The Cu was compressed along [1 0 0]; compression of an FCC lattice along this direction results in a phase transformation to BCC. The derived Debye-Waller factors were used to predict Debye temperatures of Cu under compression and compared to Debye temperatures predicted by a variety of Gruneisen parameter models. It was shown

that the phase transformation led to a departure in predicted Debye temperature, relative to a selection of Gruneisen parameter models.

While the work of Murphy et al was an important first step in the study of the Debye-Waller effect in shock compressed MD, the work stopped short of assessing the impact of different Gruneisen parameter models on the accuracy of a potential temperature measurement. What's more, the observed phase transformation added unnecessary complexity to the analysis of Debye temperature undergoing uniaxial compression. The impact of crystal imperfections were also left largely unconsidered.

This chapter sets out to establish more concretely the feasibility of using the Debye-Waller effect as a temperature measurement tool on laser-shock experiments, and to reveal the potential challenges an experimentalist might face. A number of confounding situations are investigated in such a way that their effect is isolated and measured, allowing a hierarchy of impact to be constructed.

3.1 Thermalisation times for a set of atoms

The MD software used in this chapter is LAMMPS [77]. This software has been used to produce a vast amount of high-quality work performed by a huge community of users, and so LAMMPS is considered to be a high-quality, robust code. However, when using computational techniques such as MD it is important to understand the limitations of the software, and its relevance to the problem at hand, so as to give valuable context when interpreting any results. This is especially important when using third party software such as LAMMPS, which can often be used as a black-box. It is therefore prudent to independently examine LAMMPS and ensure

sensible atomic systems are being produced.

It is practical to establish the minimum time necessary for a box of atoms to thermalise. This knowledge is useful when setting up further simulations, ensuring that simulations are evolved over an appropriate timescale. If the simulation finishes too soon, the derived results may be misleading since the system is not in equilibrium. Conversely, too long a timescale is wasteful, especially when considering larger simulations.

A classical atomic system is said to be in thermal equilibrium when there is no net flow of matter and the atom speeds obey a Maxwell-Boltzmann distribution. Since the simulations considered here do not exchange matter with any other system, the latter part of this definition is the relevant qualification for thermodynamic equilibrium. The Maxwell-Boltzmann probability density function is given by the equation

$$PDF(x) = \sqrt{\frac{2}{\pi}} \frac{x^2 e^{-x^2/(2a^2)}}{a^3} \tag{3.1}$$

where x is the independent variable and a is the fitting parameter.

A LAMMPS simulation box of FCC Cu was setup using the Cu Mishin EAM1 potential developed by Mishin et al [78]. This potential was used by Murphy et. al. and so is used here for the sake of comparison. This potential has been shown to produce shock characteristics commensurate with experiment [70]. The box has periodic boundaries i.e. atoms on the edge of the box will interact with atoms on the opposite side of the box to remove anomalous behaviours associated with sample edges. The atoms were first assigned a velocity distribution consistent with 300 K; this is achieved by assigning Gaussian distributions to the velocities in x y z. As

the atoms are allowed to evolve, one observes that the temperature of this system rapidly drops to 150 K. This is because, initially, all of the energy in the system is kinetic, with no energy taking the form of potential. The result is that over time the energy will become evenly distributed between kinetic and potential, and so the velocity distribution of the atoms will now correspond to a system at 150 K. In order to restore the system to the desired temperature of 300 K, the system is coupled to a Nosé-Hoover thermostat.

Different box sizes were selected to investigate the effect of an increase of atoms on the thermalisation time. A cube of lattice points were set up with side length N of 5, 20, 60, and 100, where N is the number of conventional lattice sites along each cube dimension. For an FCC material like Cu, the number of atoms per conventional unit cell is 4, thus the number of atoms in each simulation is $4N^3$. The simulation is allowed to run for 10000 timesteps, with each timestep corresponding to 1 fs.

N = 5	N = 20	N = 60	N = 100
10.81 K	1.55 K	0.64 K	0.52 K

Table 3.1: *The standard deviation in temperature, in the last 5000 timesteps, for boxes with side length N = 5, 20, 60, 100.*

The temperature of each simulation every 100 timesteps is shown in figure 3.1. The thermalisation time increases as N increases. The scatter about the desired temperature also improves with increasing N; this is to be expected given the more favourable statistics associated with larger systems. The standard deviations in temperature for each box size are shown in table 3.1; these figures are calculated from the final 5000 timesteps of the simulation.

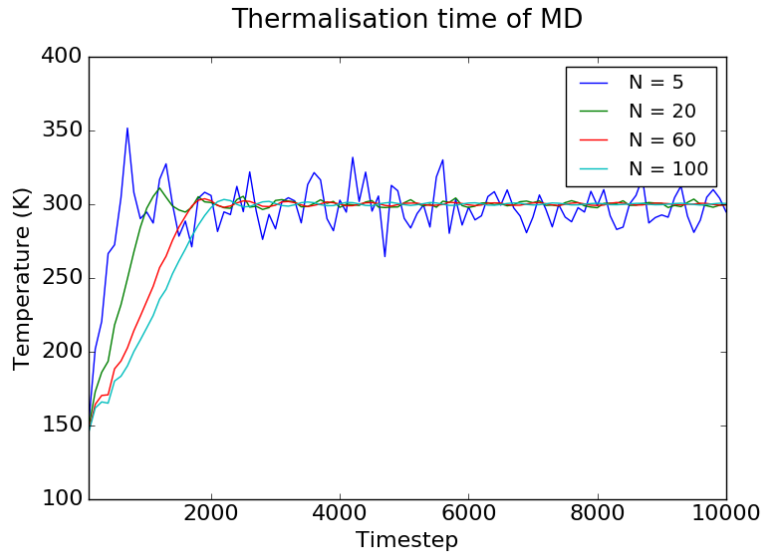Figure 3.2 shows the atomic speed distributions of simulations with $N = 20$ and

Figure 3.1: *The temperature over time of simulated copper is shown for different box sizes.*

$N = 100$ at timestep 10^4. A normalised form of equation 3.1 is applied in each case. Again, the increased number of atoms in the $N = 100$ simulation reduces scatter about the fit.

Based on the results shown in figures 3.1 and 3.2, thermal equilibrium is sufficiently achieved by timestep 10000 on large simulation boxes. When performing simulations starting from an equilibrated material, these conditions should first be met.

3.2 The lattice parameter of simulated copper and niobium

Cu has a lattice parameter of 3.615 Å at s.t.p. [79]. The Cu potential used in simulation may differ from these values and so an appropriate lattice parameter

(a) $N = 20$

(b) $N = 100$
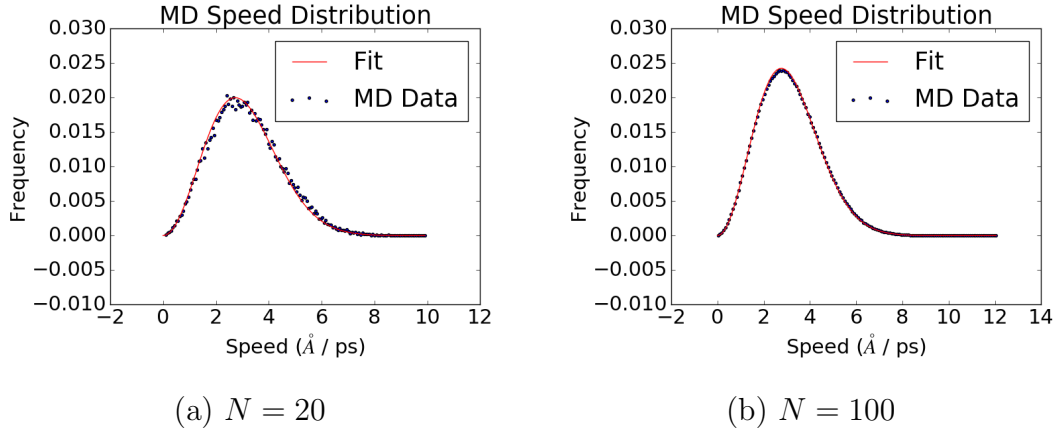
Figure 3.2: *Speed distributions of simulated Cu at 300 K. A Maxwell-Boltzmann distribution function is fit to the data.*

should be found.

A 100x100x100 cube of Cu was simulated using the Cu Mishin EAM1 potential, with an initial lattice parameter of 3.615 Å. The Cu was first thermalised to 300 K for 5000 timesteps of 1 fs, using an nvt Nosé-Hoover thermostat. Once the material was thermalised, the thermostat was changed from an nvt to an npt; the volume is now allowed to change, and so the material should relax to a pressure of 0 bar. This npt was performed for a further 5000 timesteps of 1 fs. Figure 3.3 shows the lattice parameter a and the corresponding material pressure P every 100 timesteps during the npt phase of the simulation. The conventional lattice parameter was calculated from the volume V by the equation $a = \sqrt[3]{V}/N$, where $N = 100$ in this instance. The line fit has the equation $a = $-8.77009516x$10^{-07}P + 3.63185453$. The standard deviation of points about the trend line is 3.183x10^{-05}. Therefore at $P = 0$ bar and $T = 300$ K , the equilibrium lattice parameter of Cu Mishin EAM1 is reported as 3.63186 $\pm$ 3 $\times 10^{-5}$ Å.
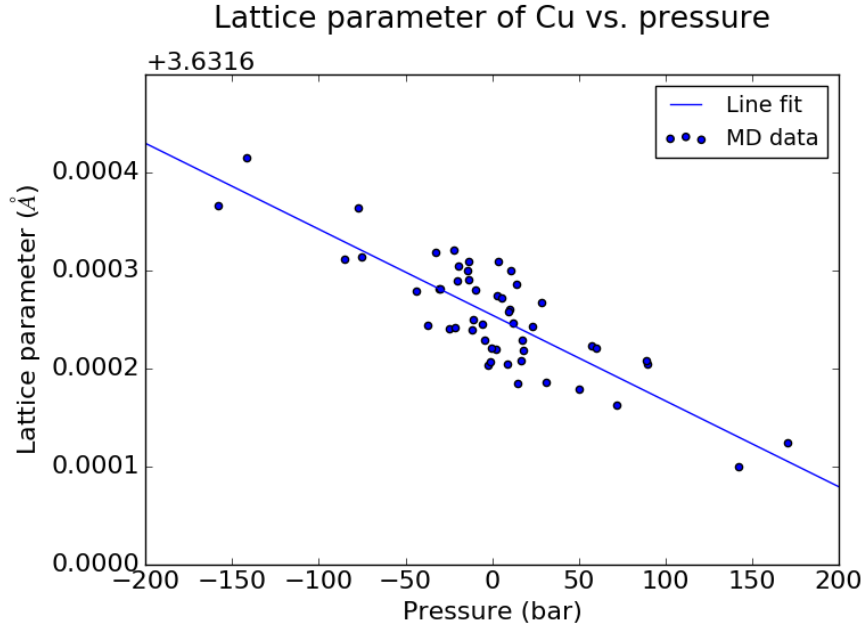
Figure 3.3: *The lattice parameter of the Cu Mishin EAM1 potential as a function of pressure.*

The same procedure was applied to the Nb Fellinger EAM potential [80]. At s.t.p. niobium is a BCC material with lattice parameter of 3.3004 Å[81]. Figure 3.4 shows the lattice parameter of the Nb EAM potential as a function of pressure. By fitting a line to this data and taking the y-intercept as the lattice parameter, the lattice parameter of the Nb Fellinger EAM potential is reported here as $a = 3.33069 \pm 2 \times 10^{-5}$ Å, where the error is one standard deviation.

3.3 The Debye-Waller effect in molecular dynamics

In the case of MD, an x-ray diffraction pattern can be simulated by performing a discrete Fourier transform of the atomic positions. In this work, the discrete
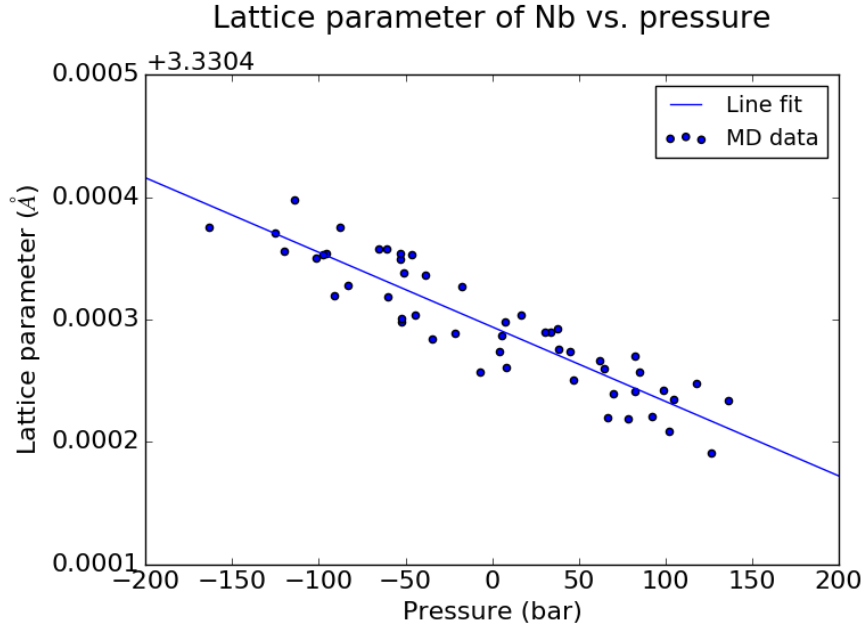
Figure 3.4: *The lattice parameter of the Nb Fellinger EAM potential as a function of pressure.*

Fourier transform was performed using the SonOfHoward code written by Andrew Higginbotham.

Each Fourier transform calculation yields a single intensity point in reciprocal space. For a crystal, the majority of the reciprocal space intensity is contained in the volume around the reciprocal lattice points. It is therefore most computationally efficient to calculate the Fourier transform at points nearest to the reciprocal lattice points. In the kinematic approximation, the intensity of an ideal Bragg reflection in one direction takes the form

$$y = \frac{sin^2(Nx)}{sin^2(x)} \tag{3.2}$$

70

where $y \propto I$, x is the reciprocal distance from the centre of the diffraction peak, and N is the number of unit cells in the x direction,[82]. An image of this function is shown in figure 3.5. The width of the central peak is $\frac{2\pi}{N}$, where the width is twice the x value between the highest peak and the first minimum. Since the majority of the intensity is contained within this central region it is most efficient to calculate the intensity in this area only, discounting the "wings" of the function. This is especially true in three dimensions; a doubling of the width considered results in an eight-fold increase in volume considered, and thus an eight-fold increase in computation required to calculate a discrete Fourier transform with the same resolution.
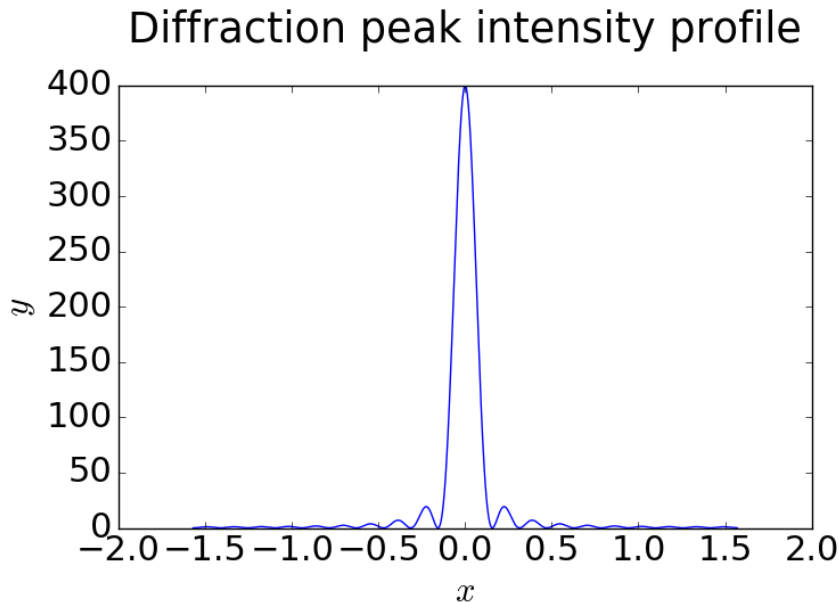
Figure 3.5: *Equation 3.2 with N = 20.*

In order to measure diffraction peak intensities from MD efficiently, the peakfinder

code was written. The basic work flow of this code is shown in figure 3.6. The code begins by estimating the reciprocal space positions of the diffraction peaks using the user-defined structure and lattice parameter i.e. peakfinder will not search for forbidden reflections. The code will predict as many reflections as instructed by the user. The user may toggle the presence of negative values for h k l. The user may also toggle the presence of the non-physical (0 0 0) reflection.

Since the simulated crystals considered here are typically under compression, the code then searches for the location of a single peak along each of the reciprocal space directions k_x k_y and k_z. This is done by performing a 1-dimensional discrete Fourier transform (1D-DFT) from $(c_{x0}h \quad c_{y0}k \quad c_{z0}l)$ to $(c_{x1}h \quad c_{y1}k \quad c_{z1}l)$, where c_0 is the user-defined undershoot factor of the peak position, c_1 is the user-defined overshoot factor of the peak position, and x y z correspond the the k_x k_y k_z co-ordinates, respectively. The user also defines the number of reciprocal space points calculated between these two points. By allowing the user to define these parameters, the user is given fine control over the size of the computation and can thus leverage their pre-existing knowledge of the MD system to efficiently manoeuvre the code.

Once these first compression-finding 1D-DFT's have been completed, the maxima are used to estimate the overall compression in the sample along k_x k_y k_z. The compression factor $S = p_{max}/p_{init}$ is calculated along each direction, where p_{max} is the point of maximum intensity in the 1D-DFT line out, and p_{init} is the initial guess of the position of the diffraction peak. These compression factors are then applied to the full list of initial guesses of peak positions so that each initial $(h$ k $l)$ becomes $(S_x h \quad S_y k \quad S_z l)$.

A further set of 1D-DFT's is performed, this time over each individual peak.

The aim is to find each peak centre individually. A 1D-DFT is performed over each k_x k_y k_z direction; the maxima of each 1D-DFT is used as the peak-centre reciprocal space position in each corresponding dimension. The step size in each dimension is dk_x, dk_y and dk_z.

A 3-dimensional discrete Fourier transform is then performed in the immediate vicinity of the nominal peak-centre determined from the previous three 1D-DFT's. The idea is to investigate the space between the maxima and the next nearest point in the previous 1D-DFT's. A 3-dimensional cuboid is defined in reciprocal space centred on the nominal peak centre. The cuboid has side lengths of $2dk_x$, $2dk_y$ and $2dk_z$, using the values from the previous three 1D-DFT's. The maxima of this 3D-DFT is used as the final peak-centre value.

Now that the centre of the peak has been found to a high degree of accuracy, the final 3D-DFT is performed over the full peak. The width of the peak is defined by the user; this is because more complicated MD systems have poorly resolved peak edges. Instead, the user defines the peak edge such that the full peak is enclosed within the 3D-DFT cuboid. The resolution of the 3D-DFT is also set by the user so that a lattice of points is defined with cell volumes of $dV = dk_x dk_y dk_z$. The intensities of the DFT at each point on the lattice is summed and then multiplied by dV to give an approximate value of the integrated intensity I. The higher the resolution of the lattice (i.e. the smaller dV) the closer the approximation approaches the actual integrated intensity of the peak.

The integrated intensities are now ready to be used to calculate temperature, using the Debye-Waller effect discussed in section 2.3.2. Since the atoms in an MD system obey a Boltzmann distribution, the classical form of the equation for the
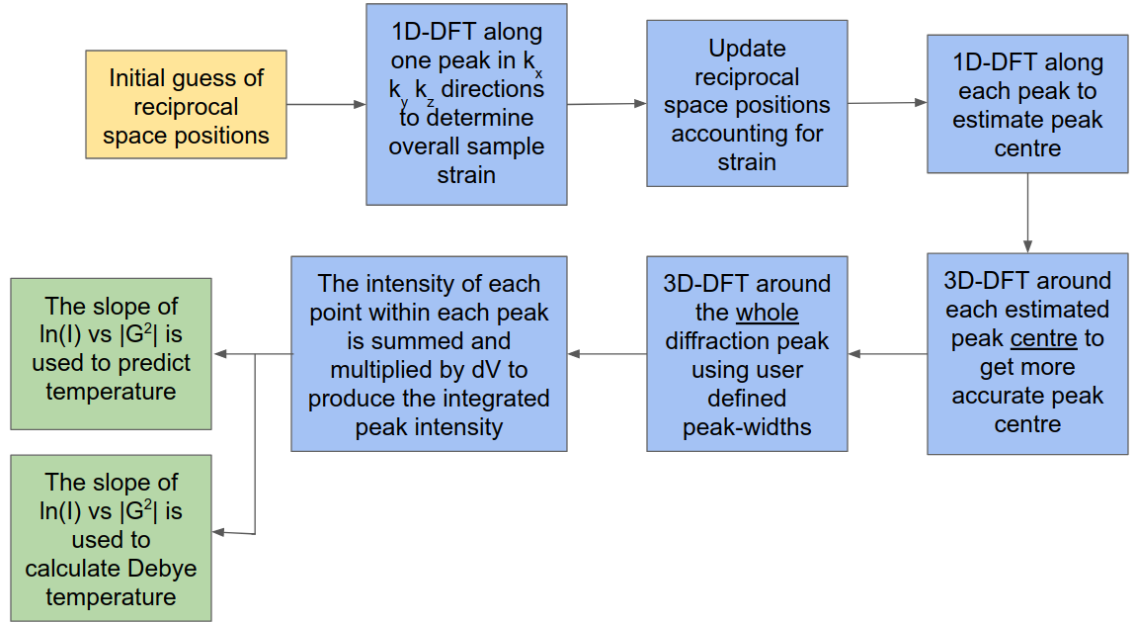
73

Figure 3.6: *The peakfinder code work flow, showing the major operational stages.*

Debye-Waller effect is used.

$$I(T) = I_0 exp(-2M) \tag{3.3}$$

$$2M = \frac{3h^2 N_A |\mathbf{G}|^2}{m k_B \Theta_D} \left[\frac{T}{\Theta_D} \right] \tag{3.4}$$

By taking the natural log of integrated intensities, the following linear equation is produced.

$$ln\left(\frac{I(T)}{I_0}\right) \frac{1}{|\mathbf{G}|^2} = -\frac{3h^2 N_A}{m k_B \Theta_D^2} T \tag{3.5}$$

Thus, a line fitted to $ln\left(\frac{I(T)}{I_0}\right)$ vs. $|\mathbf{G}|^2$ has a slope equal to the right hand side of equation 3.5. The only remaining unknown quantities are Θ_D and T. By substituting in for a value of Θ_D, a measurement of T can be inferred. Alternatively, one can input a value of T to infer Θ_D.

Note that I_0 here is the intensity from the simulated (0 0 0) "reflection"; this reflection is an artefact of the Fourier transform and is not physical. It is used here to normalise the intensities of diffraction. Alternatively, the diffraction intensity at 0 K can be used for I_0. Furthermore, the normalisation of the intensities has no impact on the temperature measurement technique at hand, since the effect of intensity normalisation on the plot of $ln(I(T))$ vs. $|\mathbf{G}|^2$ is to simply subtract the constant $ln(I_0)$ from each value of $ln(I(T))$; the slope remains unchanged, and thus the temperature measurement is also unchanged.

Figure 3.7 shows the diffraction intensities from simulated Cu using the Cu Mishin EAM1 potential [78]. A cube with side length of $N = 60$ conventional unit cells was thermalised for 10^4 timesteps, with each timestep corresponding to 1 fs. The thermalisation was performed using a Nosé-Hoover thermostat set for 300, 600, 900, and 1200 K. This is in line with the work of Murphy et. al. [37], whose results are independently verified here. By using the final temperature of the 300 K simulation, as reported by LAMMPS itself, equation 3.5 was used to determine the Debye temperature of the simulation $\Theta_D = 315$ K.
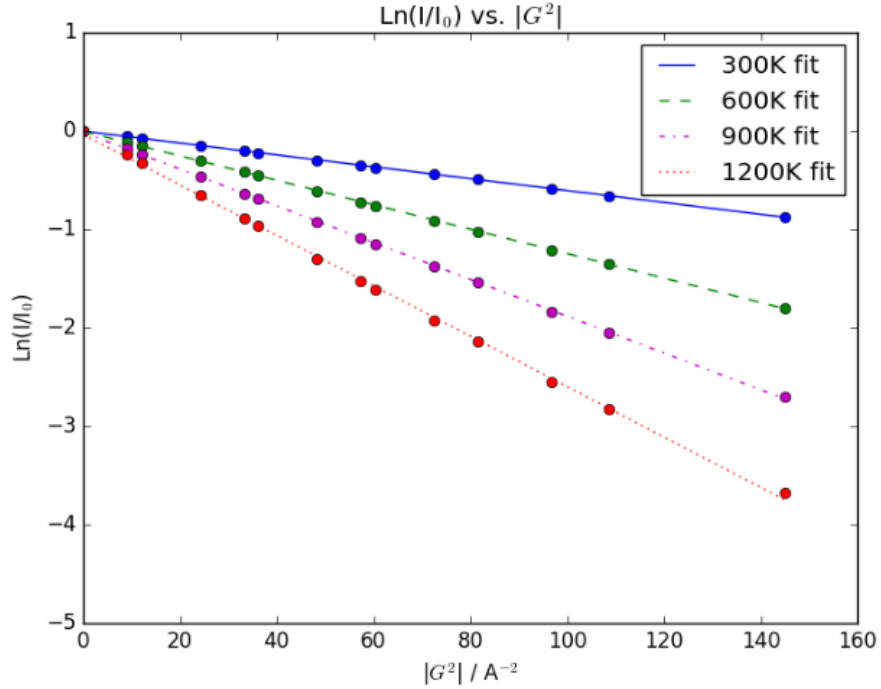
Figure 3.7: *The simulated diffraction intensities for a cube of Cu with N = 60 conventional unit cells in each dimension, at temperatures of 300, 600, 900, and 1200 K. The Cu Mishin EAM1 potential is used [78]. The x-axis shows the square of the reciprocal space position for each peak. As temperature increases, the diffraction intensity diminishes quicker due to the Debye-Waller effect.*

3.4 Debye temperature as a function of the number of atoms

The number of phonon modes available in an atomic system is dependent on the number of atoms. Therefore it is expected that there is a minimum requirement for the number of atoms in a simulated solid in order to adequately approximate the phonon distribution of a large sample.

A simulation was performed on a sample of copper with conventional cell dimensions

NxNxN in order to investigate this, where N was varied between 10 and 100 in steps of 10. Figure 3.8 shows the x-ray diffraction Debye temperatures for simulations of various N. At each N, three simulations were performed using different initial velocity distributions; this illustrates the variance in results caused by slightly different starting conditions. An additional simulation was performed for $N = 200$ to verify Debye temperature convergence.
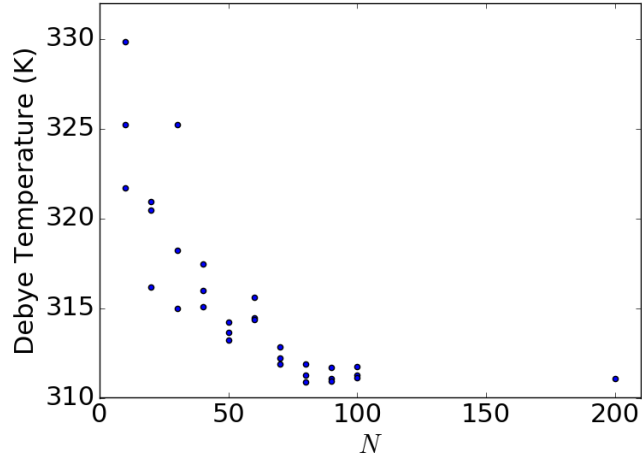

Figure 3.8: _The Debye temperature of a box of $4N^3$ atoms at 300 K using the Cu Mishin EAM1 potential as a function of N, where N is the number of lattice sites in each simulated Cartesian dimension._

It can be seen that the Debye temperature asymptotically approaches a value of 311 K at large N. It can also be seen that the standard deviation of the results between temperature seeds decreases with N; this result is explained by recalling that the measure of Debye temperature here depends on the atomic displacement from the lattice sites. If there are more atoms to sample, the atomic displacement distribution is more likely to accurately resemble the expected atomic displacement distribution for an infinite sample, and thus the scatter between Debye temperature

results will be reduced. These results suggest that simulations should employ $N \geq 80$ to produce a sufficiently sampled phonon distribution.

An physical explanation of this result is produced by considering a classical 1-D chain of atoms performing simple harmonic motion. The phonon frequencies available to this system are related to wavenumber k by the relation

$$\omega(k) = \frac{k_B \Theta_D}{\hbar} sin\left(\frac{ka}{2}\right) \tag{3.6}$$

where a is the atomic spacing [38]. If there is only one atom in the system there will only be one phonon mode available at $k = 0$. When two atoms are present, an additional mode is available at $k = \frac{\pi}{a}$. In general, for a 1-D chain of $N > 2$ atoms, there are N oscillation modes available with wavevcetors k_n such that

$$k_n = \frac{n-1}{N-1}\frac{\pi}{a} \tag{3.7}$$

where n is an integer number between 1 and N.

Each phonon mode will be occupied according to the Boltzmann distribution

$$f = e^{-\hbar\omega(k)/(k_B T)} \tag{3.8}$$

Note that the $k = 0$ phonon is unoccupied in this analysis; this phonon mode corresponds to a translation of the 1D-chain and therefore is not meaningful with respective to the average frequency of oscillation within the system. The Boltzmann occupation is calculated for each mode using equation 3.8 and then normalised by the sum of all occupations according to

$$Z(k) = \frac{f(k)}{\sum_n^N f(k_n)} \tag{3.9}$$

This normalisation ensures that the sum of all probabilities of occupation is 1. The mean frequency of oscillation can now be calculated by

$$\bar{\omega} = \sum_{n=1}^{N} \omega(k_n)Z(k_n) \tag{3.10}$$

The average frequency is proportional to the Debye temperature. Figure 3.9 shows the convergence of Debye temperature as the number of atoms N increases.
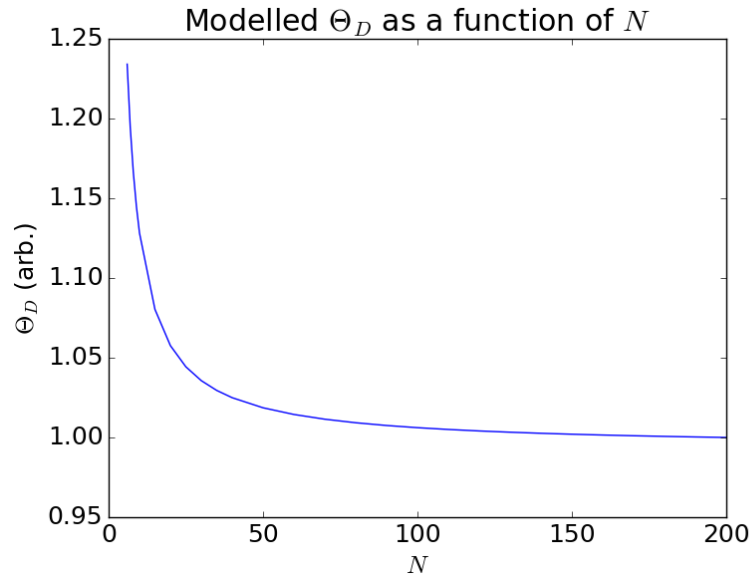

Figure 3.9: *A classical model showing the relationship between Debye temperature Θ_D and the number of atoms in a 1-D chain.*

It has therefore been shown that a small number of atoms results in an over prediction of the Debye temperature of the solid. The average frequency of oscillation of a small system will be such that the material potential looks "stiffer". This

stiffer-looking potential is the cause of the higher predicted Debye temperature. If more atoms are added to the chain the average frequency is lowered, causing the Debye temperature to converge. From this analysis, a simulated sample requires $N \geqslant 100$ atoms to produce an appropriately populated phonon distribution. This result will be carried forward into future investigations.

3.5   Hydrostatic compression of Cu and Nb

A box of 100x100x100 Cu atoms with periodic boundary conditions was simulated with varying lattice parameters. By intentionally using a shorter lattice parameter, the system is subjected to a hydrostatic compression. The lattice parameter is selected such that $a_l = ca_{l0}$, where c is the factor by which the lattice constant is shortened and a_{l0} is the original lattice parameter of Cu at $P = 0$ bar, as calculated in section 3.2. The final volume of the sample, V as a fraction of the uncompressed volume V_0, is given by

$$\frac{V}{V_0} = (1 - c)^3 \tag{3.11}$$

The value of V/V_0, referred to here as the compression fraction, was selected at values between 0.80 and 1.00.

The Cu Mishin EAM1 potential was used yet again, and the box was thermalised for 10^4 timesteps of 1 fs each. The analysis described in section 3.3 was performed on these simulations, using the MD temperature as an input to determine the Debye temperature. The Debye temperature for each compression fraction is shown in figure 3.10. A third degree polynomial is fit to the data of the form

$$\Theta_D = A\left(\frac{V}{V_0}\right)^3 + B\left(\frac{V}{V_0}\right)^2 + C\left(\frac{V}{V_0}\right) + D \qquad (3.12)$$

where $A = -940.77$, $B = 4409.42$, $C = -6459.18$, and $D = 3300.72$. The polynomial was fitted using the "polyfit" function of the Python module NumPy. This model for Debye temperature as a function of compression is compared to several other models found in the literature; these models were compiled by Murphy et. al. [37], though the implementation of these models appears to be incorrect. The simplest model approximates that Γ/V is constant, where Γ is the Gruneisen parameter [83]. The model of Pandya et. al. is derived from perturbation theory [84]. The models from Ramakrishnan et. al [85] and Walsh et. al. [86] are derived from fits to experimental data.

The MD model predicts a Debye temperature at s.t.p. of $\Theta_D = 309.9$ K. This is slightly lower than the literature value of 320 K [87]. In order to best compare the behaviour of Θ_D as a function of V/V_0 given by the different literature models, the uncompressed Debye temperature for the literature models is set to 309.9 K in figure 3.10. The difference between the MD Debye temperature model presented here and other models found in the literature highlights the fact that MD is not a perfect representation of real-life materials. In later sections in this chapter, the MD model for Debye temperature will be used to infer temperature. This is useful since the results will give a strong indication of the accuracy of the temperature-measurement technique. The literature Debye temperature models will also be used so as to give an indication of error associated with using different Debye temperature models.

The same procedure was carried out for BCC Nb using the Nb Fellinger EAM potential, though this time a fifth order polynomial was fitted to the data with the
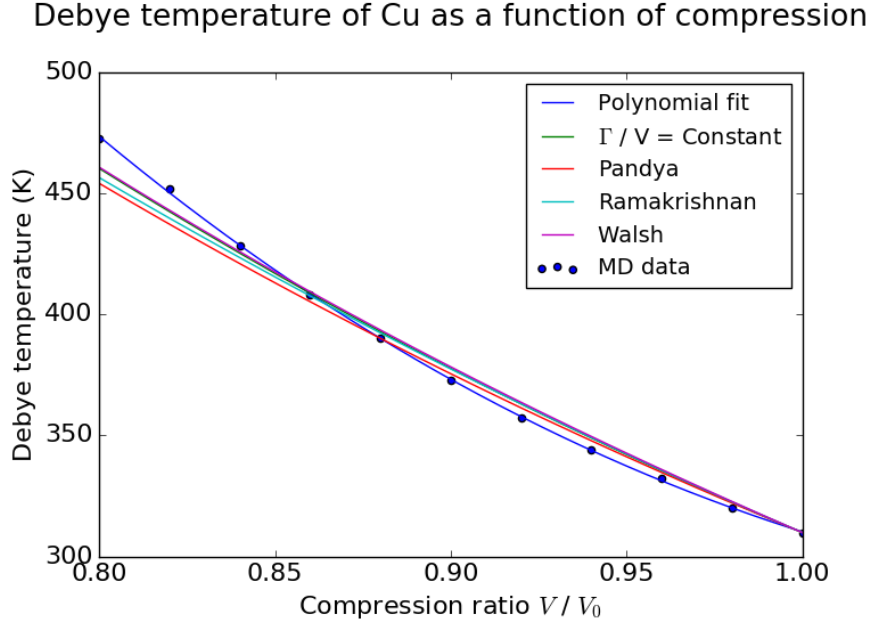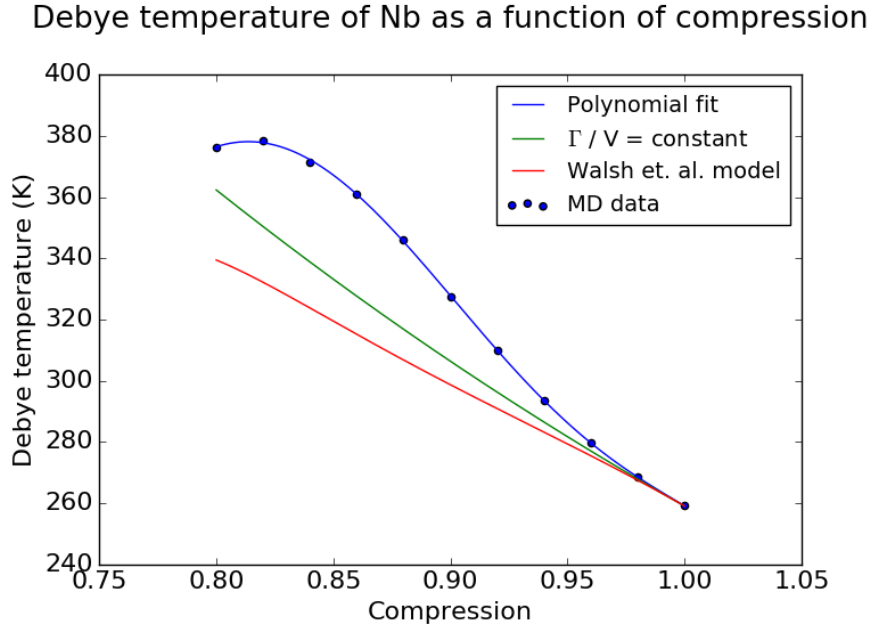
Figure 3.10: *The Debye temperature of simulated Cu as a function of hydrostatic compression. A third order polynomial is fit to the data.*

following equation

$$\Theta_D = A\left(\frac{V}{V_0}\right)^5 + B\left(\frac{V}{V_0}\right)^4 + C\left(\frac{V}{V_0}\right)^3 + D\left(\frac{V}{V_0}\right)^2 + E\left(\frac{V}{V_0}\right) + F \qquad (3.13)$$

where $A = -769547.13$, $B = 3387086.89$, $C = -5920835.77$, $D = 5134767.61$, $E = -2208100.45$, and $F = 376887.89$. The results are shown in figure 3.11. The MD model predicts the Debye temperature of uncompressed Nb to be 259 K, compared to the experimentally determined value of 276.6 K [88]. Other models from literature are also shown, including the approximation that Γ/V is constant [83]. The model from Walsh et. al. is fitted from experimental data.

Figure 3.11: *The Debye temperature of simulated Nb as a function of hydrostatic compression. A fifth order polynomial is fit to the data.*

At large compressions the MD model predicts that the Debye temperature will inflect and begin to decrease. A similar phenomenon, observed instead in FCC Cu uniaxially compressed along [1 1 1], has been attributed to phase transitions by Murphy et. al. [37]. There are no predicted phase transitions in Nb under the hydrostatic conditions present in figure 3.11 [89] and so this argument is not satisfactory in this case. This behaviour indicates that this potential may make poor predictions of real-life behaviour at high compressions. The MD Debye temperature model also departs from the literature models, though the literature models also disagree with each other, much more so than is seen above for Cu.

3.6 Static uniaxial compression

Upon uniaxial shock compression, material strength results in a resistance to stress relief along non-shocked directions. High strength materials will thus compress non-hydrostatically, resulting in different lattice parameters along x, y and z. The impact of material strength on Debye-Waller thermometry is not immediately obvious, and requires investigation.

A box of 100x100x100 conventional unit cells of Cu atoms was simulated using the Mishin EAM1 potential, as before. The lattice was compressed along the [1 1 1] direction up to $V/V_0 = 0.86$. This direction was chosen to avoid a known phase transition, which causes FCC materials to transition to a BCC phase [90]. The Debye-Waller analysis of section 3.3 was carried out on the compressed samples. A plot of $ln(I(T))$ vs. $|\mathbf{G}|^2$ is shown in figure 3.12.

The intensities no longer lie on a line. This is caused by an anisotropic Debye temperature. Along the compression direction, the inter-atomic bond has stiffened, resulting in a heightened Θ_D. This is accompanied by a softening of the inter-atomic bond along the directions perpendicular to the compression direction. The result is a directionally dependent Θ_D, evidenced by the divergence in Debye-Waller response seen in figure 3.12.

An effective value for Θ_D can still be calculated from the slope of the line of best fit. The Debye temperature calculated for uniaxial compressions is shown in figure 3.13. Below $V/V_0 = 0.86$, stacking faults were generated in the sample. This plasticity is the likely cause of the divergence between measured hydrostatic and uniaxial Debye temperatures at $V/V_0 < 0.92$; stacking faults have the effect of
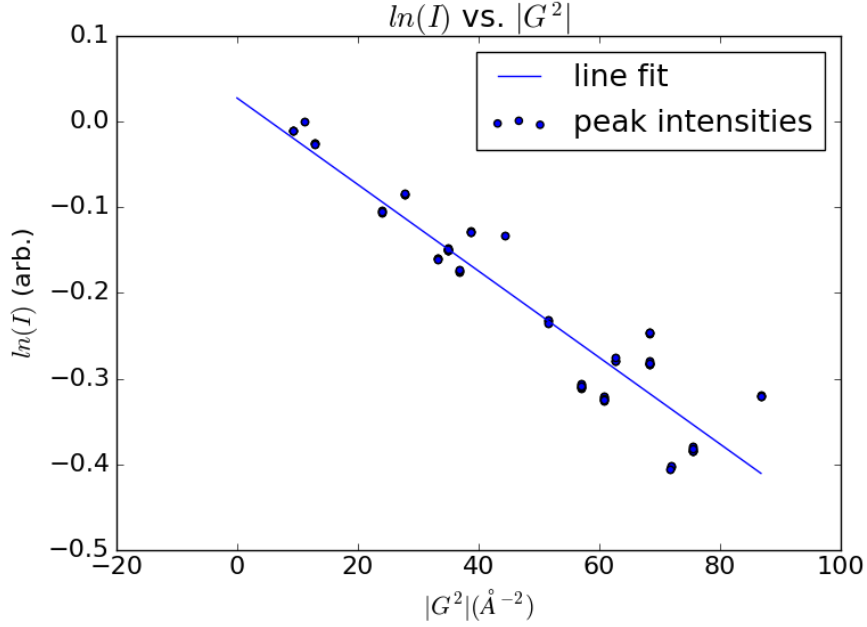
Figure 3.12: *Debye-Waller plot for simulated Cu uniaxially compressed along* [1 1 1] *to* $V/V_0 = 0.9$.

splitting intensity away from a diffraction peak [91], which, according to these results, causes a difference in Debye-Waller behaviour compared to a non-defective sample. When $V/V_0 > 0.92$, the measured Debye temperature is slightly lower for uniaxial compression compared to hydrostatic compression, though the difference is very small. Figure 3.14 shows the temperature measured using the hydrostatic model of Θ_D derived from MD in section 3.5. At $V/V0 = 0.9$, before the apparent onset of plasticity, the difference between the measured T and the true value of T is 2.5%. This is evidence that the anisotropy in Θ_D has a minor effect on temperature measurement. What's more, the uniaxial compressions considered here are rather extreme compared to what is observed experimentally; a typical strength observed

on a laser shock experiment corresponds to $V/V_0 > 0.98$ [60]. Material strength, therefore, will have little impact on the Debye-Waller thermometer.
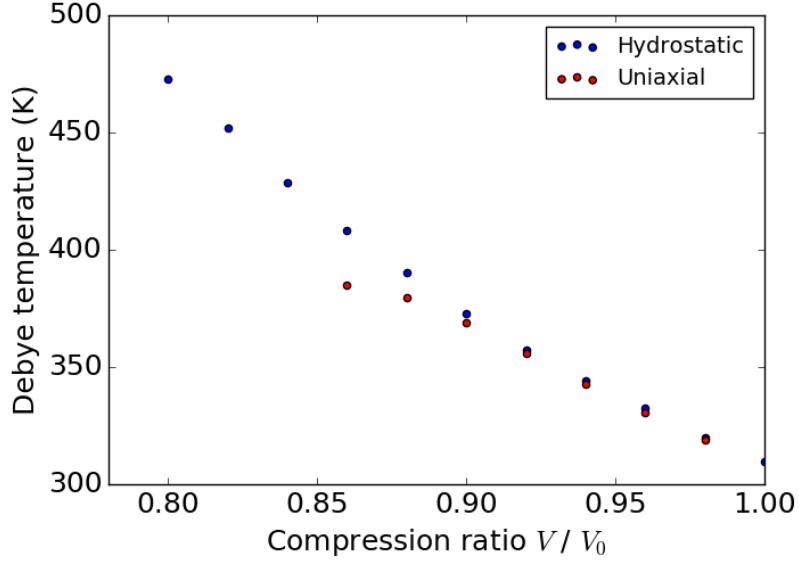
Figure 3.13: *A comparison between the Debye temperature of hydrostatically compressed Cu vs. Cu compressed uniaxially along* [1 1 1].

3.7 Elastic shock compression

The passage of a shock-wave through a material is a disruptive occurrence. An elastic shock with relatively low particle velocity u_p will cause a uniaxial compression of the material. At higher values of u_p, plasticity will be activated, relieving the uniaxial pressure into a more hydrostatic compression. Elastic shocks are investigated in this section and compared to the static uniaxial compressions of section 3.5. The effects of plasticity will be discussed later in section 3.9.
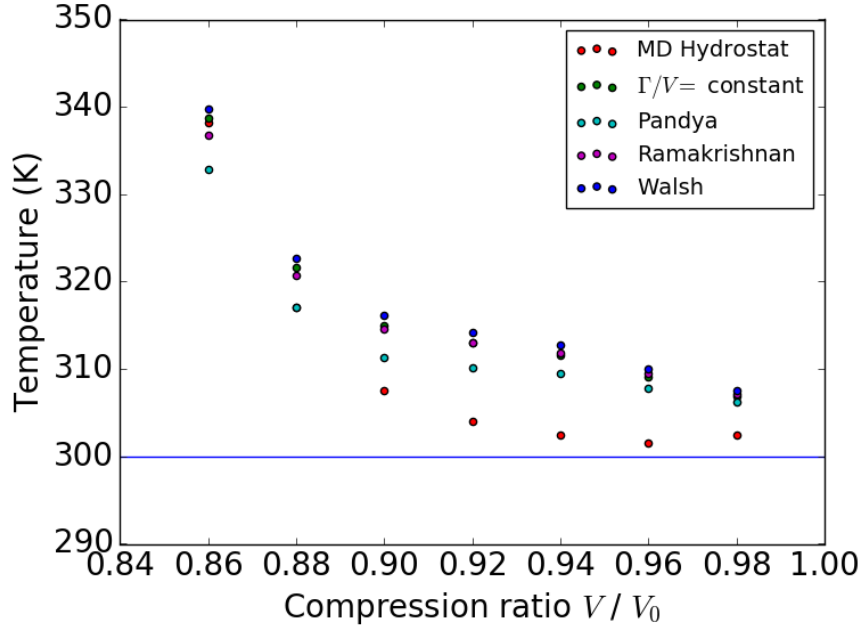
Figure 3.14: *Temperature measured from the simulated intensities of diffraction using a variety of Debye temperature models. The sample is simulated Cu at 300 K compressed along* [1 1 1].

A 100x100x210 box of Cu was simulated using the Cu Mishin EAM1 potential, with the [1 1 1] direction oriented along z. Periodic boundaries are enforced in the x and y directions; a non-periodic boundary is enforced along z. One 100x100x5 face at the base of the simulation was designated as a piston; this is used to drive the shock-wave through the sample. At the top of the simulation another 100x100x5 face was designated as the back wall; this back wall prevents the ejection of atoms from the rear of the simulation. The atoms in both the piston and back wall are frozen in place. They may interact with other atoms, but their positions are not updated. All other atoms in the simulation are designated as the bulk.

At first the bulk atoms were thermalised to 300 K over a period of 10^4 timesteps

of 1 fs. The piston atoms were then given a constant velocity u_p along the z direction. As a result of the "freezing" of these atoms, their velocity remains constant throughout the simulation. The atoms in the remaining bulk are compressed by the resulting shock wave. Values of u_p between 0.3 and 0.9 km s$^-$1 were used. At $u_p = 0.2$ km s$^-$1, a clear shock wave does not form. At $u_p = 1.0$ km s$^-$1, plasticity is clearly activated in the form of stacking faults; the plasticity was identified using the Common Neighbour Analysis [92] routine implemented in the Ovito visualisation package [93].

A central chunk of 100x100x100 unit cells was extracted from the bulk for Debye-Waller analysis as described in section 3.3. Figure 3.15 shows the Debye-Waller plot for $u_p = 0.6$ km s^{-1}. The measured values of T according to all of the Θ_D models used in section 3.5 is shown in figure 3.16. The difference between measured T and the real T at this u_p, using the MD hydrostatic model, is +6.1%. This result will now be compared with the static uniaxial compression of the previous section.

3.8   Simulated temperature measurement overview

Temperatures have been calculated for simulated Cu undergoing static uniaxial compression and elastic shock compression. Figure 3.2 shows the error associated with representative temperature measurements. The percentage error e here is

$$e = \frac{|T_{DW} - T_{MD}|}{100 \times T_{MD}} \tag{3.14}$$

where T_{DW} is the temperature according to the Debye-Waller measurement, and T_{MD} is the temperature as calculated from atom velocities in the simulation. Each row
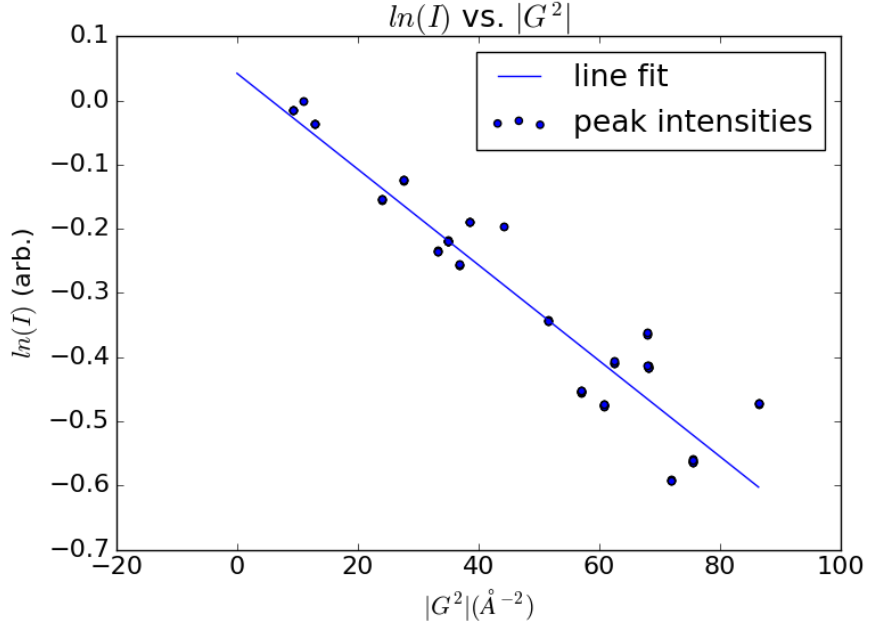
Figure 3.15: *The Debye-Waller plot for Cu elastically shocked along* [1 1 1].

shows the error in calculated temperature using each model of Debye temperature.

	Uniaxial $V/V_0 = 0.9$ % Error in T	Elastic shock $u_p = 0.6$ km s^{-1} % Error in T
$\Gamma/V =$ **constant**	+ 5.0	+ 8.7
Pandya	+ 3.8	+ 7.5
Walsh	+ 4.9	+ 8.6
Ramakrishnan	+ 5.4	+ 9.1
Hydrostatic MD	+ 2.5	+ 6.1

Table 3.2: *The error in measured temperature associated with different Debye temperature models. Two simulation types are considered: static uniaxially compressed, and elastically shock compressed.*

The Hydrostatic MD model was produced in section 3.5 and represents the "true" behaviour of the Cu Mishin EAM1 potential. The other models are based
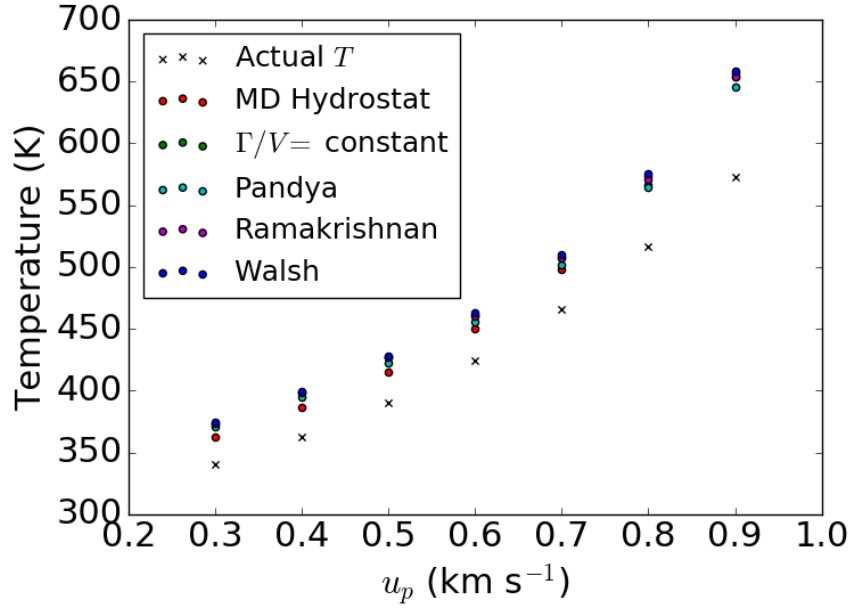
Figure 3.16: *Temperature measured from the simulated intensities of diffraction using a variety of Debye temperature models. The sample is simulated Cu at 300 K compressed along* [1 1 1].

on real Cu. Therefore the MD model shows the best indication of the actual impact of the applied process. Uniaxial compression consistently resulted in a slight over-prediction in temperature. Elastic shock compression, while producing seemingly similar Debye-Waller behaviour as that observed under static uniaxial compression, gave noticeably larger errors. The centrosymmetry parameter [94] associated with atoms in the system indicate higher structural disorder in the case of shock compression compared to uniaxial compression. This higher disorder will cause decoherence in scattered x-rays, resulting in lower observed intensities. This is proposed as the cause of the slight difference observed between the measured temperatures.

By comparing the results of the Debye temperature models of real Cu, some insight can be gained about the error introduced by an inaccurate model of Debye temperature. Interestingly, the difference in error for each model introduces a relatively small scatter in T_{DW}. In the uniaxial case, the difference in error has a maximum value of 1.6% of the material temperature. In the shock case the maximum difference is also 1.6%. This suggests that the thermometry technique is robust with respect to choice of Debye temperature model; however, Cu is a well-studied material. A less popular material may not enjoy such a convergence of models, as seen in section 3.2 with respect to Nb.

3.9 Dislocations and the Debye-Waller effect

Shock compression beyond the elastic limit of a material produces a high density of dislocations. It is known that the presence of dislocations broadens diffraction peaks; however, the impact of dislocations on the Debye-Waller effect is not obvious. This section investigates the impact, if any, that dislocations have on the Debye-Waller thermometer.

3.9.1 Theoretical predictions

The work of Wilkens described in section 2.3.4 was used to build model intensity profiles from crystal with varying dislocation populations. The theory of Wilkens was initially developed for dislocation densities in ambient material. Under shock conditions, the dislocation densities present are expected to be much higher due to the viability of homogeneous nucleation and the onset of plasticity.

The Wilkens equation for diffraction intensity cannot be solved analytically. A numerical code was therefore written to solve the equation. At high dislocation densities the equation becomes very computationally inefficient, and convergence becomes difficult. Figure 3.17 shows the predicted (3 2 1) reflection intensity profiles for crystals containing only screw dislocations. The contrast factor C_s is set to 0.25, which is the maximum value for screw dislocations; recall from 2.3.4 that C_s takes the form $sin^2x\ cos^2x$. This means that the screws are oriented such that they have the maximum possible impact on the diffraction intensity.

The area under each of the curves in figure 3.17 is similar. This result indicates a minimal impact of screw dislocation density on the Debye-Waller effect since the integrated intensity of a single reflection seems largely unaffected by dislocation density; however, the Wilkens model is dependent on both dislocation character and the reciprocal space position of the peak. Therefore, to analyse the predicted effect of dislocations on the Debye-Waller effect, the Wilkens equation should be solved for a variety of peaks with varying contrast factors; this should reveal the full extent of the difference in peak intensities brought about by screw dislocations.

Figure 3.18 shows the relative intensities of various diffraction peaks for different C_s. The ratio of the highest intensity to lowest intensity is 0.976, though it should be noted that these solutions are not fully converged; however, the ratio of highest intensity to lowest intensity was observed to approach 1 with convergence. Each point in this plot represents hours of computation, and so further convergence was not sought due to computational requirements.

Since the diffraction intensities are largely the same across both dislocation density and C_s, the Wilkens model predicts that screw dislocations do not compromise
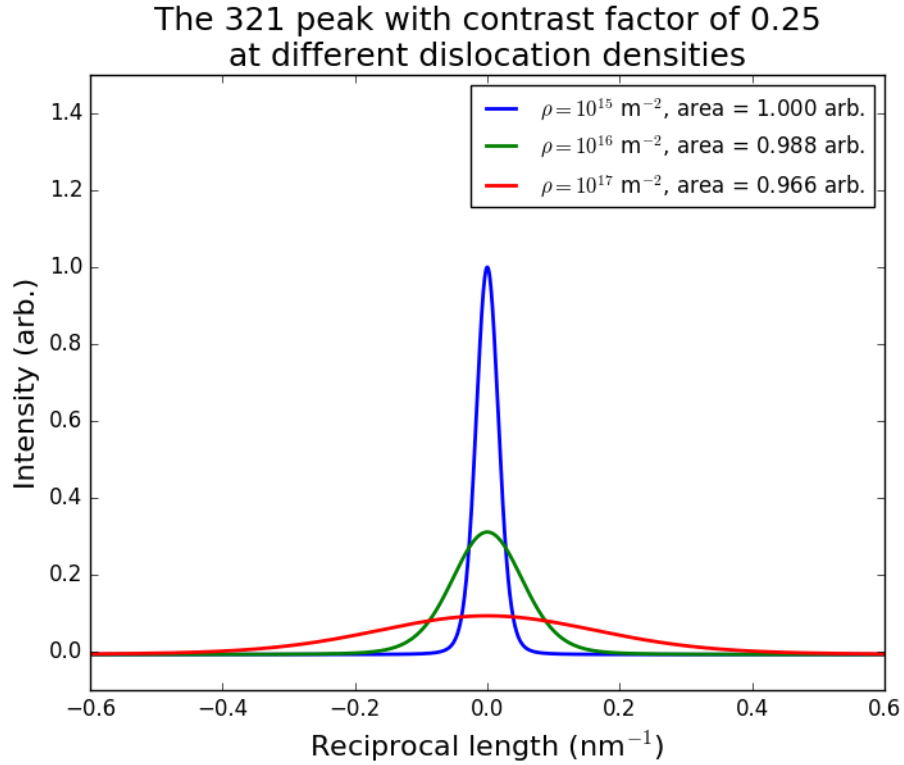
Figure 3.17: *The (3 2 1) reflection for a crystal containing screw dislocations. Each peak corresponds to a different dislocation density.*

the Debye-Waller effect as a means of measuring temperature. This prediction will now be assessed with molecular dynamics.

3.9.2   Simulations of x-ray diffraction from dislocations

Dislocations were generated in MD by shocking a sample of 100x100x100 conventional unit cells of BCC Nb along (1 1 1), using the Nb Fellinger EAM potential. The shocked sample was produced using the Hugoniostat described in section 2.4.3. Similar atomistic simulations of BCC materials have generated dislocations when shocking along (1 1 1) [95]. The dislocation densities were calculated using the DXA
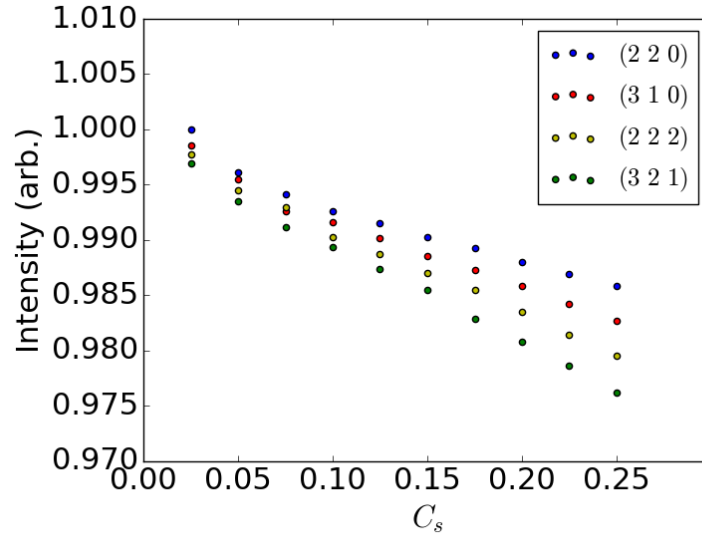
Figure 3.18: *The intensity of a variety of diffraction peaks as a function of C_s.*

module in Ovito [96].

The sample was subjected to 1 Mbar along (1 1 1). Once the sample had reached the desired pressure, the sample was cooled to 20.9 K to "freeze-in" the dislocations and to isolate their effect. If the dislocations have no effect on the Debye-Waller thermometer, as predicted by the theoretical models of the previous section, the temperature measured by the Debye-Waller analysis will be close to 20.9 K. Note that any temperature measurement here will require a Debye temperature model for the Nb Fellinger EAM potential. The model developed in section 3.5 is used here.

The Debye-Waller plot of the cooled, dislocated sample is shown in figure 3.19. The diffraction profiles were found to be much broader than in a non-dislocated sample. The slope from the Debye-Waller plot gives a temperature of 218 K. Contrast this with figure 3.20, where a sample of pure BCC Nb with no dislocations,

also at 1 Mbar, is also analysed. The slope from this Debye-Waller plot gives an accurate temperature measurement of 21.5 K. Thus the dislocations are decreasing the intensity of diffraction; more than that, the behaviour resembles the effect of temperature on the diffraction intensities such that a "dislocation temperature" is observed.
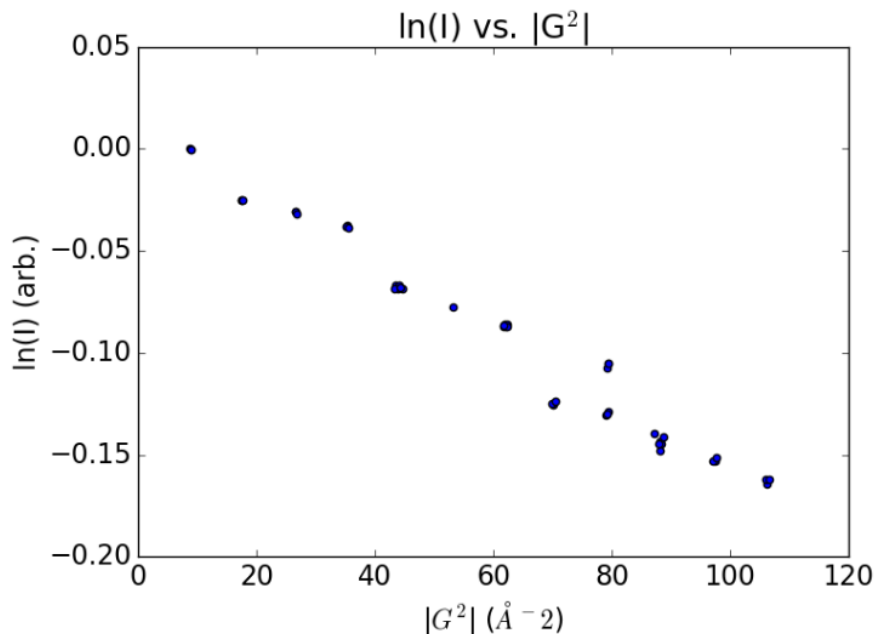

Figure 3.19: *The Debye-Waller plot for a dislocated sample of Nb at 1 Mbar. The sample temperature is 20.9 K, but the temperature calculated from the slope is 218 K.*

Attempts were made to characterise the additional temperature recorded as a function of the dislocation density. To generate different dislocation densities, a simulated sample of Nb was shocked along (1 1 1) as before, though this time to 800 kbar. This is an attempt to produce as low a number of dislocations as possible, and 800 kbar is the lowest pressure investigated at which dislocations form. To try to
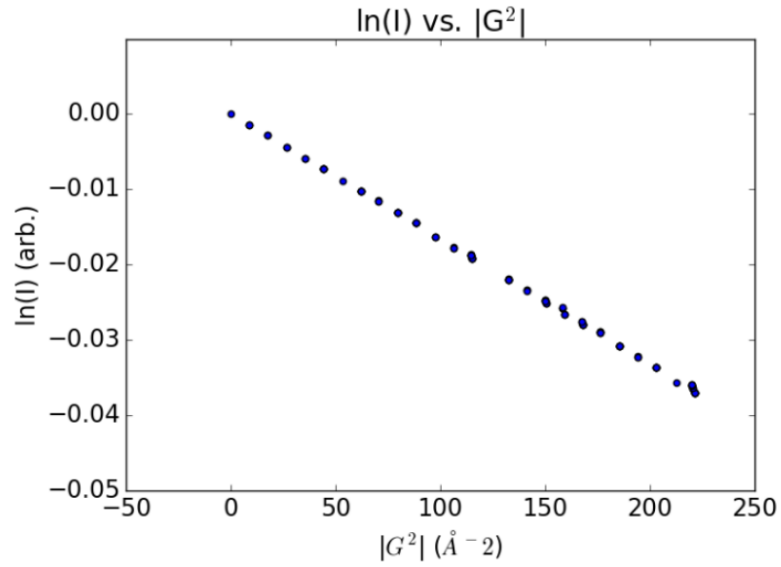
Figure 3.20: *The Debye-Waller plot for non-dislocated Nb at 1 Mbar. The sample temperature is 20.12 K, and the temperature calculated from the slope is 21.5 K.*
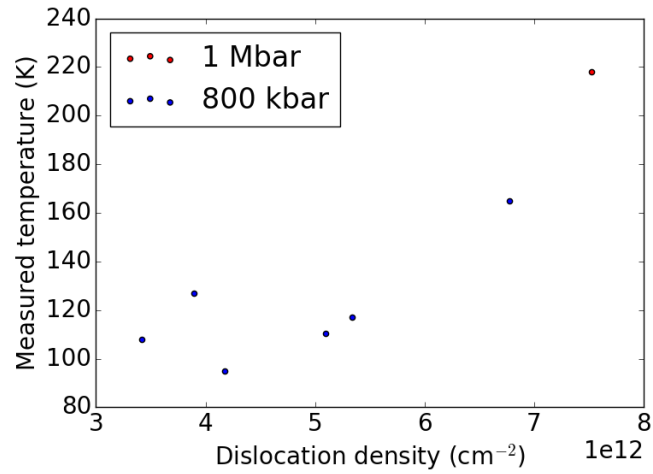

Figure 3.21: *The measured temperature of 800 kbar dislocated Nb at 10.8 K, and 1Mbar dislocated Nb at 20.9 K, as a function of dislocation density.*

96

decrease the dislocation density further, the compressed simulated sample was heated to $T = 1600$ K and left to anneal for 0 to 50 ps. While this did produce a variety of dislocation densities in the sample, no clear relationship between dislocation density and annealing time were observed. The Debye-Waller analysis was then performed on these samples.

Figure 3.21 shows both the 1 Mbar and 800 kbar data. The general trend indicates that the additional measured temperature increases with dislocation density. The form of this dependency is not expected to be simple. As Wilkens points out, the orientation of dislocations with respect to the diffracting plane will play a role in the appearance of the diffraction profile, as will the edge-screw character of the dislocations.

The dislocation densities present in these simulations are very high when compared to those envisioned by the theory of Wilkens. The Wilkens model makes the implicit assumption that the dislocation density is low enough that the dislocation cores do not interact with one another, which may no longer be a safe assumption upon shock compression.

These results indicate that the Wilkens theory breaks down at high dislocation densities. Dislocations on laser shock experiments will therefore cause a substantial over-measurement of temperature by the Debye-Waller thermometer.

3.10 Conclusions

The efficacy of using the Debye-Waller effect to measure temperature has been analysed using molecular dynamics simulations and simulated diffraction patterns.

The complexity of the systems analysed increased gradually, starting with a simple perfect crystal and finishing with dislocated shocked crystals at high pressures. The purpose of these investigations was to study the confounding potential of a variety of phenomena and measure their impact on the Debye-Waller thermometer.

The chapter began with a critical assessment of previous work undertaken by Murphy et al [37]. It was found that the simulation conditions used by Murphy et al resulted in an under sampled phonon distribution in the simulated sample; as a result, the Debye temperature of 315 K reported by Murphy et al for the Cu Mishin EAM1 potential was incorrect. It has been shown that a box size of at least 80 conventional unit cells is required to adequately populate the phonon distribution. At 100 conventional unit cells, the Debye temperature of uncompressed Cu using the Cu Mishin EAM1 potential is 311 K. This is slightly lower than the experimental value for Cu of 320 K. The more general observations by Murphy et al of the decrease in diffraction intensity due to temperature and compression were verified.

The impact of material strength on the Debye-Waller effect was investigated by uniaxially compressing simulated Cu along the [1 1 1] direction to $V/V_0 = 0.86$. An anisotropic Debye temperature was observed. The Debye temperature was observed to increase along the compression direction [1 1 1] and decrease in directions perpendicular to [1 1 1]. This resulted in a change of Debye-Waller behaviour. At $V/V_0 = 0.9$, the error in temperature measurement introduced by strength was +2.5%. Uniaxial compression can also be expressed as the ratio of $a_\perp$ (the lattice parameter perpendicular to the compression direction) to $a_\parallel$ (the lattice parameter along the compression axis). This is a useful measure when comparing with experiment. In these uniaxial simulations, the lattice parameter

ratio is equivalent to V/V_0, and therefore when $a_\perp/a_\parallel = V/V_0 = 0.9$, the error in temperature measurement is still $+2.5\%$. Experimentally, lattice parameter ratios are typically observed to be $a_\perp/a_\parallel > 0.98$ [60]. Strength is therefore not thought to be a major source of error for the present temperature measurement scheme.

Simulated Cu was elastically shocked along [1 1 1]. The impact on the Debye-Waller effect was similar to the effects observed by uniaxial compression, though the error of temperature measurement was larger at $+6.1\%$. This is attributed to the structural disorder added to the system upon the passage of the shock front.

To measure temperature effectively using the Debye-Waller effect, a model of Debye temperature under compression is necessary. Four distinct models for Cu were compared. The variance in predicted temperature was less than 2%, indicating that well-developed Debye temperature models are sufficient for x-ray diffraction temperature measurement. Not all materials benefit from the popularity experienced by Cu and so their Debye temperature models may be more poorly constrained.

Dislocated simulations of Nb were investigated. It was found that at dislocation densities greater than 4×10^{12} cm^{-2}, dislocations cause a similar decrease in intensity as that observed by the Debye-Waller effect. This is a confounding factor for the thermometry technique, as the effect of dislocations is indistinguishable from the effect of temperature. This result is in conflict with the theory of Wilkens [63] which predicts no impact of dislocations on the Debye-Waller effect. Wilkens' model makes the assumption that dislocations are sufficiently separated such that the strain fields from each dislocation do not interact; it is suggested here that this may not be valid at high dislocation densities such as those observed on a laser shock experiment, though this conclusion requires further substantive evidence. In any case, the results

of these simulations indicate that the Wilkens model is not valid at high dislocation densities.

Out of all the confounding phenomena investigated, the presence of dislocations will have the highest impact on the Debye-Waller thermometer. Both material strength and choice of Debye model are predicted to have only a slight impact on the efficacy of the tool.

Chapter 4

Experimental Investigation of Temperature Measurement using the Debye-Waller Effect

In the previous chapter, high pressure states of matter were simulated using molecular dynamics, and the confounding phenomena affecting Debye-Waller thermometry investigated. While such analysis gives valuable insight at low cost, the development of an experimental diagnostic is the ultimate aim. A complementary investigation should therefore be performed with the aim of revealing additional challenges of an experimental nature.

4.1 Design Considerations

No laser shock experiment has previously been published dedicated to the exploration of the Debye-Waller thermometer. The principles of an appropriate experimental design are thus yet to be defined. The necessary considerations are discussed here.

Lattice structure of the probed material

A large number of reflections are desired to populate the final Debye-Waller plots, similar to the plots found throughout chapter 3. Diffraction will occur according to the Bragg condition, but for diffraction of a sufficiently high order, the angle θ_B will approach 90° and the diffraction will be indistinguishable.

From the Bragg condition, $\theta_B \propto sin^{-1}(a)$. By increasing the lattice parameter, θ_B is decreased for all reflections, allowing more reflections to be observed. Therefore the lattice parameter of the sample should be large such that θ_B is small and thus more reflections are recorded on the detectors. A BCC material is also desirable since it possesses the highest number of allowed reflections in a given range of θ_B.

Low Debye temperature of the probed material

The intensity of diffraction is related to Debye temperature by $ln(I) \propto \Theta^{-3}$; see equation 2.35. A material with a low Debye temperature should therefore be selected. This ensures that the difference in diffraction intensity between two reflections is large, and therefore more easily detected. What's more, the difference in diffraction intensity at different temperatures will be more easily observed, and so the instrument will be more sensitive to temperature.

Avoidance of material phase transitions

Phase transitions within the sample add unnecessary complexity to the experiment. It is not anticipated that phase transitions will severely impact the technique, though lack of knowledge of material Debye temperature under such conditions may be problematic. Given the prototypical nature of this technique, any known phase transitions should be avoided.

Transparency of sample to x-rays

The chosen material must be transparent enough to x-rays to allow a significant portion of the sample to be probed by the x-ray beam. The x-ray beam must travel into the sample, and diffracted beams must be able to re-emerge with as little attenuation as possible. Unfortunately diffraction intensity increases with the number of electrons Z, whereas transparency decreases with Z. The higher Z chosen, the stronger the diffracted signal, but the diffraction is from a smaller region of the sample.

Diffraction geometry

When a high power laser is incident on a material, as is the case in this experiment, x-rays are produced. The more powerful the initial laser pulse, the more photons are produced, and the more energetic are the x-rays. This effect is exploited when producing a laser x-ray source; however, this effect is also in play when seeding a shock wave in the sample. The x-rays produced from the target are a nuisance in this experiment since they will appear on any x-ray detectors as "drive noise". Some careful geometric positioning can be implemented to reduce the impact of drive noise.

The surface at which the laser-sample interaction occurs is usually referred to as the front surface; the opposing surface of the sample is termed the rear surface.

When diffracting from the sample, diffraction can be detected in transmission, or in reflection. In a transmission geometry, the diffracted x-rays are detected on the opposite side of the sample relative to the initial x-ray beam. The diffracted x-rays must traverse the full width of the sample, causing attenuation of the final detected intensity. In a reflection geometry, the diffraction is detected from the same surface at which the initial x-ray beam is incident. A reflection geometry from the rear surface has the advantage of using the sample itself to filter out the majority of the drive noise. This method, however, requires more careful timing of the x-ray pulse to ensure coincidence of the x-rays with the passage of the shock wave. The x-ray diffraction pattern will inevitably contain diffraction from both the shocked material, and the unshocked material.

A reflection geometry from the rear surface of the sample was selected for this experiment since the preservation of diffraction intensity is of utmost importance.

X-ray source selection

Recall from the Bragg condition $\mathbf{G} \propto \frac{sin(\theta_B)}{\lambda}$. A short x-ray wavelength results in the presence of higher order reflections at lower Bragg angles. similar to the argument made for a large lattice parameter, a short wavelength has the effect of increasing the amount of reciprocal space accessed; the total number of diffraction rings that are observed will increase. The more rings are accessed, the more data points can be used to measure temperature.

4.2 Niobium: the sample of choice

Niobium was chosen as a good candidate material, as it possesses a favourable combination of the qualities described in section 4.1. Nb is a BCC material with a lattice parameter of 3.3004 Å[81]. Nb also has a low Debye temperature of 260 K at room temperature.

The experimental Hugoniot of niobium up to 200 GPa (2 Mbar) is shown in figure 4.1. Phase transitions are typically evidenced by a sudden change of relationship between pressure and particle velocity; this is due to the volume collapse associated with plastic phase transitions. The absence of such a change in figure 4.1 indicates the absence of a phase transition in Nb under shock loading.
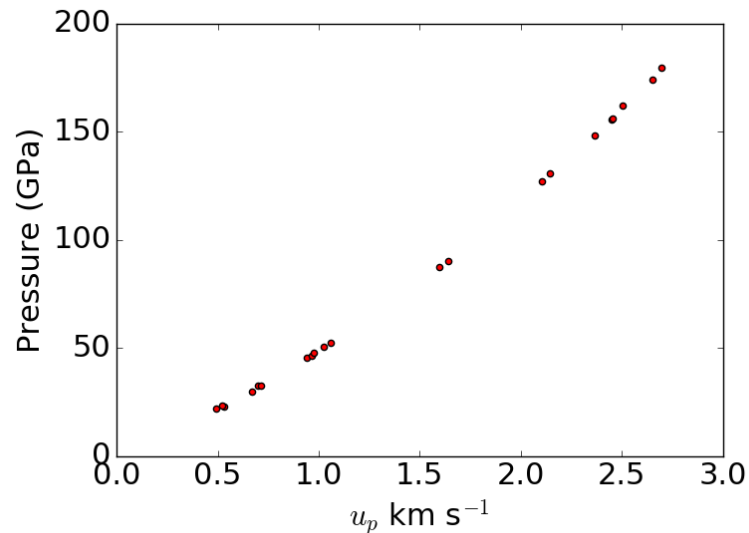
Figure 4.1: *Some experimental Hugoniot data for niobium is shown [97] [98]. The lack of "kinks" in the Hugoniot indicates an absence of phase transitions.*

105

4.3 Experimental Setup

The Orion Laser Facility was chosen to platform this experiment. Orion has a track record of delivering high quality diffraction data on similar shock experiments [60, 99].

The laser facility itself consists of ten long pulse beams nominally capable of delivering 500 J per beam to a target for a duration of 0.1 - 10 ns [100, 101]. The light is generated from a commercial laser source at 1053.0 nm, shaped to user specification, amplified to high energy, frequency tripled to 351 nm, and finally focused onto target. For this experiment, facility restrictions meant that the laser was capable of delivering approximately 260 J per beam with a pulse duration of 0.5 - 5 ns. Five backlighter beams were used to generate x-rays, while one drive beam was used to shock the sample. Both the drive beams and backlighter beams were fitted with phase plates; phase plates introduce decoherence to the optical front of the laser, producing a more spatially uniform drive spot [102].

For x-ray generation, the shortest possible pulse length is desirable to give a diffraction pattern from a single point in time. X-rays for this experiment were generated by striking a 10 μm metal foil with a 0.5 ps pulse, with a spot size of 250 μm. The heating of the target produces a population of He-like ions [103]. The de-excitation of core shell electrons results in the emission of high energy x-rays; such emission is termed He-α. The energies of the resulting x-rays are material dependent. The primary backlighter material used on this experiment was Zn, with peak x-ray energy at 8.997 keV [103], though Fe and Cu were also used.

The laser generated He-α x-ray sources used on this experiment are not perfectly

106

monochromatic, and the additional wavelengths also diffract from the sample, showing up as noise on the image plates. On Orion, the shortest laser pulse available was 0.5 ns. The pulse-length of the x-ray beam is typically commensurate with the laser pulse [104], and so the pulse-length of the x-ray source is also assumed to be 0.5 ns.

The drive beam should use as long a pulse length as possible, since premature extinction of the drive beam will result in a release wave travelling inwards from the drive surface; the release wave will rapidly catch up with the shocked material and may disrupt the shocked state that is being investigated, potentially destroying any attempts at sensible temperature measurement. Since the pressure in the sample is related to laser intensity approximately by $P \propto I^{2/3}$ [105], the laser intensity can be used to control pressure. To alter intensity one may alter the energy, duration, or spot size of the beam.

The Orion facility is fitted with many optical diagnostics [106]. The primary diagnostic in this experiment is the BBXRD (broad band x-ray diffraction) detector, which is ideally suited for this experiment; it has been fielded previously on similar experiments requiring large area coverage of diffraction [60, 99]. The BBXRD acts as an x-ray cage, surrounding the material with four image plates in a pyramid fashion. A cross-section schematic of the BBXRD is shown in figure 4.2. The image plates used are Fuji BAS-SR, a popular choice of detector on laser-shock experiments [107]. The image plates are shielded using two filter materials. The first filter material is Al with thickness of 10 μm. This filter is opaque to low energy x-rays, as indicated by figure 4.3. This is desirable as it has the effect of attenuating low-energy photons that contribute to noise, while leaving high-energy signal largely unchanged. Al is also very cheap and malleable; this allowed complete wrapping of the image-plate

with the Al filter, preventing low energy x-rays from interacting with the detector through the edges. This advantage was not available on the second high-energy filter materials.

The second filter material is selected so that an absorption edge in the filter occurs at an energy slightly above the energy of the main diffraction signal. The absorption edges for Fe, Cu, and Zn are shown in figure 4.3. These edges have the effect of filtering out high-energy noise at energies above the signal energy, while still allowing the signal itself to get through to the detector largely unhindered. In the case of an Fe x-ray source, a filter of Fe with thickness 10 μm was used. In the case of a Cu x-ray source, a filter of Cu with thickness 10 μm was used; occasionally a 20 μm Cu foil was used in an attempt to reduce noise further. In the case of a Zn x-ray source, a filter of Zn with thickness 10 μm was used.

The BBXRD is the primary diagnostic for this experiment. There are three secondary diagnostics: VISAR (velocity interferometry system for any reflector), GXD (gated x-ray detector), and HEX-ID (high-energy x-ray spectrometer).

VISAR uses interferometry to measure the rear surface velocity of the sample as the shock reaches the rear of the sample [20]. In figure 4.2, a low power continuous wave laser is incident on the rear surface of the sample via a mirror. After reflection from the sample, light travels back through the BBXRD, through the mirror, and back into the VISAR diagnostic. The returning beam is split in two; one half of the beam is time-delayed using an optical cavity, while the other half is unhindered. The two beams are recombined and their interference pattern is recorded over a time window coinciding with the arrival of the shock wave at the rear surface. The rear surface accelerates, causing the interference fringes to "shift". By measuring the
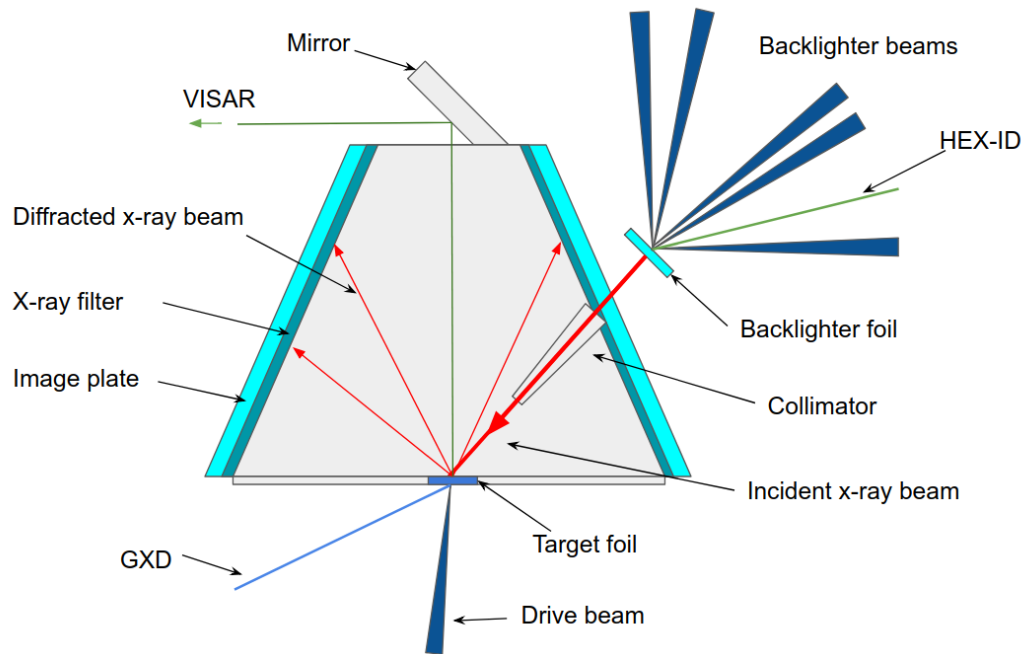
Figure 4.2: *A schematic cross-section of the BBXRD (broad band x-ray diffraction) detector, not to scale. The sample (target foil) to be probed sits at the largest surface of the detector. The drive beam is incident upon the surface of the sample on the exterior of BBXRD. Simultaneously, the backlighter foil is illuminated with the backlighter beams. This creates a bright x-ray source. A sliver of these x-rays are allowed into the BBXRD via the collimator where they interact with the target rear surface. The rays are diffracted away from the sample and onto the image plates, which sit on all four sides of the the interior of BBXRD. X-ray filters are placed in front of the image plates to attenuate the signal from low-energy background x-rays. After each shot is completed, BBXRD is taken apart and the image plates scanned.*

shift of fringes before and after the shock, the velocity of the sample rear surface is measured. The measured free surface velocity is often assumed to be related to the particle velocity by $v_{fs} = 2v_p$, and so the Hugoniot relations can be used to link rear-surface velocity to pressure within the sample. In this experiment, however, the main use of VISAR was to time the shock wave, since the fringe shift coincides with the arrival of the shock wave at the rear surface; this requires a reference

Attenuation length of Al, Fe, Cu, and Zn as a function of photon energy
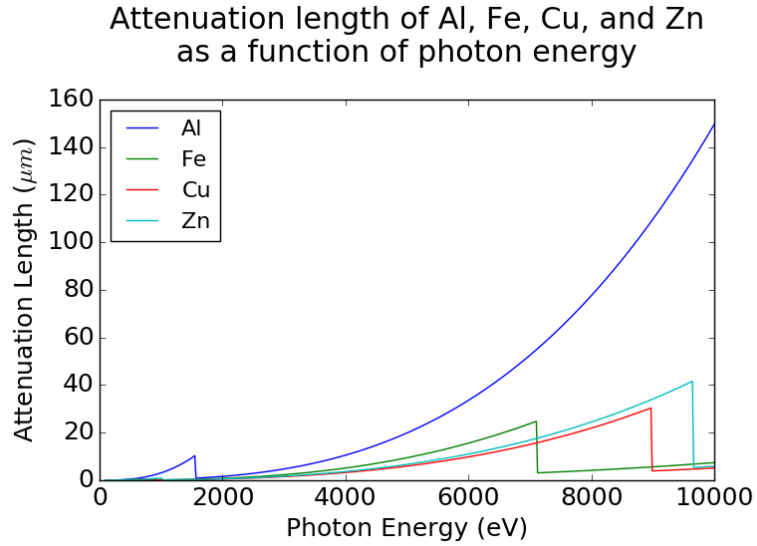
Figure 4.3: *The absorption spectrum of Al, Fe, Cu, and Zn as a function of photon energy. The presented data was generated using the online CXRO tool [108], using semi-empirical atomic scattering factors developed by Henke et. al. [109].*

VISAR measurement to be taken with a very thin sample so that the start time can be recorded. Using this timing method, x-ray diffraction could be timed to occur just before the shock front reached the rear surface. VISAR also provides spatial information about the planarity of the shock front; if the shock front is planar, the fringe shift will occur at the same time across the spatial dimension of the VISAR output.

GXD is used to image time-resolved x-ray intensities at extremely high frame-rates [110]. In this experiment the GXD is trained on the target front surface. When the drive beam strikes the target, x-rays are emitted. The image left on the GXD by the x-ray emission gives insight into the quality of the drive beam profile. Ideally the emission spot is supergaussian in form, with a clear central uniform region.

If the emission spot is irregular in shape, with multiple hot and cold regions, the implication is that the laser intensity differs across the surface of the sample. Since differing intensities result in differing material pressures, the seeded shock wave will be non-uniform, and the final state of the shocked material difficult to assess. Unfortunately, the GXD was not functional during the main portion of the experiment and no images were taken.

HEX-ID measures a time-integrated spectrum of x-ray emission [111]. The energy spectrum is generated by diffraction from crystals onto image plates. Since the diffraction angle is a function of x-ray energy, the position of diffraction lines on the image plate will correspond to energy. HEX-ID has four channels with a different crystal in each channel; this allows for a broad range of x-ray energies to be collected. The HEX-ID is pointed at the backlighter foil so that the x-ray emission spectrum from the backlighter can be observed. It is common on laser-shock experiments involving x-ray diffraction to have uncertainty related to the performance of the x-ray backlighter. By fielding HEX-ID, any speculation on x-ray performance can be substantiated or dismissed.

4.3.1   X-ray source configuration

Typically, He-α x-rays are generated by striking the foil with a single laser pulse. Other x-ray generating procedures have been explored [112]. By striking the metal foil with two pulses separated by a few ns, it has been observed that the x-ray yield of the second pulse increases above that observed by a single pulse x-ray source [113]. The idea is conceived by the observation that gaseous x-ray sources convert laser energy to x-rays more efficiently than thin metallic foils. This is due to the formation

of an underdense plasma in the case of a gaseous target. In the case of a metallic foil, the metal is pre-exploded with the intention of forming an underdense plasma region around the laser spot. The subsequent heating of the underdense plasma has been shown to produce yields 2-4 times that observed for a single pulse, though this was observed on the OMEGA laser, where the metallic foil is irradiated on both sides [113]; the available intensities are also higher at OMEGA than at Orion.

With a Zn x-ray source it should be possible to see up to the (3 3 2) diffraction ring in Nb, though the maximum driven diffraction visible will be from the (4 2 0) ring. Figure 4.4 shows an example Zn x-ray spectrum collected on the experiment. As previously mentioned, the HEX-ID spectrometer used has 4 channels, with each channel coloured separately in the figure. Each channel contains a crystal of differing reflectivity. The reflectivities of these crystals were not well known at the time of writing, which results in some error in the intensities. This error results in a mis-match between the intensities of each channel; this error is in the region of 30 - 50% [114]. The low energy x-rays are thought to be due to drive noise on the front surface of the Nb sample, though this is difficult to confirm.

A high x-ray yield is desirable for this experiment. A double pulse configuration was therefore implemented, with an idealised pulse shape given in figure 4.5. A side-effect of this configuration is that the image plates will be exposed to two diffraction images from different moments in time. The first x-ray pulse will interact with the sample before the shock has travelled very far into the sample. The second pulse is timed such that the shock wave has traversed most of the sample width. The resulting x-ray diffraction pattern on the detectors will have a very strong signal from the static material, overlayed with signal from the driven material.
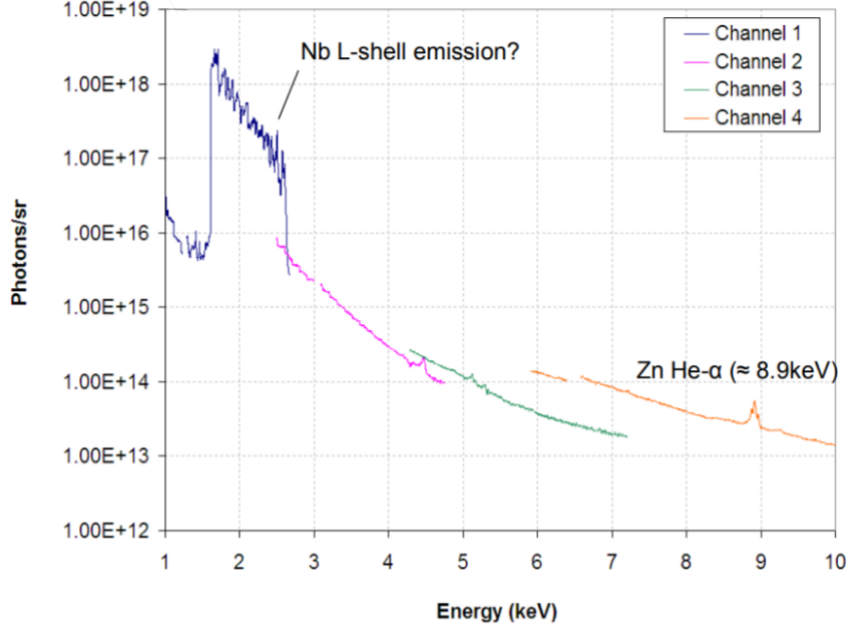
Figure 4.4: *A sample Zn x-ray source used on this experiment. The He-α signal is clearly discernible between 8.9 - 9 keV. The large volume of low energy x-rays are thought to be the result of drive noise from the Nb front surface.*

For a Zn x-ray source (8.997 keV) the linear attenuation depth of niobium is 11.2 μm. This is just enough to allow the sampling of a substantial region of the driven sample; however, it means that the timing of the experiment will have to be somewhat exact. If the timing is too early, no diffraction from the driven portion of the sample will be observed since the x-rays are unable to penetrate far enough into the sample. If the timing is too late the material will be driven, but the shock will have broken out through the rear surface, disrupting the Hugoniot state that is being probed. For Cu x-rays (8.9 keV), the attenuation length of Nb is 10.9 μm, and for Fe x-rays (6.7 keV) the attenuation length of Nb is 5 μm.
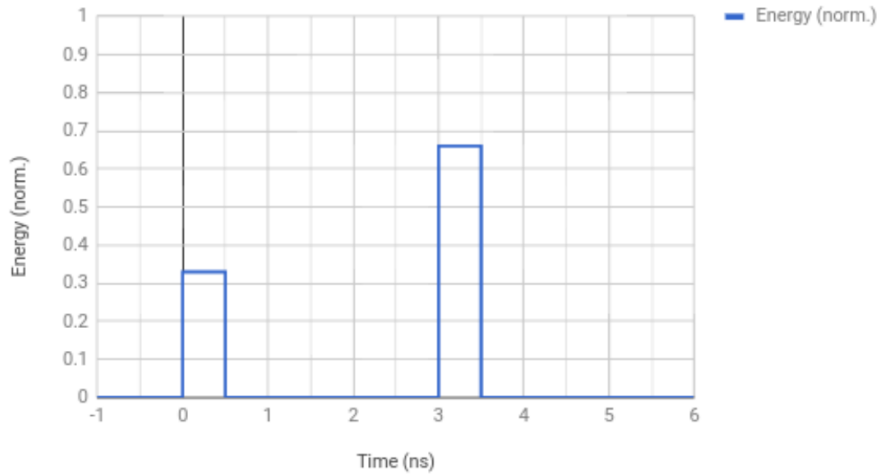
Figure 4.5: *An ideal version of the double laser pulse used on Orion. The first pulse is followed by a second pulse with a 3 ns peak to peak delay. The ratio of pulse energy is 1:2, and the width of each pulse is 0.5 ns.*

4.4 Simulated sample conditions

To understand the conditions present in the sample, some simulations were carried out by David McGonegle using the HYADES plasma hydrodynamics code [115]. This code is a widely used tool for simulating the sample conditions present in a sample under laser shock compression.

The input parameters required to simulate Nb were not readily available, however the input parameters for Cu were available. As can be seen in figure 4.6, Cu responds to shock compression in a way that is very similar to Nb; similar pressures and shock velocities are achieved for the relevant particle velocities. Therefore, Cu is used here as an approximation of Nb; note that while this difference in material precludes an exact comparison with experiment, there are some qualitative insights that can be drawn from such an exercise.
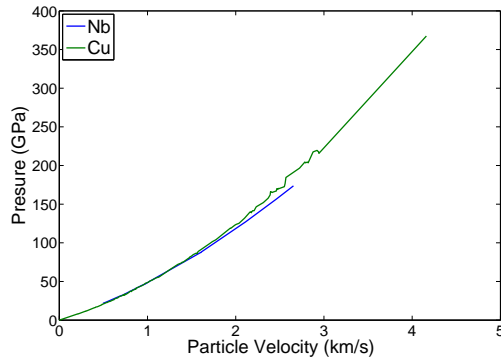
Pressure vs particle velocity   Shock velocity vs. particle velocity
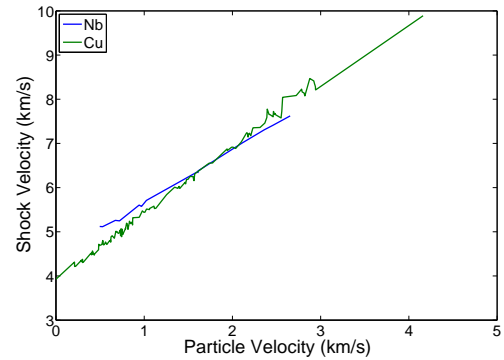
Figure 4.6: *A comparison of the pressure and shock velocity of Nb and Cu for a range of particle velocities relevant to the present experiment [98]. The two materials exhibit similar behaviour under the shock conditions considered here. These figures were created by David McGonegle and are reproduced here with permission.*

Figures 4.7 and 4.8 show two HYADES simulations performed on Cu. The two simulations reach a sample pressure of approximately 20 GPa and 110 GPa respectively. The y-axis shows the depth of the sample, and the x-axis shows the elapsed time in ns. The simulated target is composed of 15 μm of parylene (at the bottom of the image), and 10 μm of Cu (at the top of the image). The two layers of material are separated visually by a bright line at 15 μm. As the shock progresses, more material is compressed. The colour shows the pressure at each point in the 1D sample at every moment in time. When the shock reaches the material at 25 μm, the shock has travelled through the full length of the sample.

In both the 20 GPa sample and the 110 GPa there is a slight variation of pressure in the bulk of the Cu. If this were present on experiment, one might expect some broadening in the detected x-ray diffraction signal.
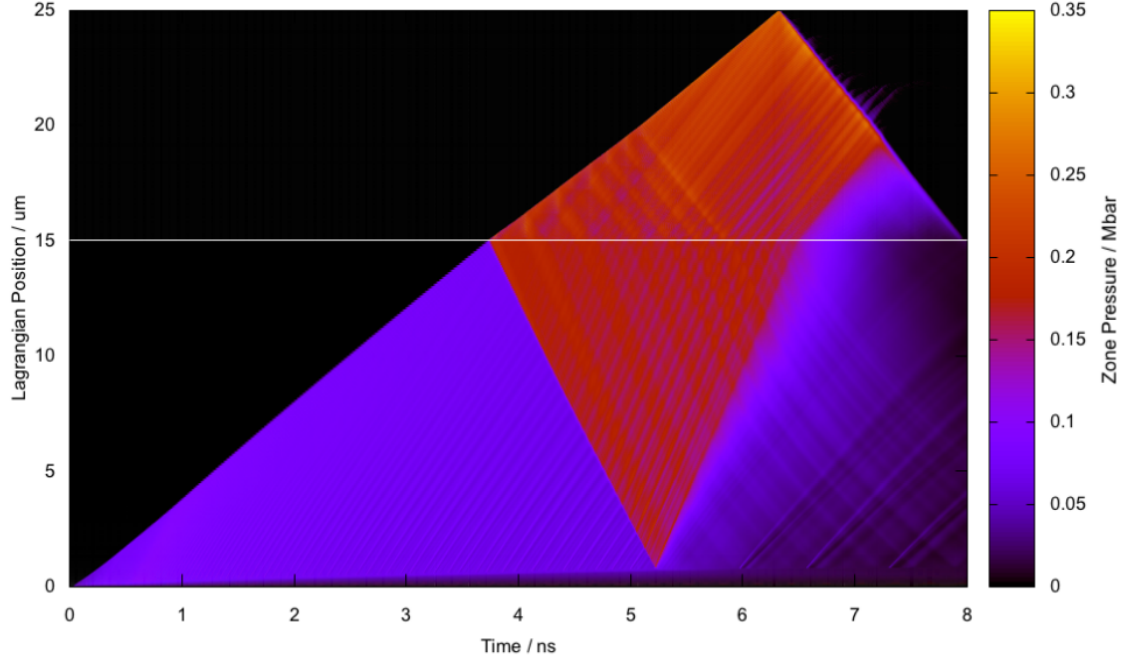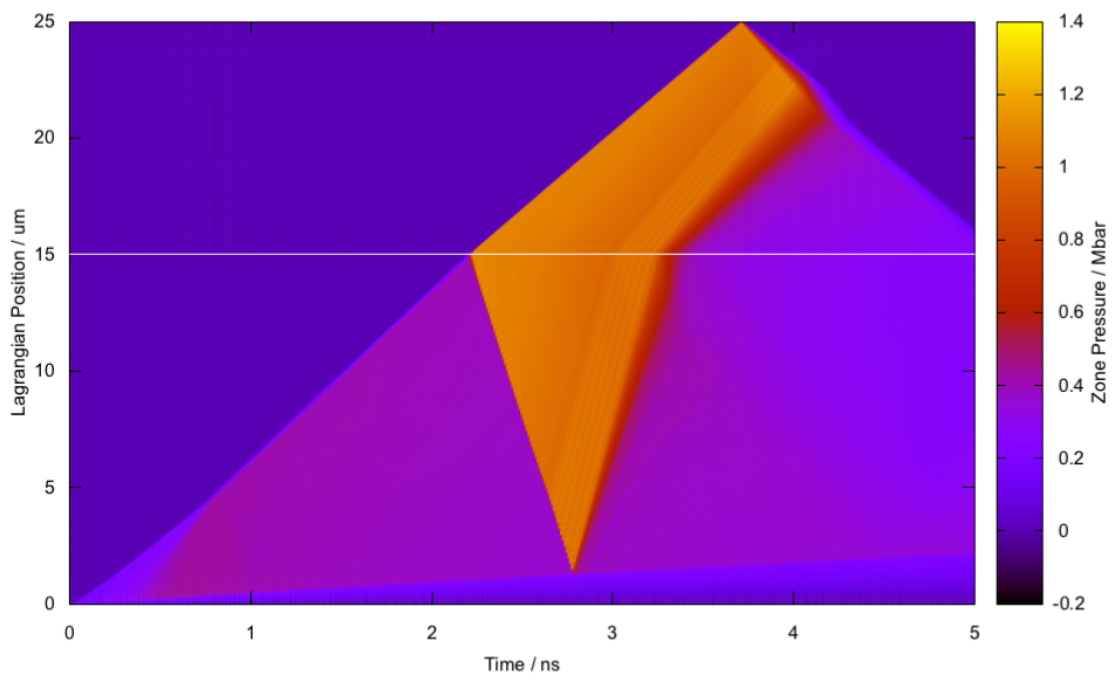
Figure 4.7: *A HYADES simulation of Cu at ≈ 20 GPa (0.2 Mbar). This simulation was produced by David McGonegle and is reproduced here with permission.*

4.5 Overview of results

More than 50 shots were completed over the course of the experiment. Appendix C summarises the 42 shots that produced high quality diffraction data. The remaining shots were discounted due to equipment malfunction or improper diagnostic operation. The pressures were calculated by measuring the shift in diffraction peak positions, assuming that the compression is hydrostatic, and then using the Nb Hugoniot shown in figure 4.1 to link compression to pressure. This assumption of hydrostatic compression is supported by the apparent lack of strength in the diffraction images; if this assumption were not valid, one would expect to see a variation in θ_B around the diffraction ring [60, 61, 116].

Figure 4.8: *A HYADES simulation of Cu at ≈ 110 GPa (1.1 Mbar). This simulation was produced by David McGonegle and is reproduced here with permission.*

4.6   Diffraction Image Analysis

To illustrate the image analysis, diffraction data captured using BBXRD on shot 10268 will be used. Shot 10268 performed diffraction on a static sample of niobium; the drive beam was delayed so that the x-ray diffraction would image the static crystal only. The x-rays are no longer incident on the sample when the drive-beam strikes the target. The drive noise is therefore captured on the image plates alongside the static signal. The backlighter used here was Zn with the double pulse shape of figure 4.5. This is an important shot as it will serve as a temperature reference at $T = 300$ K. Because of the lack of shocked material signal, it is also one of the easiest shots to analyse.

4.6.1 Converting raw image grayscale to PSL

The raw images are in the form of .img files. This is a file format created by the Fujifilm FLA 7000 flatbed image plate scanner used in this experiment. This file format saves the intensity in a logarithmic grayscale format. To convert to the linear PSL units (photostimulated luminescence) one must use the equation

$$PSL = \left(\frac{R}{100}\right)^2 \frac{4000}{S} 10^{L[G/(2^b-1)-0.5]} \tag{4.1}$$

where R is the resolution of the scanner in μm, S is the scanner sensitivity setting, L is the latitude (the order of magnitude of the dynamic range) , b is the number of bits used to store a data point, and G is the raw image pixel intensity [117]. All images were scanned using values of $R = 50 \ \mu$m, $S = 4000$, $L = 5$, and $b = 16$ bits. PSL is proportional to x-ray intensity until saturation [118], and so it is sufficient to use PSL as a proxy for intensity for the purposes of this analysis.

Images of the four BBXRD image plates are shown in figure 4.9, converted to PSL. Structure within the x-ray source spectrum is clearly visible in the diffraction images.

There are some bright features on the edges of these image plates due to slight misalignment between the filters and image plates. These features must be masked from further analysis. This is done by simply setting pixels in these regions to zero intensity.

(a) Plate 1

(b) Plate 2

(c) Plate 3

(d) Plate 4
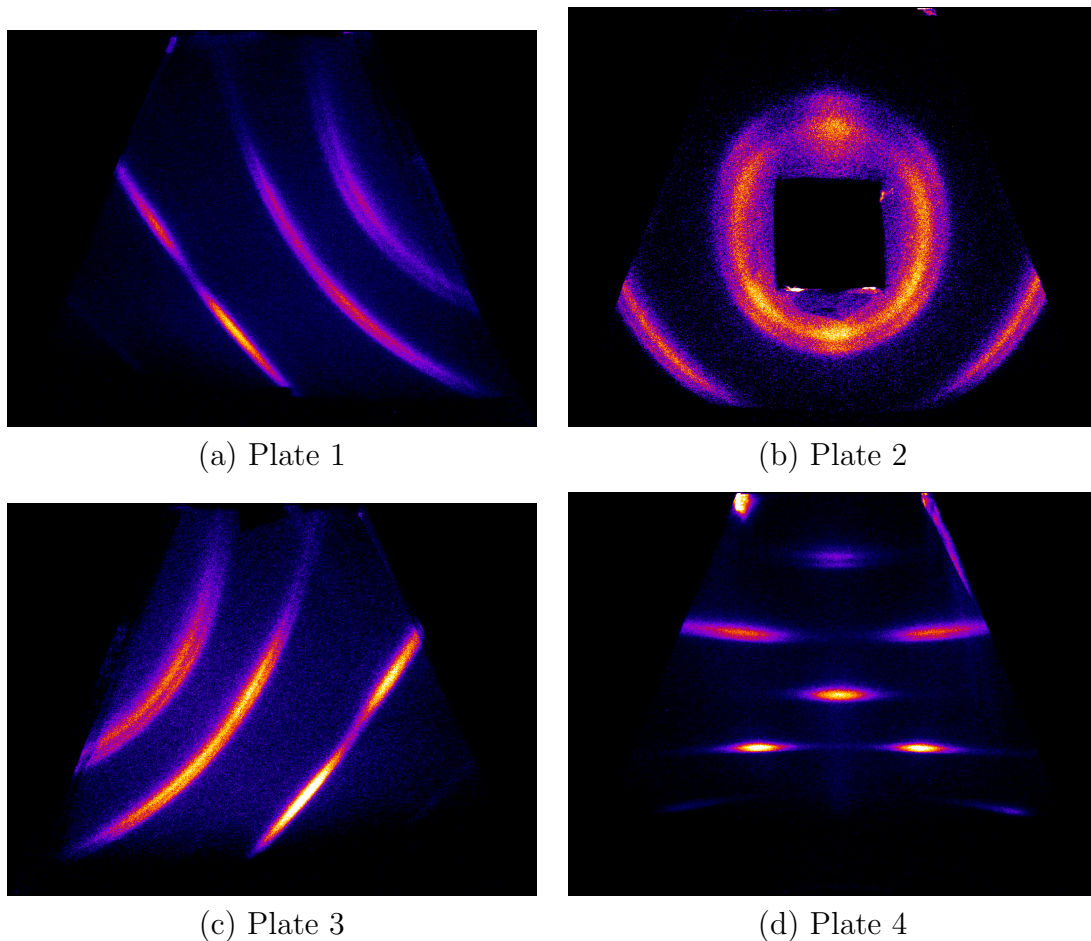
Figure 4.9: *The four image plates from shot 10268, showing only diffraction from the unshocked niobium.*

4.6.2 Beginning the image transformation

Now that the images are in appropriate units, the images are transformed so that the intensity of a full diffraction ring can be calculated. This is done by replotting each pixel from each image plate onto a 2D histogram where one dimension is $|\mathbf{G}^2|$ (or equivalently θ_B) and the other dimension is the angle around the diffraction ring, ϕ.

To begin, the images are aligned using the LP-Diffract code developed by Andrew Higginbotham. This code simulates the positions of diffraction cones for any given experimental geometry. Using LP-Diffract, the diffraction lines on the image plates are aligned with the ideal diffraction positions, and so the exact geometric position of the image plates relative to the sample is recovered.

A code, theta.py, was written to calculate $|\mathbf{G}^2|$ at every pixel using the Bragg equation, and ϕ at every pixel by defining an arbitrary plane where $\phi = 0$. Maps showing the values of $|\mathbf{G}^2|$ at each pixel for each image plate are shown in figure 4.10. Maps showing the values of ϕ at each pixel for each image plate are shown in figure 4.11.

Once $|\mathbf{G}^2|$ and ϕ are defined for every pixel, the pixels are binned to produce an intensity histogram, showing intensity vs. $|\mathbf{G}^2|$. The histogram is then used to make an image. Before the transformed image is created, however, the pixel intensities are corrected.
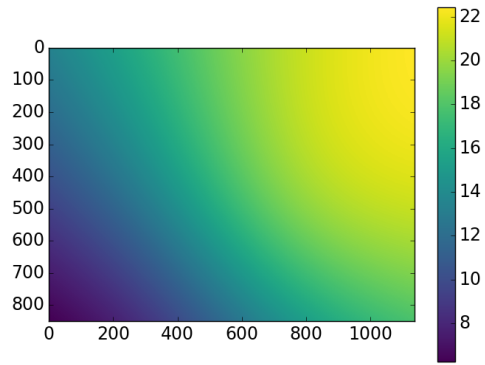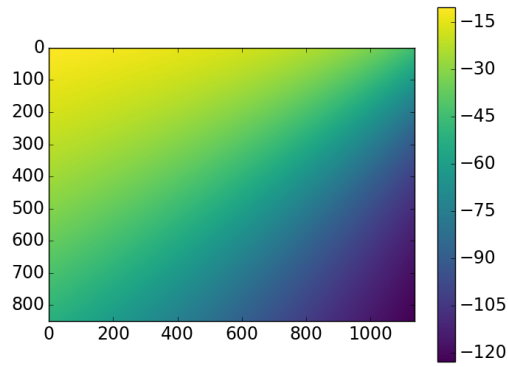
(a) Plate 1
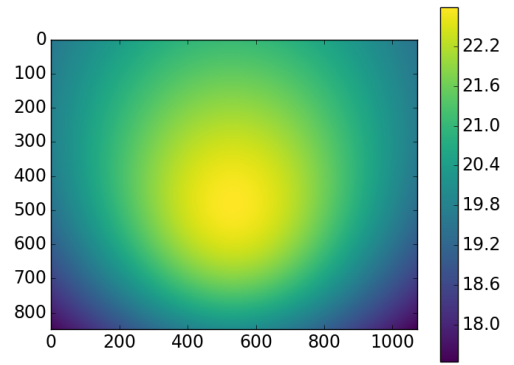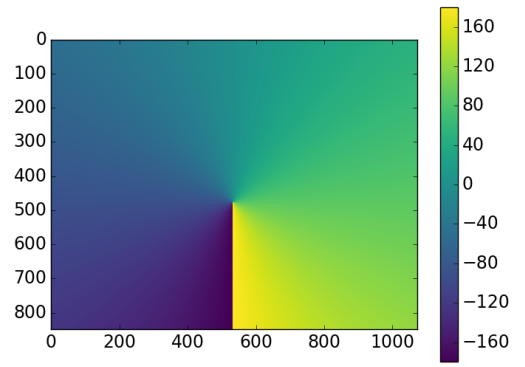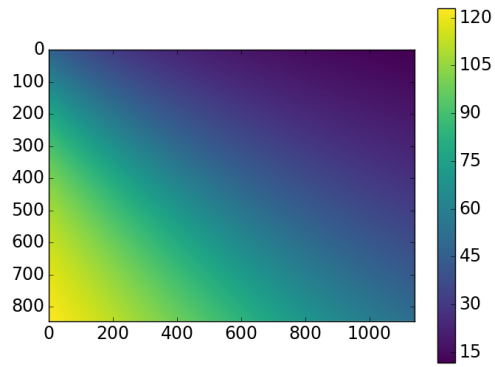

(b) Plate 2
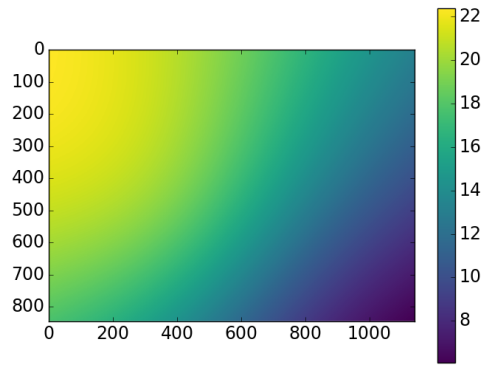
(c) Plate 3
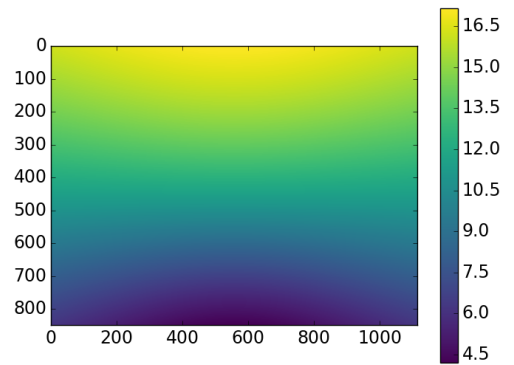
(d) Plate 4

Figure 4.10: *Maps of the $|\boldsymbol{G}^2|$ values calculated for every pixel in every image plate of shot 10268. The x and y axes correspond to pixel number. The colourbar to the right of each image indicates the $|\boldsymbol{G}^2|$ for each colour in the image.*
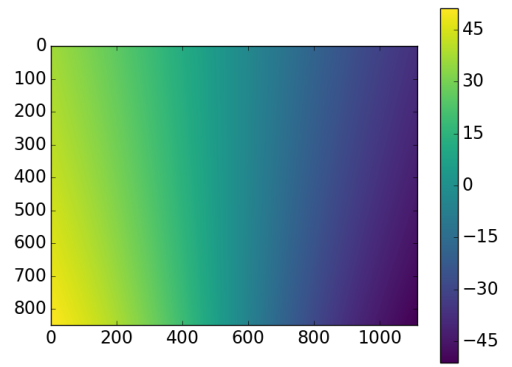
(a) Plate 1

(b) Plate 2

(c) Plate 3

(d) Plate 4

Figure 4.11: *Maps of the φ values calculated for every pixel in every image plate of shot 10268. The x and y axes correspond to pixel number. The colourbar to the right of each image indicates the φ for each colour in the image.*

4.6.3 Intensity corrections

This analysis does not require absolute intensities to be calculated; however, there is a need to establish relative intensities accurately. A number of corrections require application to the images. These are: the Lorentz-polarisation correction; the correction due to attenuation by the sample; the correction due to the x-ray filters; the correction due to the atomic form factor. Each of these corrections are discussed below.

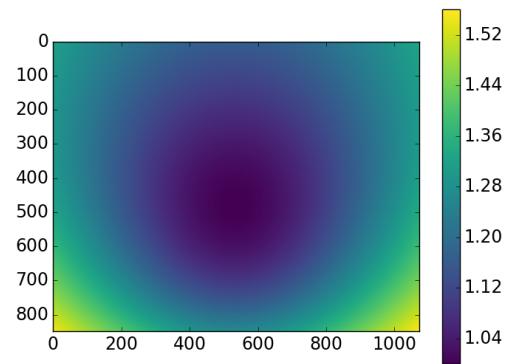**The Lorentz-polarisation correction**

The Lorentz-polarisation correction was discussed in section 2.3.3. The geometrical part of the Lorentz-polarisation factor, shown in equation 2.43 arising from the intersection of the finite-width Ewald sphere with the finite-width reciprocal lattice is accounted for later in the analysis in section 4.6.7 when correcting for crystallographic texture. Therefore the Lorentz-polarisation correction, now reduced simply to a polarisation correction, is applied to each pixel.

$$C_{LP} = \frac{2}{1 + cos^2(2\theta_B)} \tag{4.2}$$

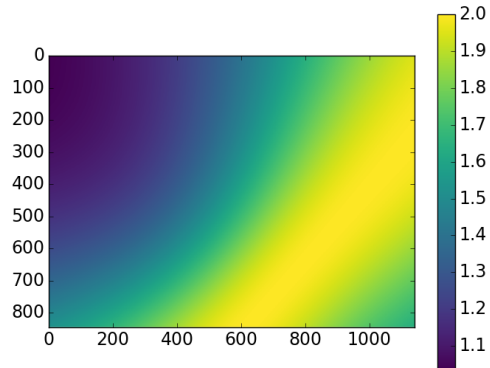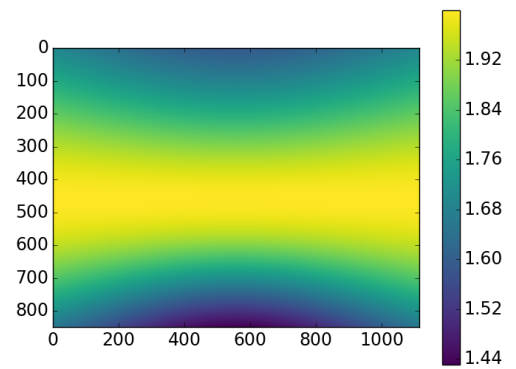The corrections applied to each image plate is shown in figure 4.12.
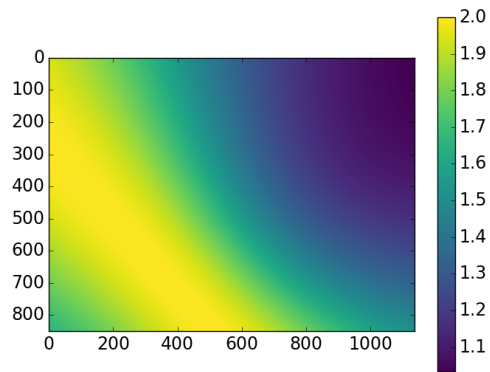
(a) Plate 1

(b) Plate 2

(c) Plate 3

(d) Plate 4

Figure 4.12: *The correction factors due to Lorentz-polarisation for application to the four image plates from shot 10268. The x and y axes correspond to pixel number. The colourbar to the right of each image indicates the correction factor for each colour in the image.*

Attenuation by the sample

When x-rays diffract from a sample the incident beam must enter the sample, scatter from the material, and then exit the sample. Since there is some absorption of the beam as it travels through the sample, the intensity is decreased. Furthermore, the path length of the x-ray beam is different for each corresponding point on the detector surface. A schematic of the situation is shown in figure 4.13. The image shows two beams being diffracted from within a sample onto a pixel at point D. The total distance travelled within the sample is $x + y$, and this distance differs from one diffracted beam to the next. As each beam is attenuated as a function of path length, the correction to the intensity detected at D is a non-trivial calculation.
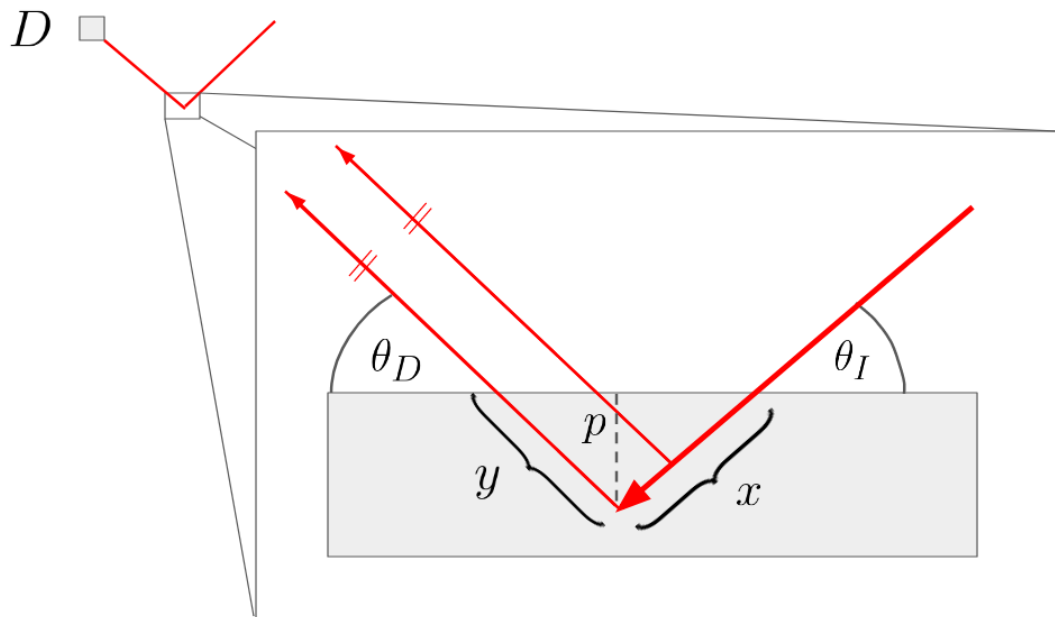

Figure 4.13: *The path of a diffracted x-ray from source to the pixel at position D. The path travelled by beams diffracting from different points is attenuated by a different amount, depending on the amount of sample traversed by each beam.*

The attenuation due to absorption by the sample follows the Beer-Lambert law. Thus the intensity at the point of detection I_D due to a given point in the sample is given by

$$I_D = I_S e^{-\mu x} \alpha e^{-\mu y} \tag{4.3}$$

where I_S is the intensity of the x-ray source, μ is the attenuation coefficient of the sample, x is the path length of the incident beam into the sample, α is the scattering probability at each point in the sample, and y is the path length of the diffracted beam out of the sample.

It is prudent to substitute for the perpendicular penetration into the sample p. This substitution takes the form

$$x = \frac{p}{sin\theta_I} \tag{4.4}$$

$$y = \frac{p}{sin\theta_D} \tag{4.5}$$

where θ_I is the angle of incidence and θ_D is the angle of diffraction. Both angles are defined visually in figure 4.13. Thus

$$I_D = I_S e^{-\mu \frac{p}{sin\theta_I}} \alpha e^{-\mu \frac{p}{sin\theta_D}} \tag{4.6}$$

Combining the exponents gives

$$I_D = I_S \alpha e^{-\mu p (\frac{1}{sin\theta_I} + \frac{1}{sin\theta_D})} \tag{4.7}$$

The equation is plotted in figure 4.14, showing I_D vs. p for different values of θ_I, holding θ_D constant. The total intensity detected at D is given by the area under each curve. Integrating between 0 and infinity gives
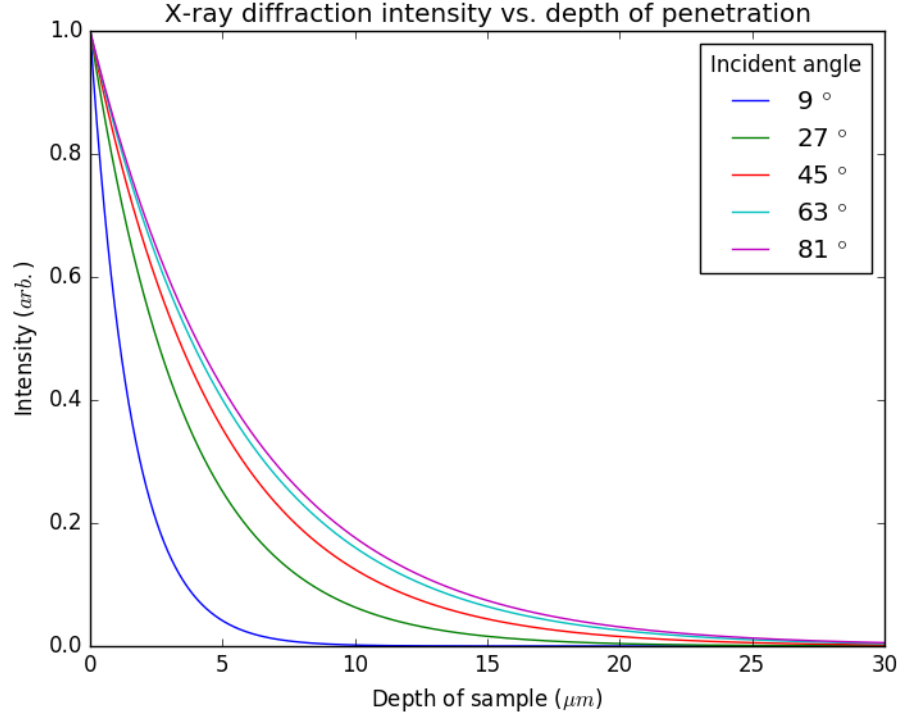

Figure 4.14: *The intensity of diffraction as a function of penetration depth p, for a given point of detection with diffraction angle $\theta_D = 45°$, and a sample with attenuation coefficient $\mu = 0.0862 \ \mu m$. The different colour curves represent different values of θ_I. The area under each curve represents the total intensity detected at point D.*

$$I_D = I_S \alpha \int_0^\infty e^{-\mu p(\frac{1}{sin\theta_I} + \frac{1}{sin\theta_D})} dp \tag{4.8}$$

Using the identity $\int_0^\infty e^{-ax} dx = \frac{1}{a}$ the result is

127

$$I_D = I_S \alpha \frac{1}{\mu(\frac{1}{sin\theta_I} + \frac{1}{sin\theta_D})} \tag{4.9}$$

This equation tells us the total intensity of diffraction at the point of detection D due to all possible scattering sites in the probed medium.

The correction factor to be applied to each pixel intensity is

$$C_S = \left(\frac{1}{sin\theta_I} + \frac{1}{sin\theta_D} \right) \tag{4.10}$$

The values of C_s applied to each image are shown in 4.15.

Note that this treatment assumes that the incident beam is not attenuated by the diffraction of x-rays. While this is technically incorrect, the fraction of the incident beam that is scattered is often considered to be negligible given the fact that about 0.1% of the total incident beam is diffracted.

In this experiment the diffraction will often be coming from both shocked material as well as static material, and so in this case there will be two separate attenuation lengths in play. This effect has been neglected given the small difference in attenuation lengths between shocked and unshocked material of the same element.

It is also assumed in this analysis that, for every pixel at detection point D, the angle of diffraction θ_D is constant at every point within the sample. This is justified since the distance from sample to image plate is several mm, whereas the probed sample thickness is of the order of 10 μm, and so the beams are very close to parallel when arriving at any point D.
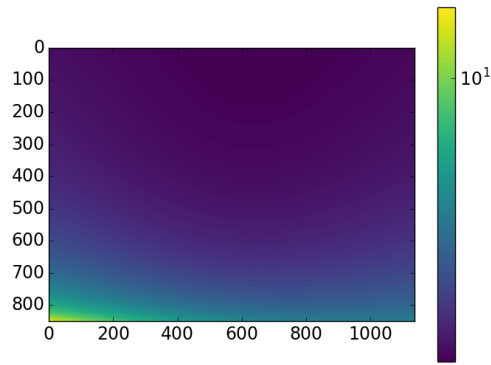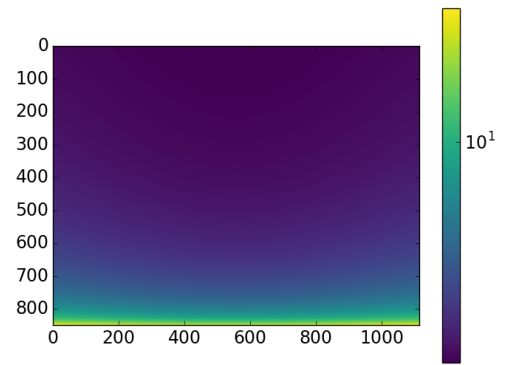
(a) Plate 1
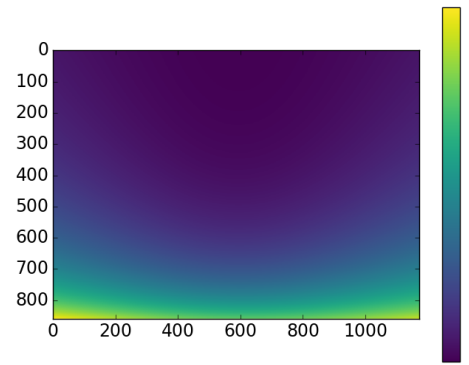
(b) Plate 2
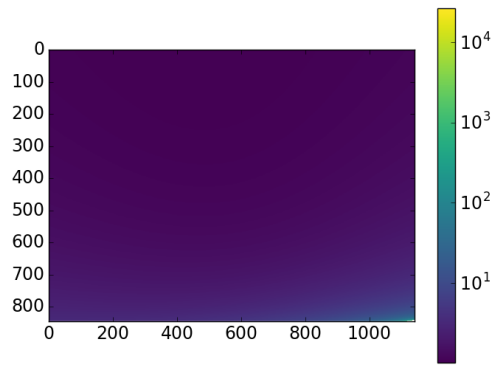
(c) Plate 3

(d) Plate 4

Figure 4.15: *The correction factors due to sample attenuation for application to the four image plates from shot 10268. The x and y axes correspond to pixel number. The colourbar to the right of each image indicates the correction factor for each colour in the image.*

Attenuation by filters

As previously mentioned, thin sheets of metal are placed in front of the image plates to filter out low energy background x-rays. The signal x-rays also must travel through these filters. Since the diffracted rays pass through the filters at different angles, the effective path-length through the filters is different at every point on the image plate.

The effective filter thickness t_e for a filter of thickness t is

$$t_e = \frac{t}{cos(\alpha)} \tag{4.11}$$

where α is the acute angle between the normal of the filter and the diffracted beam. Using the Beer-Lambert law, the attenuation of the beam intensity is given by
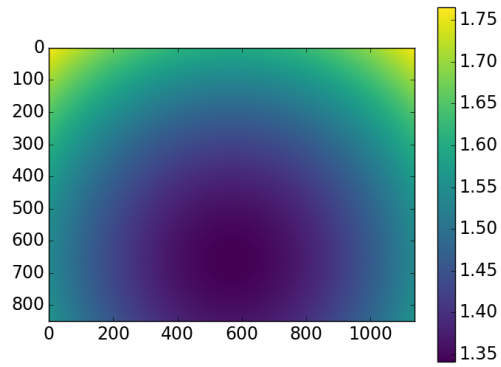
$$I_D = I_S e^{\frac{-t_e}{\xi}} \tag{4.12}$$

where ξ is the attenuation length of x-rays travelling through the filter.

The correction factor for filter attenuation, then, is

$$C_F = \frac{1}{e^{-t_e/\xi}} \tag{4.13}$$

The correction factors applied to each image plate from shot 10268 are shown in figure 4.16.

(a) Plate 1
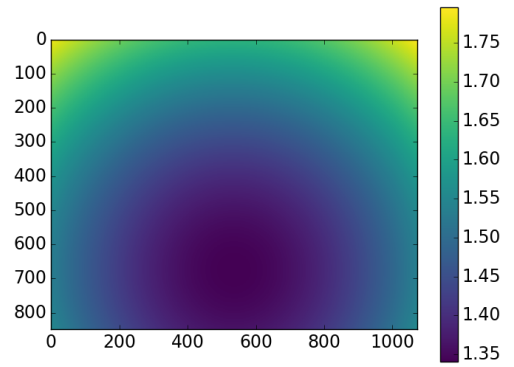
(b) Plate 2
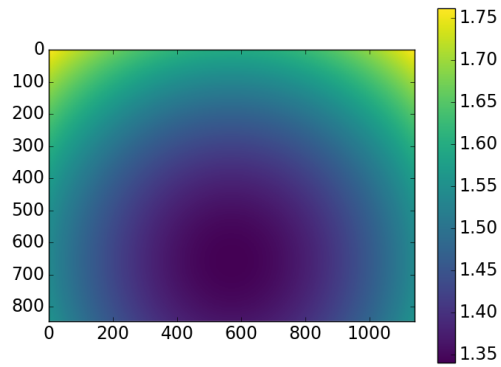
(c) Plate 3

(d) Plate 4

Figure 4.16: *The correction factors due to filter attenuation for application to the four image plates from shot 10268. The x and y axes correspond to pixel number. The colourbar to the right of each image indicates the correction factor for each colour in the image.*

Atomic form factor correction

The atomic form factor accounts for the dependence of scattering intensity due to differences in atomic structure. Each element has its own atomic form factor; Niobium's atomic form factor is shown in figure 4.17, where $|\mathbf{G}| = \frac{sin(\theta)}{\lambda}$.
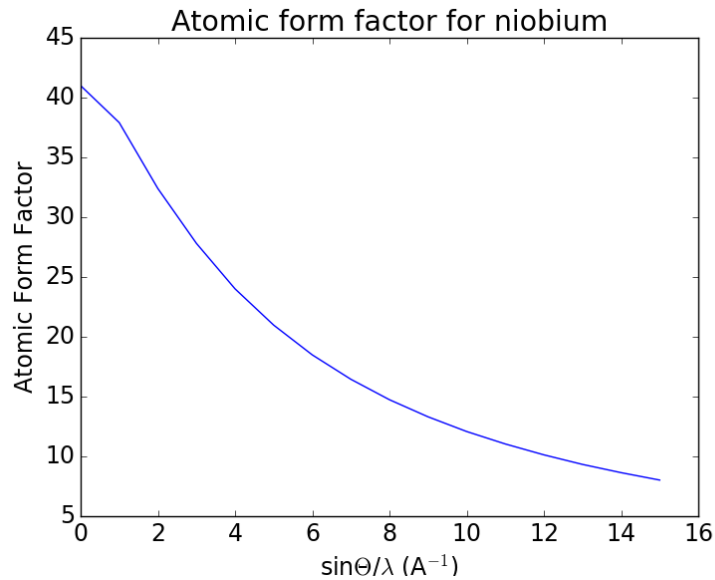
Figure 4.17: *The atomic form factor of Nb [48]. The form factor is linearly interpolated between experimental data points to create a continuous function such that correction factors can be calculated for every θ.*

The correction factor C_A is therefore the inverse of the atomic form factor. The correction factors applied to each image plate from shot 10268 are shown in figure 4.18.
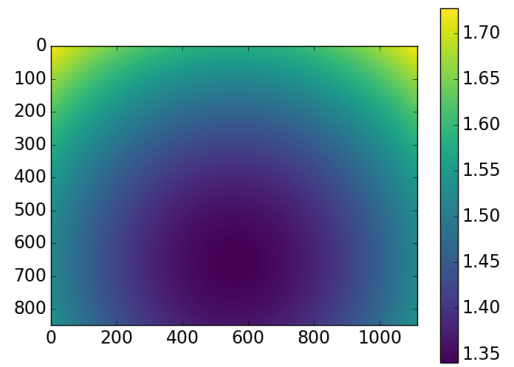
132
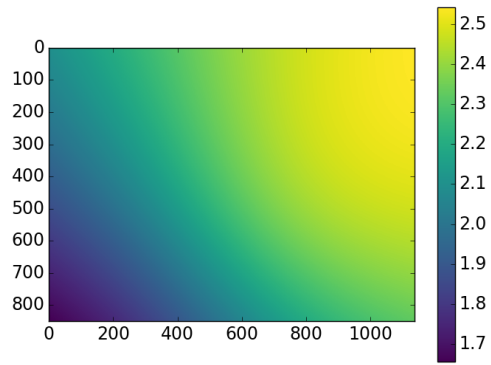
(a) Plate 1
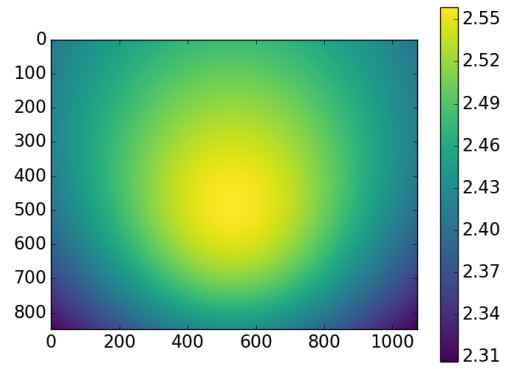
(b) Plate 2
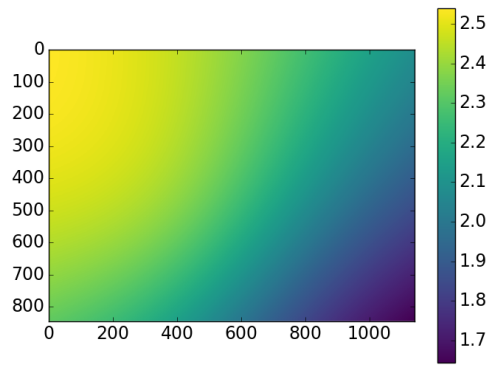
(c) Plate 3

(d) Plate 4

Figure 4.18: *The correction factors due to atomic form factor for application to the four image plates from shot 10268. The x and y axes correspond to pixel number. The colourbar to the right of each image indicates the correction factor for each colour in the image.*

Total intensity correction

The total correction factor C needed to account for each of these effects is

$$C = C_{LP}C_SC_FC_A \tag{4.14}$$

When applied to the original image intensity (in PSL units) I_R, a new corrected intensity is calculated $I_C = CI_R$. Note that I_C is not actually the original absolute intensity. To arrive at the original intensity would require quantitative knowledge of the x-ray source intensity and the probability of diffraction from the sample. This knowledge is unnecessary as the present analysis only requires knowledge of the relative intensity of diffraction from one diffraction ring to another. What matters is that I_C is proportional to the original scattered intensity.

The total correction applied to each image plate from shot 10268 are shown in figure 4.19. These images look very similar to the plots of C_S shown in fig 4.15, and so the attenuation due to the sample is the most important effect when correcting for intensity.

(a) Plate 1
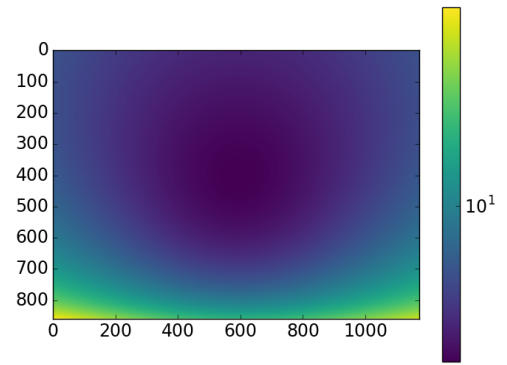
(b) Plate 2
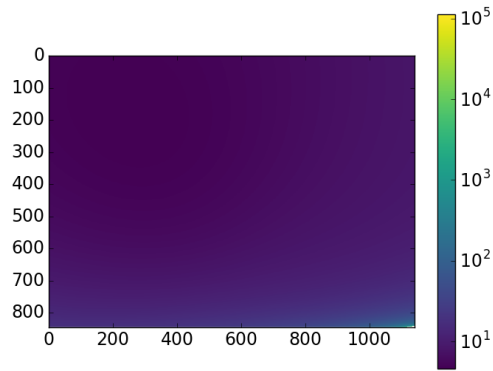
(c) Plate 3
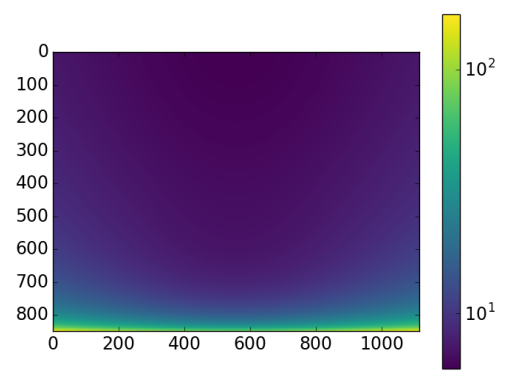
(d) Plate 4

Figure 4.19: *The total correction factors for application to the four image plates from shot 10268. The x and y axes 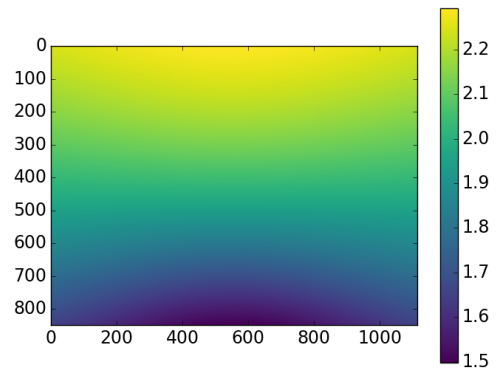correspond to pixel number. The colourbar to the right of each image indicates the correction factor for each colour in the image.*
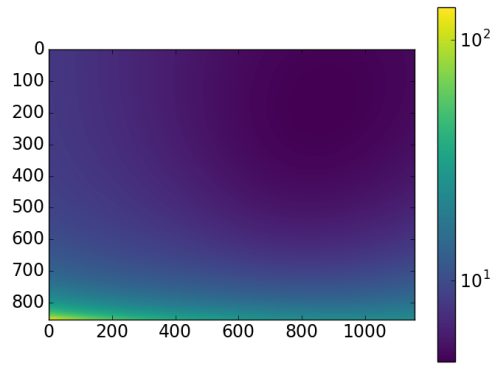
4.6.4   Finishing the image transformation

Now that the intensity of every pixel in each image has been corrected, the 2D histogram can be formed, shown in fig 4.20. The diffraction lines line up along $|\mathbf{G}^2|$ as expected. Since Nb is a BCC material, diffraction rings are expected at all even values of $|\mathbf{G}^2|$.
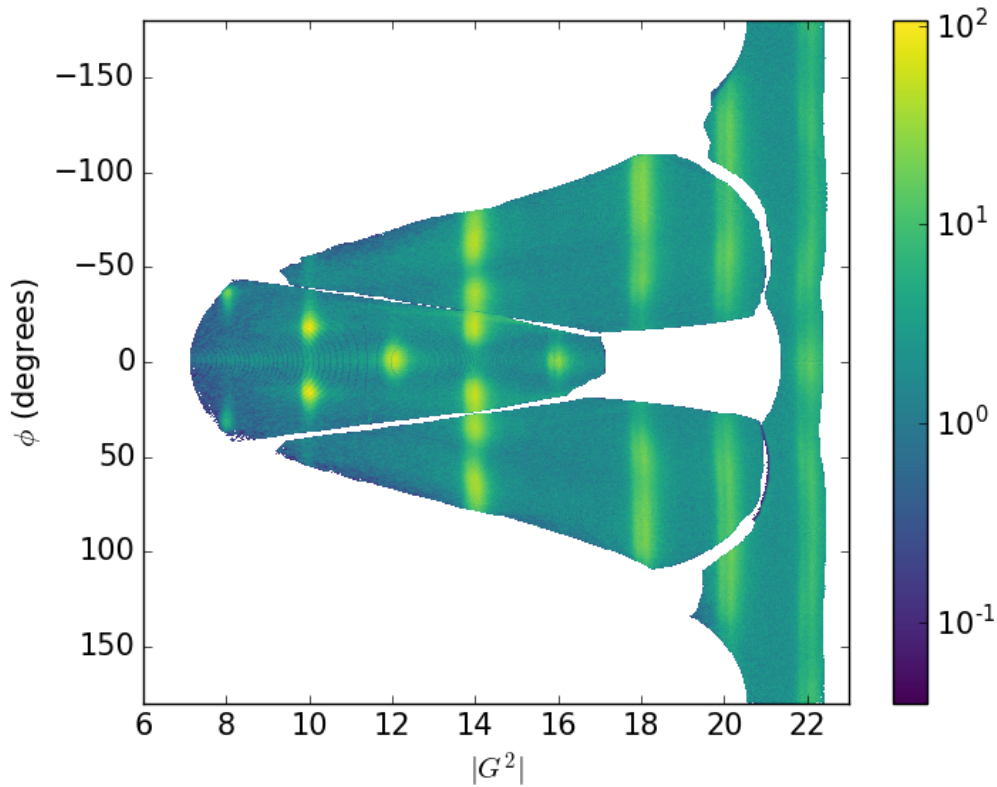
Figure 4.20: *The completed image transformation of plates 1 - 4 of shot 10268, showing static x-ray diffraction from Nb using a Zn x-ray source. The raw pixel intensities have been corrected for Lorentz-polarisation, attenuation through the Nb sample, attenuation through image-plate filters, and atomic form factor. This is a log-scale image as indicated by the colourbar to the right of the image.*

The diffraction rings are generally not uniform along ϕ. Instead, spotty diffraction

is observed this is the result of crystallographic texture in the Nb rolled foil. There is also a "smearing" of the diffraction peaks along $|\mathbf{G}^2|$. It is thought that this arises from diffraction of other wavelengths from the crystal; since the x-ray source is not a perfect delta function, and instead the x-ray source has a width, these surrounding wavelengths may diffract resulting in this low intensity smearing. This smear is removed during background subtraction.

Now that the image transformation is complete, the intensity values of each pixel can be summed across all values of ϕ, producing a graph of intensity vs. $|\mathbf{G}^2|$. This summed intensity is then divided by the number of ϕ bins contributing to the intensity, resulting in an integrated intensity per ϕ. A plot of the intensity per ϕ vs. $|\mathbf{G}^2|$ is shown in figure 4.21.
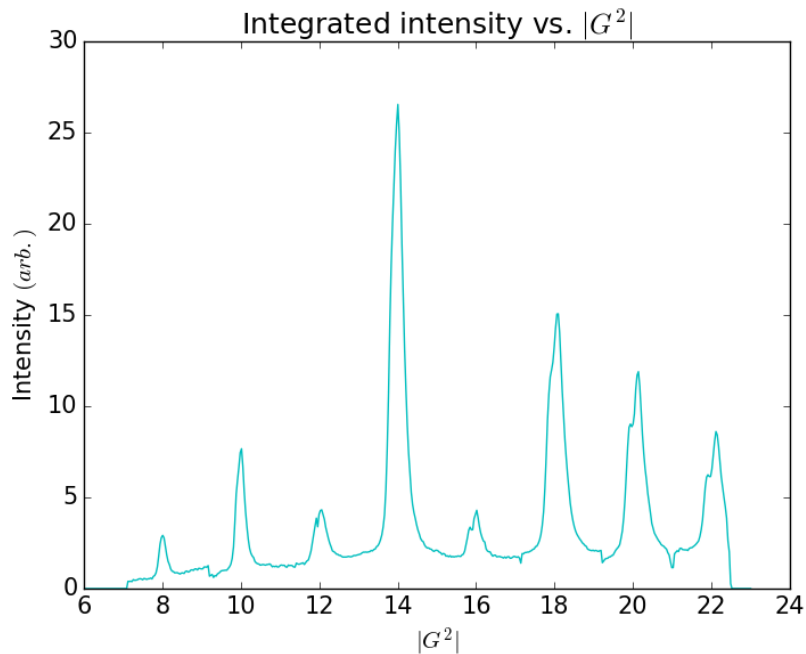
Figure 4.21: *The integrated intensity per ϕ vs. $|\mathbf{G}^2|$ of shot 10268.*

4.6.5 Background subtraction

Background is produced on this experiment from several sources. The first source of background is drive noise as previously discussed. As the energy of the drive laser increases, more high energy photons are produced as part of the drive noise, and so it is expected that noise is higher in images of higher pressure diffraction.

Another origin of background is the x-ray source. Since the facility uses a laser-driven x-ray source, the radiation generated is not monochromatic. Most of the excess x-rays are low in energy, and are broad in spectrum.

A final suspected source of background is secondary fluorescence. This is the absorption of high energy x-rays by other equipment in the chamber (namely, the VISAR payload) and subsequent re-emission. The evidence for this background source is a shadowing effect often observed on the image plates. This effect was only seen when the VISAR payload was inserted; the shadowing is caused by the blockage of some external x-ray source by the mirror of the BBXRD, indicating that the VISAR payload is the x-ray source responsible for this noise.

As previously stated filters were placed over the front surface of the image plates to absorb the lower energy x-ray noise, while still allowing high energy x-rays through. Nevertheless, some background gets through, and this is clearly seen on the image plate scans. Some post-processing must now be completed to subtract the background from the signal.

To approximate the background, the diffraction signal is masked (set to zero) and linearly interpolated as shown in figure 4.22. This interpolated image is then subtracted from the original image in an attempt to isolate the signal. Nearest neighbour interpolation was also pursued though it was found to generate a very

similar background image.
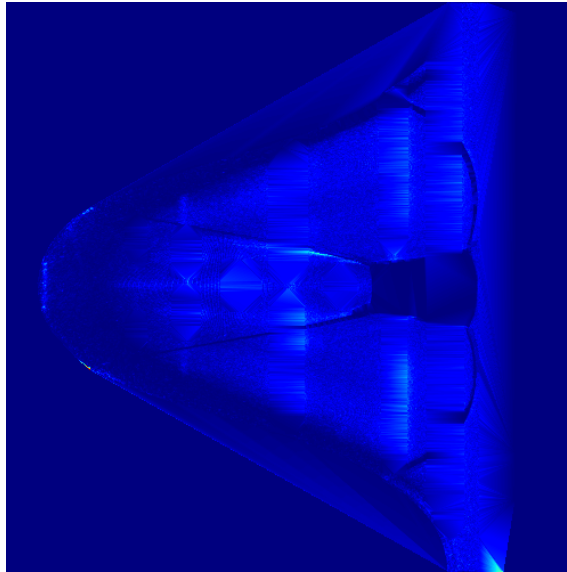
Figure 4.22: *The background image of shot 10268 where the diffraction signal is masked, and then linearly interpolated over the masked regions.*

Now that the background has been subtracted the integrated intensity is calculated again, as shown in 4.23. The background subtraction leaves some artefacts at the pedestal regions of the peaks.

4.6.6 Estimation of diffraction ring intensity

Now that background has been removed, the peak intensities are estimated by fitting a Gaussian to each peak as shown in fig 4.23. The fits were achieved by eye since a good fit using a fitting routine was difficult, given the pedestal artefacts observed on each peak. The area of these Gaussian is the integrated intensities of each reflection.
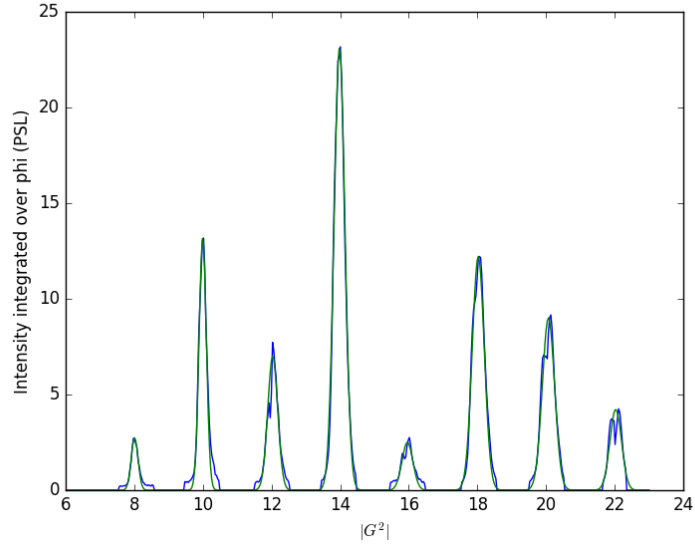
Figure 4.23: *Gaussian fits to the integrated intensities of shot 10268. The green line show the fitted Gaussians and the blue line shows the background subtracted signal.*

4.6.7 Texture correction

The work in this section is generously informed by John Foster, who originally simulated the texture of the Nb BCC foils used on this experiment. This work is reproduced by the author of this thesis so that the results may be applied to the present analysis.

The overall aim of the intensity corrections is to recover the intensity contributed to each reflection by each individual plane, since the Debye-Waller theory applies to this case. If the sample were an ideal powder there would be a uniform distribution of crystal grains within the sample. In the case of a powder, then, each reflection will be observed with contributions from planes according to the multiplicity. In the case of foil targets, this uniform distribution of grains is not present. Since a

non-uniform distribution of grains is present, a correction is required to compensate.

The texture present in a cold-rolled BCC foil is well studied [119]. The texture that is formed in this case is called an α-fibre texture. The symmetrical element of this fibre texture is characterised by three Euler angles $\alpha = 0°$, $\beta = 0 - 55°$, and $\gamma = 45°$. These Euler angles describe the crystal orientations present in a foil; β occupies a uniformly random angle between $0°$ and $55°$. These orientations arise from the rolling of the foil between rollers at high pressures. This process arranges the grains symmetrically about the rolling direction. The grain distribution is also top-bottom symmetric. Therefore to generate the full texture of the foil, the fibre element described above must be mirrored through the plane of the rolling direction, and through the plane of the sample.

(a)   (b)
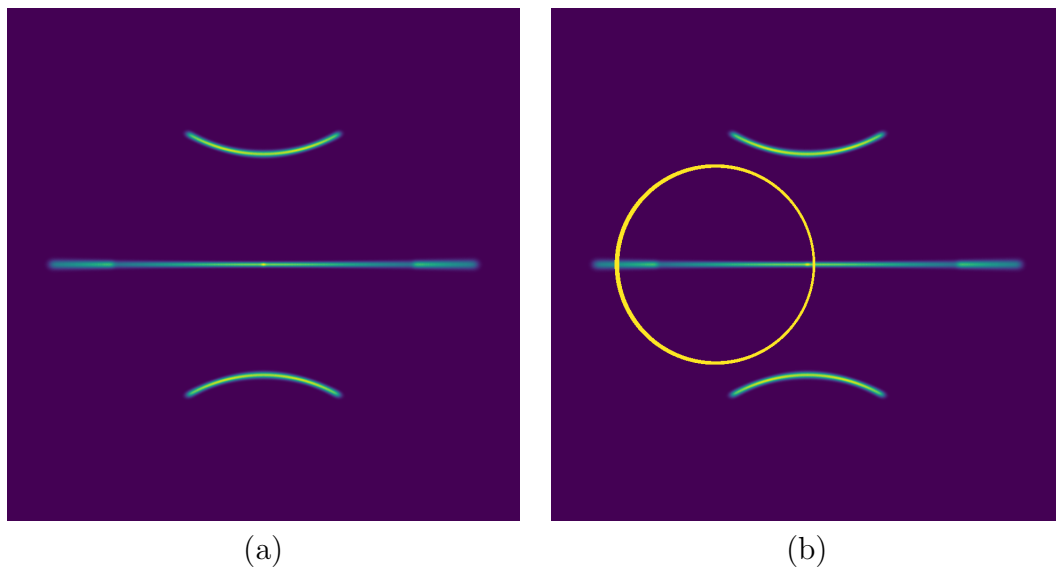
Figure 4.24: *(a) A stereographic projection of the $< 2\,2\,2 >$ family of directions (b) The ring shows the intersection of the Ewald sphere with the unit sphere, projected onto the plane. The intersection of this yellow ring with the projected vectors represents the grains that meet the Bragg condition and thus produce diffraction.*

For each reflection $|\mathbf{G}^2|$, a set of vectors corresponding to the contributing planes is generated. For example, the set of vectors for the plane $|\mathbf{G}^2| = 12$ will contain all unique members of the family of vectors $< 2\ 2\ 2 >$. These vectors are then normalised so that they all start at the origin and terminate on the unit sphere. These vectors are then rotated through the Euler angles stated above. In the case of β, a random angle is selected between $0°$ and $55°$ using a uniformly random number generator. Each of these Euler angles is summed with a random angle $d\alpha$, $d\beta$, and $d\gamma$ selected from a Gaussian distribution of random numbers with full-width half maximum of $2.0°$ and centred on 0 so that negative values might arise. These slight variations are introduced to account for random variations in the sample texture. The final Euler angles used to rotate the quiver of vectors is $(\alpha + d\alpha, \beta + d\beta, \gamma + d\gamma)$. After the rotation is applied the set of unit vectors is projected stereographically onto the $z = -1$ plane. This projection is a convenient way of representing the positions of vectors in the unit sphere.

This process of rotation and projection is repeated 3.6×10^6 times. This repetition allows the plane to be populated sufficiently such that the distribution of grains is well represented. The projection is then super-imposed with symmetrical images corresponding to the symmetry through the rolling direction and the top-bottom symmetry. The result is a projection representing all plane orientations Figure 4.24(a) shows an example of such a figure. Only the vectors in the upper half of the unit sphere are shown here, since these vectors project inside a unit circle. Vectors in the lower hemisphere of the unit sphere are always projected outside this unit circle. Vectors projected outside the unit circle present a difficulty since these vectors can appear anywhere outside of the unit circle up to infinity. Since these values are
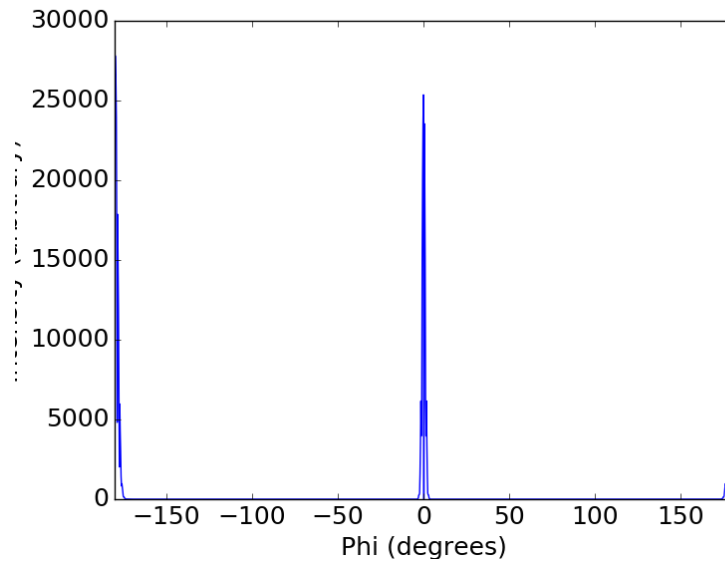
Figure 4.25: *The predicted intensity profile of the reflecting {2 2 2} planes arising from texture.*

conveniently unnecessary for the present analysis, they are neglected completely.

The Ewald sphere may also be constructed, representing all possible directions of elastic scattering. Where the Ewald sphere intersects with a reciprocal lattice direction (equivalently, the plane normal vectors) diffraction will occur. In figure 4.24(b) the intersection of the Ewald sphere with the unit sphere is projected onto the plane as a yellow circle. Where the circle intersects with the projected grain orientations, the Bragg condition is met. A larger number of grains meeting the Bragg condition results in a higher predicted intensity at that Bragg angle. The initial predicted intensity as a function of ϕ for the $< 2\ 2\ 2 >$ family of directions is shown in figure 4.25.
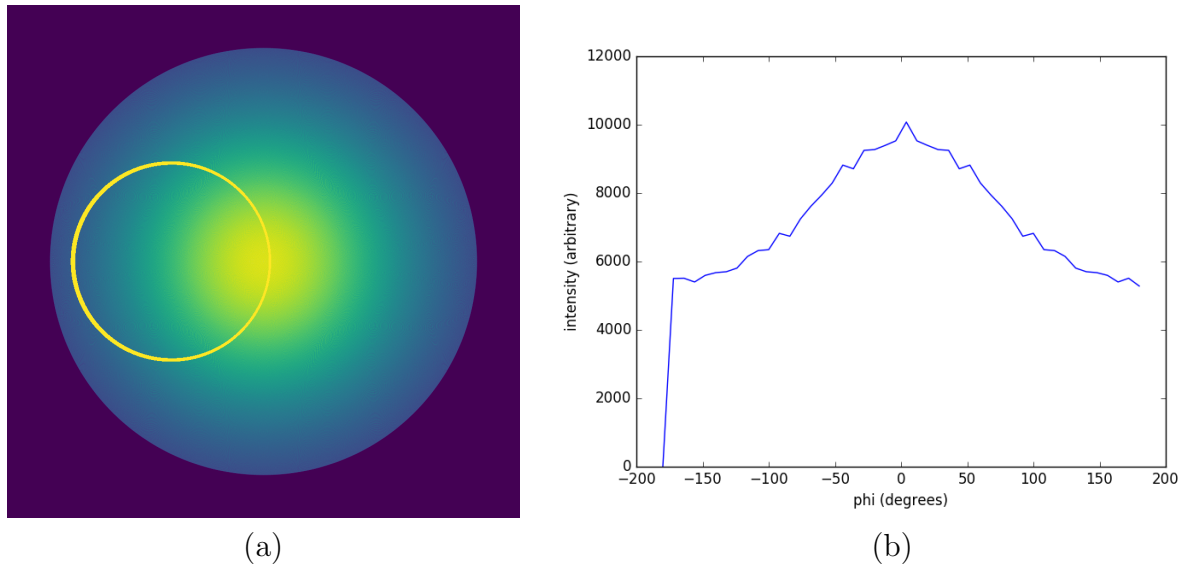
Figure 4.26: *(a) A stereographic projection of the planes in a powder. The ring shows the intersection of the Ewald sphere with the unit sphere, projected onto the plane. The intersection of this yellow ring with the projected vectors represents the grains that meet the Bragg condition and thus produce diffraction. (b) The intensity of diffraction as a function of ϕ.*

This projection method used does not preserve intensity. To demonstrate this, a powder pattern is generated by uniformly distributing vectors about the unit sphere. These vectors undergo the same stereographic projection discussed previously; the result is shown in figure 4.26(a). As is seen in figure 4.26(b), the intensity is not uniform about the ring, despite the uniform distribution of vectors about the unit sphere. By dividing the textured pattern in figure 4.25 by the powder profile of figure 4.26(b), a corrected prediction for profile intensity in the textured sample is extracted. Note that the projected powder image of figure 4.26(a) is identical for each reflection, however the profile will look different due to a differing intersection with the Ewald sphere for each reflection. Therefore this correction leaves the effect of multiplicity on intensity intact.

144

Texture projection of {2 2 0}   Predicted intensity from {2 2 0}

Texture projection of {3 1 0}   Predicted intensity from {3 1 0}

Texture projection of {2 2 2}   Predicted intensity from {2 2 2}
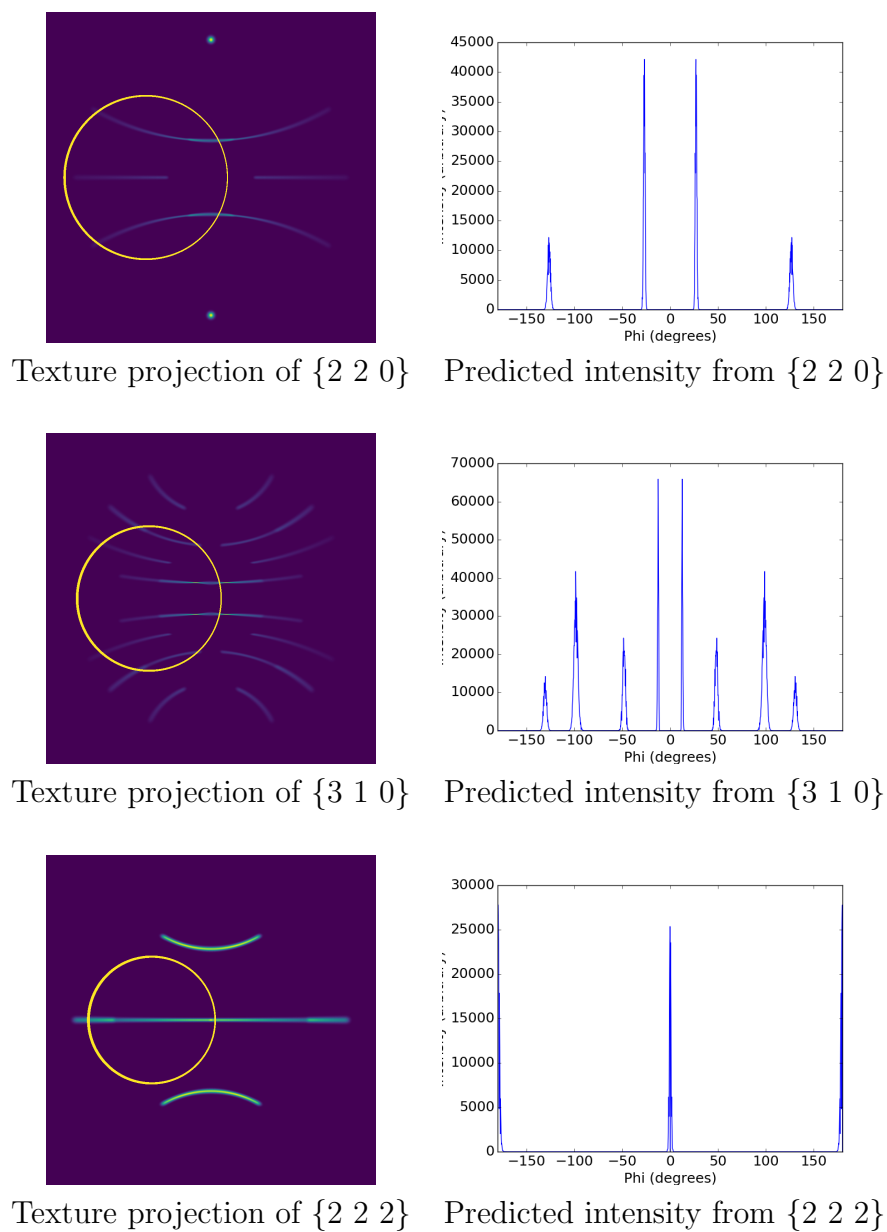
Figure 4.27

This process was undertaken for every reflection present in the diffraction images from shot 10268. The projected image for each reflection along with the corresponding

145

Texture projection of {4 0 0}   Predicted intensity from {4 0 0}

Texture projection of {4 1 1}   Predicted intensity from {4 1 1}

Texture projection of {3 3 0}   Predicted intensity from {3 3 0}
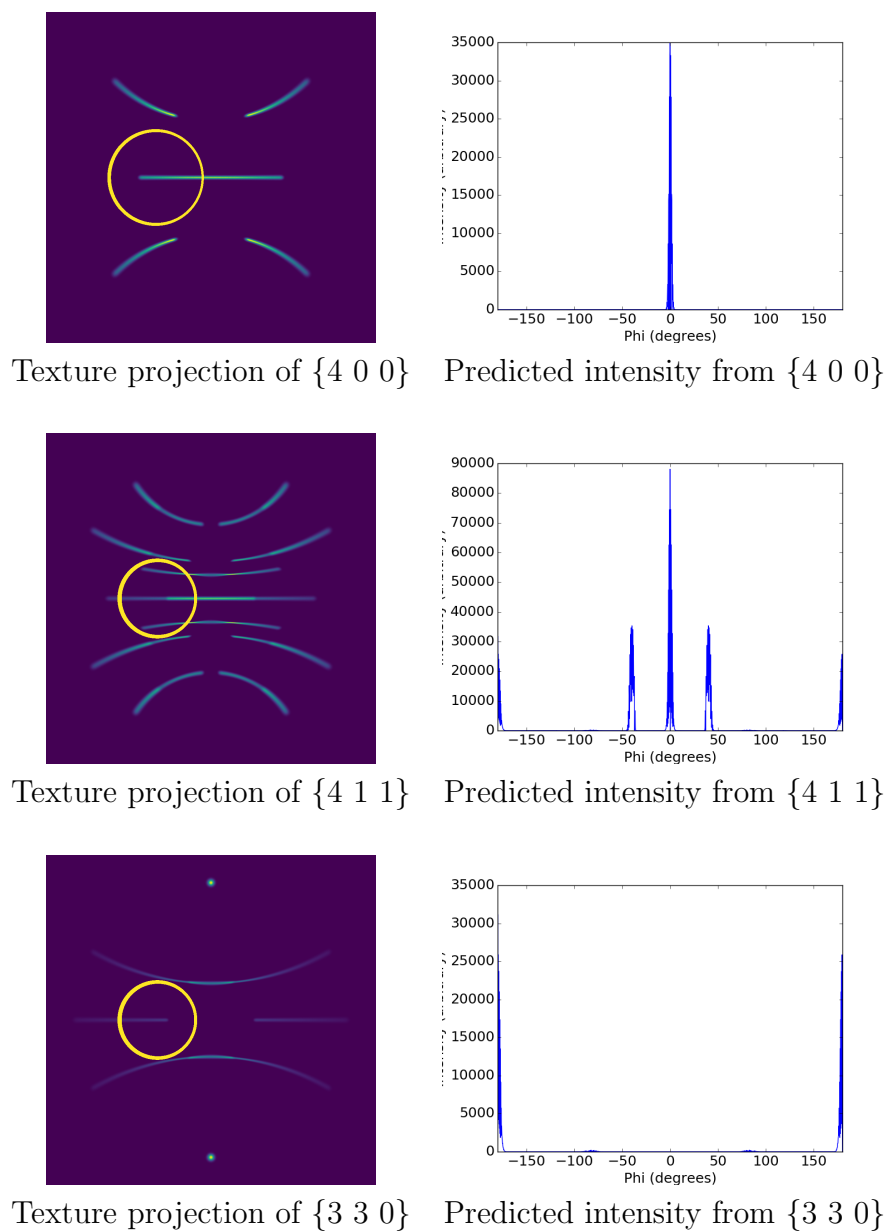
Figure 4.28

intensity profile are shown in figures 4.27 - 4.29. The diffraction ring is seen to graze the texture spots in a number of cases. The texture profiles in these cases

Texture projection of {4 2 0}   Predicted intensity from {4 2 0}

Texture projection of {3 3 2}   Predicted intensity from {3 3 2}
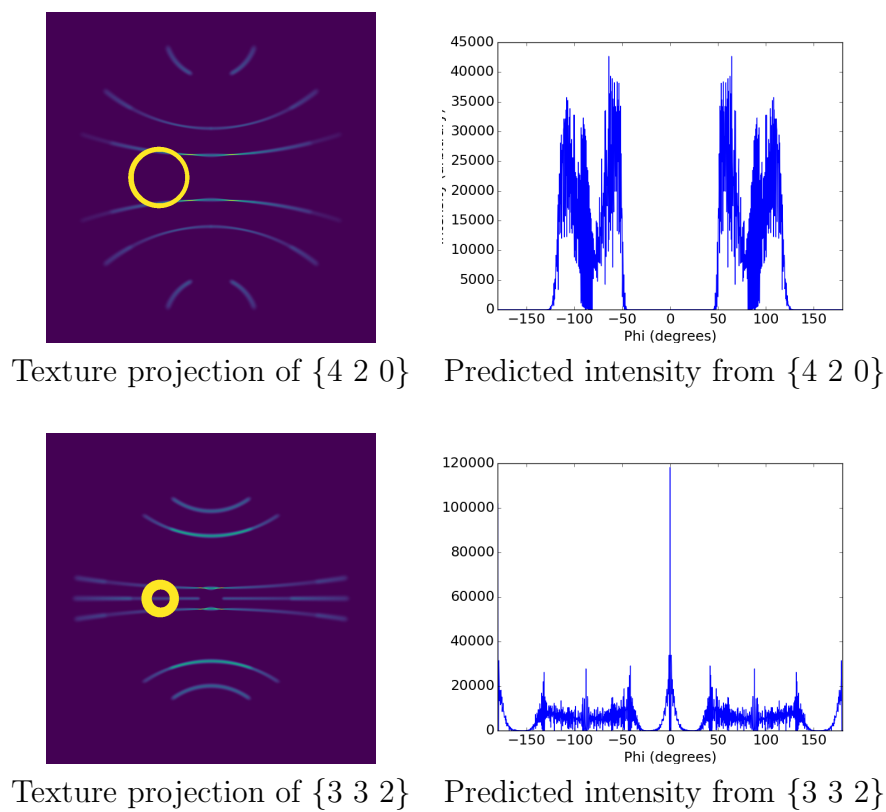
Figure 4.29

are therefore poorly constrained, and it it likely to result in a poor prediction of intensity where this is the case.

The whole ϕ range of each ring was not accessed on this experiment, and so texture profiles should be restricted to account for this. The intensity observed on experiment should be divided by the total predicted intensity in the restricted ϕ region. This will retrieve the relative intensity reflected by each individual plane. Note that this will automatically correct for multiplicity. This will also correct for the geometrical part of the Lorentz-polarisation factor arising from the intersection

147

of the finite-width Ewald sphere with the finite-width reciprocal lattice.

4.7   Results

Having transformed and corrected the diffraction images, the integrated intensities may now be used to attempt a temperature measurement.

The Debye-Waller plot for shot 10268 before the texture correction is shown in 4.30. The line of best fit has a positive slope; the Debye-Waller effect predicts a negative slope. Upon application of the texture correction, as shown in figure 4.31, the situation is improved such that a general trend of decreasing intensity with $\mathbf{G}^2$ is observed. Using the literature Debye temperature value of $\Theta_D = 260$ K, the temperature of the static sample is measured here to be 1142 K. The substantial scatter about the line of best fit indicates that the simple model of texture used to generate the texture correction is not sufficient. A reference sample texture is therefore necessary.

Since the temperature of the static material is known to be 300 K, an additional correction can be applied to each intensity so that the appropriate relative intensities are recovered. Figure 4.32 shows the static intensity data from shot 10268 corrected to give a $T = 300$ K. The corrections applied here are in essence a reference texture correction. The validity of the reference correction can be verified by applying them to static diffraction intensities on another shot. Note that there is an implicit assumption that texture is the same in both samples.

To test the texture reference gained from shot 10268, another shot was selected for analysis; the chosen shot was 10257 which was shocked to $P = 20$ GPa. The
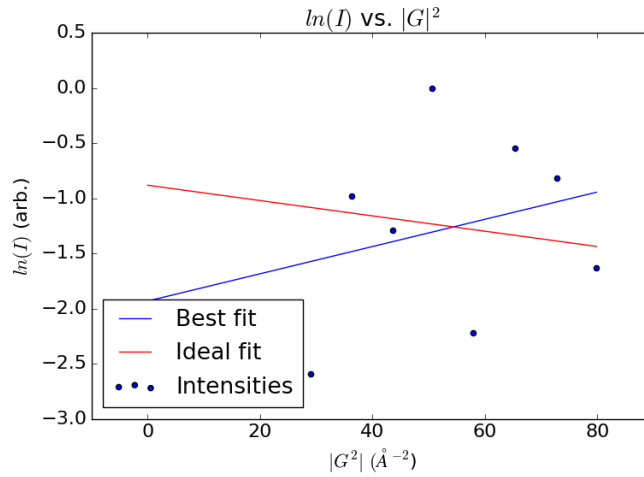
Figure 4.30: *The Debye-Waller plot for shot 10268 with no texture correction.*
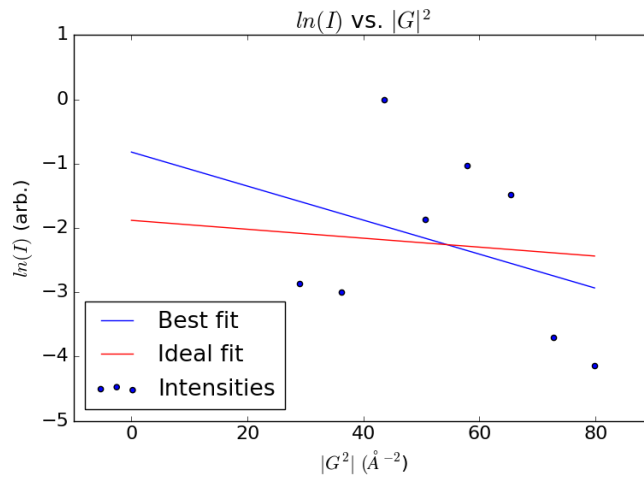
Figure 4.31: *The Debye-Waller plot for shot 10268 measuring temperature from a static diffraction image. From the line of best fit, $T = 1142$ K. The ideal line shows the slope required for a measurement of $T = 300$ K.*

transformed and corrected diffraction image shown in figure 4.33 displays diffraction from both the static material and the shocked material. The change of diffraction position when assuming hydrostatic compression indicates a volumetric compression
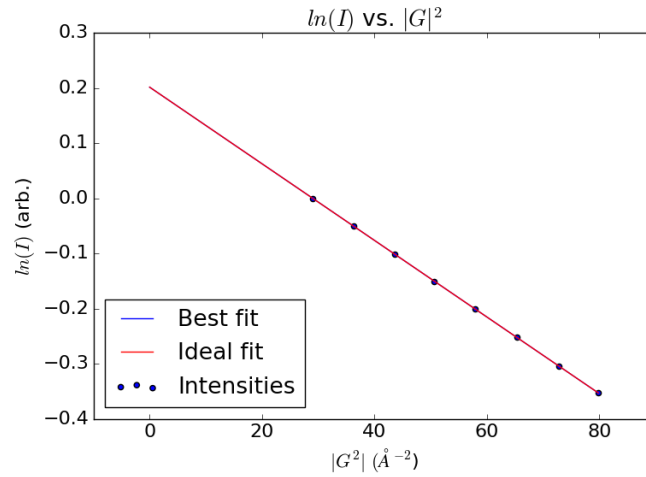
Figure 4.32: *The Debye-Waller plot for shot 10268, corrected such that all points now lie on the line corresponding to $T = 300$ K.*

of $V/V_0 = 0.90$.
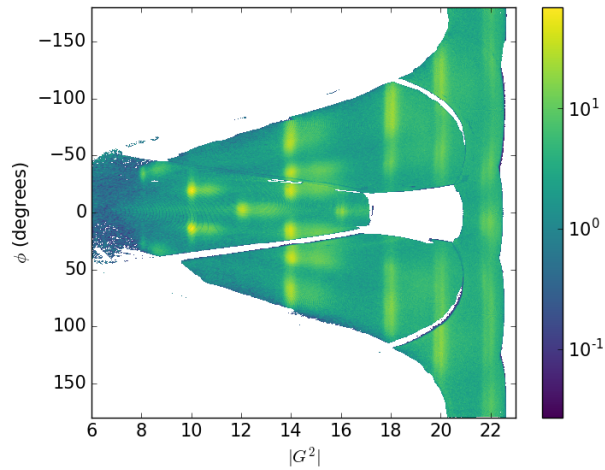
Figure 4.33: *The transformed and corrected diffraction image from shot 10257.*

The static signal was isolated using the same background subtraction method mentioned previously. As part of the background subtraction procedure, the driven

signal is also removed. Since the driven signal is broad, it is difficult to separate the static and driven signals, so the background subtraction is of a lower quality when compared to the subtraction performed on shot 10268. The integrated intensity of shot 10257 after background subtraction is shown in figure 4.34. Gaussians are fit once more by eye. This time the Gaussians are fit to both the static signal and the driven signal. The large breadth and small amplitude of the driven peaks make for a loosely constrained fit. This is especially true of the driven peaks at higher Bragg angles due to their apparent overlap with the static peaks. The driven intensities corresponding to $\mathbf{G}^2 = 16, 20$, and 21 are omitted, since no clear peak is apparent.
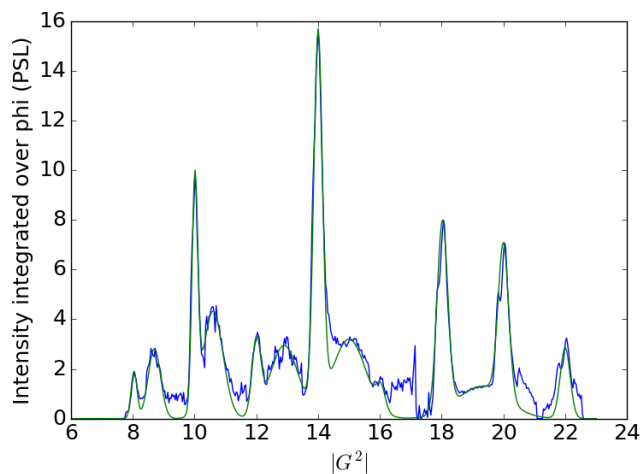
Figure 4.34: *The integrated intensity of shot 10257 after background subtraction. The green curve shows the sum of Gaussians fitted to both the static and driven signal.*

The reference correction collected from shot 10268 can now be tested on the static signal of 10257. Plot 4.35 shows the static signal of shot 10257, with the reference corrections from 10268 applied. The temperature measurement is much improved to $T = 260$ K. The scatter is generally low except for the peaks $\mathbf{G}^2 = 12$

and 16. Note that both of these peaks have a relatively low intensity in figure 4.34; the difficult background subtraction procedure is likely to have the largest impact on these peaks.
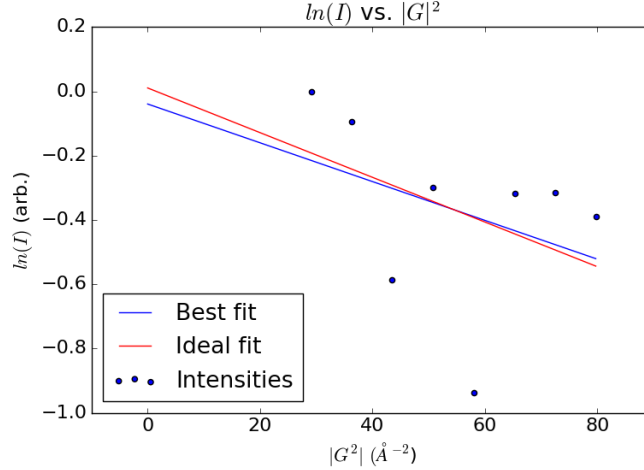
Figure 4.35: *The Debye-Waller plot of the static signal from shot 10257, with the reference correction factors from shot 10268 applied. From the line of best fit, $T = 260$ K. The ideal line shows the slope required for a measurement of $T = 300$ K.*

A temperature measurement will now be attempted for the driven diffraction. Instead of using the reference correction from shot 10268, a reference correction will be derived from the static diffraction in the same image. Figure 4.36 shows the obtained Debye-Waller plot. The scatter is noticeably improved by using the static signal from the same shot to make the reference correction. By using the approximation $\Gamma/V = $ constant, as in section 3.5, a value of Θ_D can be calculated as 310 K. With this Debye temperature, the temperature is measured to be 2396 K. At this pressure, the temperature is expected to be 450 K.

The negative effect of background subtraction will be even more pronounced for driven diffraction given the small amplitude and large breadth of driven peaks. This,

combined with the loosely constrained Gaussian fits, results in a very challenging temperature measurement.
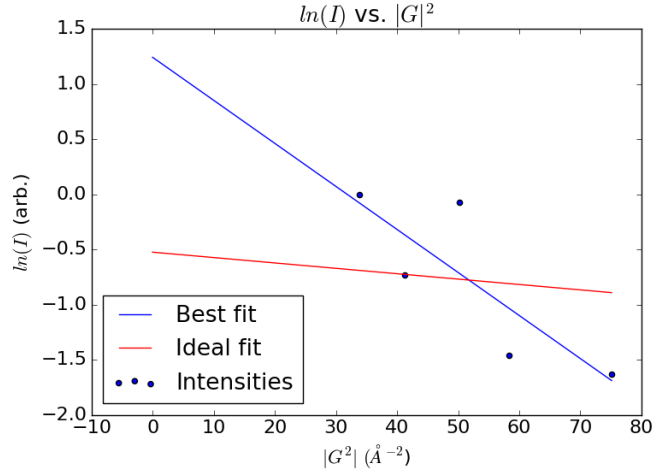
Figure 4.36: *The Debye-Waller plot of the driven signal from shot 10257. Using $\Theta_D = 310$ K and from the line of best fit, $T = 2396$ K. The ideal line shows the slope required for a measurement of $T = 300$ K.*

4.8   Conclusions and future work

The work performed in this chapter highlighted substantial complications that could only be identified with experiment. These challenges are summarised here. Their remedies are recommended below.

The main confounding factor for the Debye-Waller thermometer was the difficulty in extracting accurate peak intensities from driven signal. A poor model of the background resulted in a background subtraction method that significantly altered the driven signal intensities due to their large widths and low amplitudes. These same properties also made the accurate fitting of Gaussians to these peaks very

challenging. Any future work will require extra care when considering background subtraction.

Other useful insights were also gained on this experiment. Uncorrected texture has the potential to drastically alter the apparent Debye-Waller behaviour of the material. A simple texture model was found to qualitatively predict the positions of diffraction, but it was insufficient with regards to correcting diffraction intensities for the effect of crystallographic texture. A direct reference to the investigated material is much preferred. The double pulsed backlighter used on this experiment was a convenient tool for acquiring this reference correction. Note that the application of a reference correction derived from static signal in this way assumes that texture will not evolve upon compression. Also note that the effect of crystallographic texture on diffraction is dependent on the orientation of the sample with respect to the incident x-ray beam; an on-shot reference with a double pulsed backlighter removes the need for careful orientation of the sample.

When considering future experimental designs, the quality of diffraction signal from driven material should be the primary concern. A brighter, narrower x-ray source will increase the signal to noise ratio. An x-ray free electron laser (XFEL) is the ideal candidate for such an experiment, given the bright, high-quality x-rays produced by such an instrument. More sophisticated methods of modelling the background may also be beneficial.

With regards to the sample, a material with a uniform distribution of grains such as a powder would eliminate the need for texture correction entirely. It would also eliminate the assumption that texture does not evolve on compression; instead, the evolution of texture might be reliably observed.

Chapter 5

Conclusions and Future Work

5.1 Summary

The applicability and limitations of the Debye-Waller effect for the measurement of temperature have been investigated both through simulation and experiment.

The simulation work of chapter 3 began with a critical assessment of previous work undertaken by Murphy et al [37]. Material strength has been shown to be of little consequence to the technique. The impact of the choice of Debye temperature model was also assessed and, in the case of Cu, found to introduce < 2 % error in the measurement of temperature. Such an error is acceptable given the large errors associated with competing thermometry schemes [23].

The impact of dislocations on the Debye-Waller effect was investigated. An analysis of the theory by Wilkens [63] predicted no impact of dislocations on the Debye-Waller effect. Molecular dynamics simulations show that this is not true; at high enough densities, the presence of dislocations causes an over-prediction of

temperature. The over-prediction tends to increase with dislocation density. The Wilkens model makes the assumption that dislocations are sufficiently separated such that the strain fields from each dislocation do not interact. It is proposed that this may not be valid at the dislocation densities observed in laser shock experiments, though more work is required to confirm this. At such high dislocation densities, this result indicates that the Wilkens model is no longer valid.

The results of chapter 3 indicate the fundamental viability of the technique, though crystal imperfections are a confounding factor that increase the apparent temperature. Knowledge of the dislocation density may not be sufficient to correct for this effect, since a simple relationship is not expected between temperature error and dislocation density due to differences in dislocation character. An experimentalist must therefore also have knowledge of the quantity of edge- and screw-like dislocations and their orientations with respect to the diffracting beam. Such knowledge is not yet currently available on laser shock experiments; this result reveals a substantial hurdle to temperature measurement using the Debye-Waller effect.

The experiment of chapter 4 described the first known laser shock experiment tailor-made for the investigation of the Debye-Waller thermometer. A number of challenges were exposed in the course of this investigation.

Crystallographic texture dramatically alters the reflected intensities from a sample. A simple model of crystallographic texture was implemented to correct for this. Qualitatively, this model predicts the positions of diffraction, and the resulting texture correction significantly improved the temperature measurement; however, it was shown that, instead of using a simple model of texture to correct the intensities, the temperature measurement is much better improved using a reference texture

from the sample itself. In particular, a double-pulse backlighter was useful so that misalignment of the sample with with respect to the reference was not possible.

The process of subtracting background from intensity profiles causes substantial damage to the measurements of diffraction signal from shocked material. Removing background without removing valuable diffraction signal is a significant challenge. Additionally, the low amplitude and large width of the driven reflections makes for a poorly resolved peak. The overall result is a temperature measurement much higher than expected, with large uncertainty.

While the results of both simulations and experiment have exposed a number of challenges regarding this technique, solutions may now be sought. Recommendations of future avenues of work are provided in the next section.

5.2   Suggestions for future work

With regards to simulations, a predictive model of the impact of dislocations on the Debye-Waller thermometer should be constructed. This will require the generation of lower dislocation densities to investigate the minimum density required for this effect to be triggered; such low densities were not analysed in this thesis due to a lack of control over the number of dislocations present in a sample. In addition, the dependence of the Debye-Waller effect on dislocation type should be assessed. Other defect types such as stacking faults should also be investigated.

The impact of dislocations on experiment also needs to be well characterised. It is likely that a strong understanding of the dislocation density and type is required to make a temperature measurement. The compression of single crystals may be a

good candidate for such an experiment given their predictable plasticity modes.

Extremely low background is a necessity for this technique. Laser-plasma x-ray sources may produce too much background for practical application. It is therefore recommended that future investigations are performed using an X-ray Free Electron Laser (XFEL) such as the European XFEL, or LCLS, due to their exceptional signal to noise ratios and narrow beam energies. The high repetition rates of these facilities means that a reference diffraction pattern and a driven diffraction pattern can be obtained separately. A combination of the low background and narrow energy profile should make for well resolved diffraction from the shocked state.

5.3   In closing

In the production of this thesis, the understanding of the Debye-Waller thermometer has been progressed. It is hoped that future investigators may take the lessons learned here and judiciously apply them to their studies.

In broader terms, it is hoped that robust temperature diagnostics are developed to aid in the discovery of useful materials and technologies. High pressure states have the potential to change our understanding of the physical world. The fruits of this work are eagerly anticipated.

Appendices

Appendix A

Multiplicities in BCC Structures

The multiplicity factors for a BCC structure are given below in table A.1. Note that the $\mathbf{G}^2 = 18$ reflection receives contributions from both the (3 3 0) and (4 1 1) families of planes.

$\mathbf{G}^2$	Multiplicity	$\mathbf{G}^2$	Multiplicity
2	12	14	48
4	6	16	6
6	24	18	36
8	12	20	24
10	24	22	24
12	8	24	24

Table A.1: *Multiplicities in BCC polycrystals.*

Appendix B

Multiplicities in FCC Structures

The multiplicity factors for a FCC structure are given below in table B.1. Note that the $\mathbf{G}^2 = 27$ reflection receives contributions from both the (3 3 3) and (5 1 1) families of planes.

$\mathbf{G}^2$	Multiplicity	$\mathbf{G}^2$	Multiplicity
3	8	19	24
4	6	20	24
8	12	24	24
11	24	27	32
12	8	32	12
16	6	36	6

Table B.1: *Multiplicities in FCC polycrystals.*

Appendix C

Overview of shots taken at Orion

A summary of useful data shots taken on the Orion experiment described in chapter 4. Two sample types are included: foil and slurry. Foil refers to cold-rolled Nb foils. Slurry refers to attempts at making targets with no texture. Attempts were made to drive the Nb slurry samples, but analysis of these images did not provide a conclusive pressure. It is proposed that the slurry target does not support a well-formed single shock front, and so the diffraction images obtained from driven slurry samples contain many different pressures simultaneously. The pressures for these samples are therefore reported as NA. The pressure in some entries is marked with a "-". The inferred pressure from diffraction was not calculated for these shots.

Shots 10268 and 10289 were carried out with an "early" backlighter. This means that the sample was driven, but the x-rays were intentionally timed such that the diffraction pattern is generated before the shock has traversed the sample. This allows the drive noise to be captured at the same time as the static diffraction.

Shot ID	Target Type	Pressure (GPa)	Backlighter
10048	Nb rolled foil	0	Fe
10049	Nb rolled foil	0	Fe
10050	Nb rolled foil	-	Fe
10054	Nb slurry	0	Fe
10055	Nb rolled foil	-	Fe
10056	Nb rolled foil	-	Fe
10057	Nb rolled foil	-	Fe
10241	Nb rolled foil	-	Cu
10243	Nb rolled foil	0	Zn
10244	Nb rolled foil	∼100	Cu
10246	Nb rolled foil	∼70	Zn
10247	Nb rolled foil	∼70	Zn
10249	Nb rolled foil	∼40	Zn
10251	Nb rolled foil	∼40	Zn
10254	Nb rolled foil	∼40	Zn
10256	Nb rolled foil	∼20	Zn
10257	Nb rolled foil	19	Zn
10258	Nb rolled foil	∼45	Zn
10259	Nb rolled foil	∼45	Zn
10260	Nb rolled foil	∼40	Zn
10262	Nb rolled foil	72	Zn
10263	Nb rolled foil	∼60	Zn

Table C.1 continued from previous page

Shot ID	Target Type	Pressure (GPa)	Backlighter
10268	Nb rolled foil	$\sim$70	Zn - early
10270	Nb rolled foil	$\sim$80	Fe
10271	Nb rolled foil	$\sim$80	Zn
10272	Nb rolled foil	$\sim$80	Fe
10274	Nb rolled foil	$\sim$80	Fe
10277	Nb slurry	0	Fe
10279	Nb slurry	NA	Cu
10280	Nb slurry	NA	Cu
10281	Nb slurry	NA	Cu
10282	Nb rolled foil	-	Cu
10283	Nb rolled foil	$\sim$60	Fe
10284	Nb rolled foil	$\sim$40	Fe
10285	Nb slurry	NA	Zn
10286	Nb rolled foil	$\sim$20	Fe
10287	Nb rolled foil	$\sim$70	Zn
10288	Nb rolled foil	$\sim$40	Fe
10289	Nb rolled foil	0	Fe - early
10290	Nb rolled foil - alternative texture	$\sim$60	Zn
10291	Nb slurry	NA	Zn

Table C.1: *A summary table of data taken from the Orion experiment.*

Bibliography

[1] L. G. C. E. Pugh. Resting ventilation and alveolar air on Mount Everest: with remarks on the relation of barometric pressure to altitude in mountains. *J Physiol*, 135(3):590–610, March 1957.

[2] Deepest scuba dive (male), https://www.guinnessworldrecords.com/world-records/, retrieved on 25/09/2019.

[3] Laura Robin Benedetti, Jeffrey H. Nguyen, Wendell A. Caldwell, Hongjian Liu, Michael Kruger, and Raymond Jeanloz. Dissociation of CH4 at High Pressures and Temperatures: Diamond Formation in Giant Planet Interiors? *Science*, 286(5437):100–102, October 1999.

[4] D. T. Casey et al. Thermonuclear reactions probed at stellar-core conditions with laser-based inertial-confinement fusion. *Nature Physics*, 13(12):1227–1231, December 2017.

[5] G. J. Piermarini and S. Block. Ultrahigh pressure diamondanvil cell and several semiconductor phase transition pressures in relation to the fixed point pressure scale. *Review of Scientific Instruments*, 46(8):973–979, August 1975.

[6] Mohamed Zaghoo, Ashkan Salamat, and Isaac F. Silvera. Evidence of a first-order phase transition to metallic hydrogen. *Phys. Rev. B*, 93(15):155128, April 2016.

[7] Ranga P. Dias and Isaac F. Silvera. Observation of the Wigner-Huntington transition to metallic hydrogen. *Science*, 355(6326):715–718, February 2017.

[8] John M. Walsh and Russell H. Christian. Equation of State of Metals from Shock Wave Measurements. *Physical Review*, 97(6):1544–1556, March 1955.

[9] C. E. Ragan III, M. G. Silbert, and B. C. Diven. Shock compression of molybdenum to 2.0 TPa by means of a nuclear explosion. *Journal of Applied Physics*, 48(7):2860–2870, July 1977.

[10] A. H. Jones, W. M. Isbell, and C. J. Maiden. Measurement of the VeryHighPressure Properties of Materials using a LightGas Gun. *Journal of Applied Physics*, 37(9):3493–3499, August 1966.

[11] D. B. Reisman, A. Toor, R. C. Cauble, C. A. Hall, J. R. Asay, M. D. Knudson, and M. D. Furnish. Magnetically driven isentropic compression experiments on the Z accelerator. *Journal of Applied Physics*, 89(3):1625–1633, January 2001.

[12] Gerold Yonas. Fusion and the Z Pinch. *Scientific American*, 279(2):40–47, 1998.

[13] Zhaoyan Zhang and George Gogos. Theory of shock wave propagation during laser ablation. *Phys. Rev. B*, 69(23):235403, June 2004.

[14] F. Cottet, M. Hallouin, J. P. Romain, R. Fabbro, B. Faral, and H. Pepin. Enhancement of a laserdriven shock wave up to 10 TPa by the impedancematch technique. *Appl. Phys. Lett.*, 47(7):678–680, October 1985.

[15] S. Le Pape et al. Fusion Energy Output Greater than the Kinetic Energy of an Imploding Shell at the National Ignition Facility. *Phys. Rev. Lett.*, 120(24):245003, June 2018.

[16] Bruce A. Remington, R. Paul Drake, Hideaki Takabe, and David Arnett. A review of astrophysics experiments on intense lasers. *Physics of Plasmas*, 7(5):1641–1652, May 2000.

[17] D. H. Kalantar, J. F. Belak, G. W. Collins, J. D. Colvin, H. M. Davies, J. H. Eggert, T. C. Germann, J. Hawreliak, B. L. Holian, K. Kadau, P. S. Lomdahl, H. E. Lorenzana, M. A. Meyers, K. Rosolankova, M. S. Schneider, J. Sheppard, J. S. Stlken, and J. S. Wark. Direct Observation of the Transition in Shock-Compressed Iron via Nanosecond X-Ray Diffraction. *Physical Review Letters*, 95(7), August 2005.

[18] Adrien Denoeud, Norimasa Ozaki, Alessandra Benuzzi-Mounaix, Hiroyuki Uranishi, Yoshihiko Kondo, Ryosuke Kodama, Erik Brambrink, Alessandra Ravasio, Maimouna Bocoum, Jean-Michel Boudenne, Marion Harmand, Franois Guyot, Stephane Mazevet, David Riley, Mikako Makita, Takayoshi Sano, Youichi Sakawa, Yuichi Inubushi, Gianluca Gregori, Michel Koenig, and Guillaume Morard. Dynamic X-ray diffraction observation of shocked solid iron up to 170 GPa. *Proceedings of the National Academy of Sciences*, 113(28):7745–7749, July 2016.

[19] L. B. Da Silva, P. Celliers, G. W. Collins, K. S. Budil, N. C. Holmes, T. W. Barbee Jr., B. A. Hammel, J. D. Kilkenny, R. J. Wallace, M. Ross, R. Cauble, A. Ng, and G. Chiu. Absolute Equation of State Measurements on Shocked Liquid Deuterium up to 200 GPa (2 Mbar). *Phys. Rev. Lett.*, 78(3):483–486, January 1997.

[20] Lynn M. Barker. The development of the VISAR, and its use in shock compression science. *AIP Conference Proceedings*, 505(1):11–18, April 2000.

[21] A. Lazicki, J.R. Rygg, F. Coppari, R. Smith, D. Fratanduono, R.G. Kraus, G.W. Collins, R. Briggs, D.G. Braun, D.C. Swift, and J.H. Eggert. X-Ray Diffraction of Solid Tin to 1.2 TPa. *Phys. Rev. Lett.*, 115(7):075502, August 2015.

[22] S. J. Gurman, N. Binsted, and I. Ross. A rapid, exact curved-wave theory for EXAFS calculations. *J. Phys. C: Solid State Phys.*, 17(1):143–151, January 1984.

[23] Y. Ping, F. Coppari, D. G. Hicks, B. Yaakobi, D. E. Fratanduono, S. Hamel, J. H. Eggert, J. R. Rygg, R. F. Smith, D. C. Swift, D. G. Braun, T. R. Boehly, and G. W. Collins. Solid Iron Compressed Up to 560 GPa. *Physical Review Letters*, 111(6), August 2013.

[24] J. E. Miller, T. R. Boehly, A. Melchior, D. D. Meyerhofer, P. M. Celliers, J. H. Eggert, D. G. Hicks, C. M. Sorce, J. A. Oertel, and P. M. Emmel. Streaked optical pyrometer system for laser-driven shock-wave experiments on OMEGA. *Review of Scientific Instruments*, 78(3):034903, March 2007.

[25] Andrew W. Obst, Keith R. Alrick, William W. Anderson, Konstantinos Boboridis, William T. Buttler, Steve K. Lamoreaux, Bruce R. Marshall, Stefanie L. Montgomery, Jeremy R. Payton, and Mark D. Wilke. Ellipsometry in the Study of Dynamic Material Properties. *AIP Conference Proceedings*, 620(1):1247–1250, July 2002.

[26] Ya B. Zeldovich and Yu P. Raizer. *Physics of Shock Waves and High-Temperature Hydrodynamic Phenomena*. Courier Corporation, August 2012. Google-Books-ID: PULCAgAAQBAJ.

[27] D. K Bradley, J. H. Eggert, D. G. Hicks, P. M. Celliers, S. J. Moon, R. C. Cauble, and G. W. Collins. Shock Compressing Diamond to a Conducting Fluid. *Physical Review Letters*, 93(19), November 2004.

[28] Marius Millot. Identifying and discriminating phase transitions along decaying shocks with line imaging Doppler interferometric velocimetry and streaked optical pyrometry. *Physics of Plasmas*, 23(1):014503, January 2016.

[29] N. C. Dang, C. A. Bolme, D. S. Moore, and S. D. McGrane. Femtosecond Stimulated Raman Scattering Picosecond Molecular Thermometry in Condensed Phases. *Phys. Rev. Lett.*, 107(4):043001, July 2011.

[30] Bernhard Schrader. *Infrared and Raman Spectroscopy: Methods and Applications*. John Wiley & Sons, September 2008. Google-Books-ID: 9LOcQs2MSesC.

[31] D S Moore and S D McGrane. Raman temperature measurement. *Journal of Physics: Conference Series*, 500(19):192011, May 2014.

[32] P.H. Fowler. Report on Remote Temperature Measurement by Neutrons. Technical report, Bristol University, Department of Physics, 1984.

[33] J. Mayers, G. Baciocco, and A. C. Hannon. Temperature measurement by neutron resonance radiography. *Nuclear Instruments and Methods in Physics Research Section A: Accelerators, Spectrometers, Detectors and Associated Equipment*, 275(2):453–459, 1989.

[34] V. W. Yuan, J. David Bowman, D. J. Funk, G. L. Morgan, R. L. Rabie, C. E. Ragan, J. P. Quintana, and H. L. Stacy. Shock Temperature Measurement Using Neutron Resonance Spectroscopy. *Physical Review Letters*, 94(12), March 2005.

[35] K. L. Lancaster, S. Karsch, H. Habara, F. N. Beg, E. L. Clark, R. Freeman, M. H. Key, J. A. King, R. Kodama, K. Krushelnick, K. W. D. Ledingham, P. McKenna, C. D. Murphy, P. A. Norreys, R. Stephens, C. Steckl, Y. Toyama, M. S. Wei, and M. Zepf. Characterization of 7Li(p,n)7Be neutron yields from laser produced ion beams for fast neutron radiography. *Physics of Plasmas*, 11(7):3404–3408, July 2004.

[36] D.P. Higginson, L. Vassura, M.M. Gugiu, P. Antici, M. Borghesi, S. Brauckmann, C. Diouf, A. Green, L. Palumbo, H. Petrascu, S. Sofia, M. Stardubtsev, O. Willi, S. Kar, F. Negoita, and J. Fuchs. Temporal Narrowing of Neutrons Produced by High-Intensity Short-Pulse Lasers. *Physical Review Letters*, 115(5), July 2015.

[37] William J. Murphy, Andrew Higginbotham, Justin S. Wark, and Nigel Park. Molecular dynamics simulations of the Debye-Waller effect in shocked copper. *Physical Review B*, 78(1), July 2008.

[38] N.W. Ashcroft and N.D. Mermin. *Solid State Physics*. Saunders College, 1976.

[39] Scott M. Woodley and Richard Catlow. Crystal structure prediction from first principles. *Nature Materials*, 7(12):937–946, December 2008.

[40] L. M. Barker and R. E. Hollenbach. Shock wave study of the phase transition in iron. *Journal of Applied Physics*, 45(11):4872–4887, November 1974.

[41] Kai Kadau, Timothy C. Germann, Peter S. Lomdahl, Robert C. Albers, Justin S. Wark, Andrew Higginbotham, and Brad Lee Holian. Shock Waves in Polycrystalline Iron. *Physical Review Letters*, 98(13), March 2007.

[42] Guoyin Shen, Ho-kwang Mao, Russell J. Hemley, Thomas S. Duffy, and Mark L. Rivers. Melting and crystal structure of iron at high pressures and temperatures. *Geophysical Research Letters*, 25(3):373–376, 1998.

[43] William H. Beamer and Charles R. Maxwell. The Crystal Structure of Polonium. *The Journal of Chemical Physics*, 14(9):569–569, September 1946.

[44] Anthony Kelly and G.W. Groves. *Crystallography and Crystal Defects*. Wiley, John & Sons, 1970.

[45] D Hull and D.J. Bacon. *Introduction to Dislocations*. Butterworth-Heinemann, 2011.

[46] Marc A. Meyers. A mechanism for dislocation generation in shock-wave deformation. *Scripta Metallurgica*, 12(1):21–26, January 1978.

[47] Zhiwei Shan, E. A. Stach, J. M. K. Wiezorek, J. A. Knapp, D. M. Follstaedt, and S. X. Mao. Grain Boundary-Mediated Plasticity in Nanocrystalline Nickel. *Science*, 305(5684):654–657, July 2004.

[48] B. E. Warren. *X-Ray Diffraction*. Dover, 1969.

[49] H.J. Bunge. *Texture Analysis in Materials Science: Mathematical Methods*. Butterworth & Co., 1982.

[50] R.A. Vandermeer and J.C. Ogle. The Development of Preferred Orientations in Cold-Rolled Niobium (Columbium). *TRANSACTIONS OF THE METALLURGICAL SOCIETY OF AIME*, 242:1317–1326, July 1968.

[51] J. D. Watson and F. H. C. Crick. Molecular Structure of Nucleic Acids: A Structure for Deoxyribose Nucleic Acid | Nature. *Nature*, 171(4356):737 – 738, April 1953.

[52] Hans Frauenfelder, Gregory A. Petsko, and Demetrius Tsernoglou. Temperature-dependent X-ray diffraction as a probe of protein structural dynamics. *Nature*, 280(5723):558–563, August 1979.

[53] S. E. Sherman, D. Gibson, A. H. Wang, and S. J. Lippard. X-ray structure of the major adduct of the anticancer drug cisplatin with DNA: cis-[Pt(NH3)2(d(pGpG))]. *Science*, 230(4724):412–417, October 1985.

[54] G. Ribrik, J. Gubicza, and T. Ungr. Correlation between strength and microstructure of ball-milled AlMg alloys determined by X-ray diffraction. *Materials Science and Engineering: A*, 387-389:343–347, December 2004.

[55] Russell J. Hemley, Ho-kwang Mao, Guoyin Shen, James Badro, Philippe Gillet, Michael Hanfland, and Daniel Husermann. X-ray Imaging of Stress and Strain of Diamond, Iron, and Tungsten at Megabar Pressures. *Science*, 276(5316):1242–1245, May 1997.

[56] Jue Wang, Federica Coppari, Raymond F. Smith, Jon H. Eggert, Amy E. Lazicki, Dayne E. Fratanduono, J. Ryan Rygg, Thomas R. Boehly, Gilbert W. Collins, and Thomas S. Duffy. X-ray diffraction of molybdenum under shock compression to 450 GPa. *Physical Review B*, 92(17), November 2015.

[57] R. Briggs, M.G. Gorman, A.L. Coleman, R.S. McWilliams, E.E. McBride, D. McGonegle, J.S. Wark, L. Peacock, S. Rothman, S.G. Macleod, C.A. Bolme, A.E. Gleason, G.W. Collins, J.H. Eggert, D.E. Fratanduono, R.F. Smith, E. Galtier, E. Granados, H.J. Lee, B. Nagler, I. Nam, Z. Xing, and M.I. McMahon. Ultrafast X-Ray Diffraction Studies of the Phase Transitions and Equation of State of Scandium Shock Compressed to 82 GPa. *Phys. Rev. Lett.*, 118(2):025501, January 2017.

[58] F. Seiboth, L. B. Fletcher, D. McGonegle, S. Anzellini, L. E. Dresselhaus-Cooper, M. Frost, E. Galtier, S. Goede, M. Harmand, H. J. Lee, A. L. Levitan, K. Miyanishi, B. Nagler, I. Nam, N. Ozaki, M. Rdel, A. Schropp, C. Spindloe, P. Sun, J. S. Wark, J. Hastings, S. H. Glenzer, and E. E. McBride. Simultaneous 8.2 keV phase-contrast imaging and 24.6 keV

X-ray diffraction from shock-compressed matter at the LCLS. *Applied Physics Letters*, 112(22):221907, May 2018.

[59] Agns Dewaele, Mohamed Mezouar, Nicolas Guignot, and Paul Loubeyre. Melting of lead under high pressure studied using second-scale time-resolved x-ray diffraction. *Physical Review B*, 76(14), October 2007.

[60] J. M. Foster, A. J. Comley, G. S. Case, P. Avraam, S. D. Rothman, A. Higginbotham, E. K. R. Floyd, E. T. Gumbrell, J. J. D. Luis, D. McGonegle, N. T. Park, L. J. Peacock, C. P. Poulter, M. J. Suggit, and J. S. Wark. X-ray diffraction measurements of plasticity in shock-compressed vanadium in the region of 1070 GPa. *Journal of Applied Physics*, 122(2):025117, July 2017.

[61] W J Murphy, A Higginbotham, G Kimminau, B Barbrel, E M Bringa, J Hawreliak, R Kodama, M Koenig, W McBarron, M A Meyers, B Nagler, N Ozaki, N Park, B Remington, S Rothman, S M Vinko, T Whitcher, and J S Wark. The strength of single crystal copper under uniaxial shock compression at 100 GPa. *Journal of Physics: Condensed Matter*, 22(6):065404, February 2010.

[62] P. Debye. Interferenz von Rntgenstrahlen und Wrmebewegung. *Annalen der Physik*, 348(1):49–92, January 1913.

[63] M. Wilkens. The determination of density and distribution of dislocations in deformed single crystals from broadened X-ray diffraction profiles. *Physica status solidi (a)*, 2(2):359–370, 1970.

[64] M. Wilkens. Diffraction line broadening of crystals containing small-angle boundaries. *Journal of applied crystallography*, 12(1):119–125, 1979.

[65] M. Wilkens. ber die Rntgenstreuung an Kristallen mit Versetzungen III. Die asymptotische Darstellung von Debye-Scherrer-Linienprofilen. *phys. stat. sol. (b)*, 3(9):1718–1737, January 1963.

[66] M. Wilkens. X-ray line broadening and mean square strains of straight dislocations in elastically anisotropic crystals of cubic symmetry. *phys. stat. sol. (a)*, 104(1):K1–K6, November 1987.

[67] John Arthur Simmons, Roland De Wit, and R. Bullough. *Fundamental aspects of dislocation theory: conference proceedings, National Bureau of Standards, April 21-25, 1969*, volume 1. US National Bureau of Standards, 1970.

[68] H. Grubmller, H. Heller, A. Windemuth, and K. Schulten. Generalized Verlet Algorithm for Efficient Molecular Dynamics Simulations with Long-range Interactions. *Molecular Simulation*, 6(1-3):121–142, March 1991.

[69] Chris J. Pickard and R. J. Needs. Aluminium at terapascal pressures. *Nat Mater*, 9(8):624–627, August 2010.

[70] E. M. Bringa, J. U. Cazamias, P. Erhart, J. Stlken, N. Tanushev, B. D. Wirth, R. E. Rudd, and M. J. Caturla. Atomistic shock Hugoniot simulation of single-crystal copper. *Journal of Applied Physics*, 96(7):3793–3799, October 2004.

[71] David McGonegle, Despina Milathianaki, Bruce A. Remington, Justin S. Wark, and Andrew Higginbotham. Simulations of *in situ* x-ray diffraction

from uniaxially compressed highly textured polycrystalline targets. *Journal of Applied Physics*, 118(6):065902, August 2015.

[72] Giles Kimminau, Bob Nagler, Andrew Higginbotham, William J Murphy, Nigel Park, James Hawreliak, Kai Kadau, Timothy C Germann, Eduardo M Bringa, Daniel H Kalantar, Hector E Lorenzana, Bruce A Remington, and Justin S Wark. Simulating picosecond x-ray diffraction from shocked crystals using post-processing molecular dynamics calculations. *Journal of Physics: Condensed Matter*, 20(50):505203, December 2008.

[73] D. H. Tsai and R. A. MacDonald. Second sound in a solid under shock compression. *Journal of Physics C: Solid State Physics*, 6(8):L171, 1973.

[74] Murray S. Daw and Michael I. Baskes. Embedded-atom method: Derivation and application to impurities, surfaces, and other defects in metals. *Physical Review B*, 29(12):6443, 1984.

[75] D. J. Evans and B. L. Holian. The NoseHoover thermostat. *J. Chem. Phys.*, 83(8):4069–4074, October 1985.

[76] R. Ravelo, B. Holian, T. Germann, and P. Lomdahl. Constant-stress Hugoniostat method for following the dynamical evolution of shocked matter. *Physical Review B*, 70(1), July 2004.

[77] Steve Plimpton. Fast Parallel Algorithms for ShortRange Molecular Dynamics. *Journal of Computational Physics*, 117:1 – 19, March 1995.

[78] Y. Mishin, M. J. Mehl, D. A. Papaconstantopoulos, A. F. Voter, and J. D. Kress. Structural stability and lattice defects in copper: *Ab initio* ,

tight-binding, and embedded-atom calculations. *Physical Review B*, 63(22), May 2001.

[79] M. E. Straumanis and L. S. Yu. Lattice Parameters, Densities, Expansion Coefficients and Perfection of Structure of Cu and of Cu-In a Phase. *Acta Crystallographica*, 25:676, April 1969.

[80] Michael R. Fellinger, Hyoungki Park, and John W. Wilkins. Force-matched embedded-atom method potential for niobium. *Physical Review B*, 81(14), April 2010.

[81] James W. Edwards, Rudolph Speiser, and Herrick L. Johnston. High Temperature Structure and Thermal Expansion of Some Metals as Determined by XRay Diffraction Data. I. Platinum, Tantalum, Niobium, and Molybdenum. *Journal of Applied Physics*, 22(4):424–428, April 1951.

[82] B. E. Warren. X-ray studies of deformed metals. *Progress in metal physics*, 8:147–202, 1959.

[83] Zheng-Hua Fang and Li-Rong Chen. A simplified treatment to calculate the melting temperature of metals under a high pressure. *Journal of Physics: Condensed Matter*, 6(35):6937, 1994.

[84] C. V. Pandya, P. R. Vyas, T. C. Pandya, and V. B. Gohel. Volume variation of Gruneisen parameters offcc transition metals. *Bull Mater Sci*, 25(1):63–67, February 2002.

[85] J. Ramakrishnan, Reinhard Boehler, Gary H. Higgins, and George C. Kennedy. Behavior of Grneisen's parameter of some metals at high pressures. *J. Geophys. Res.*, 83(B7):3535–3538, July 1978.

[86] John M. Walsh, Melvin H. Rice, Robert G. McQueen, and Frederick L. Yarger. Shock-wave compressions of twenty-seven metals. Equations of state of metals. *Physical Review*, 108(2):196, 1957.

[87] P. A. Flinn, G. M. McManus, and J. A. Rayne. Effective X-ray and Calorimetric Debye Temperature for Copper. *Phys. Rev.*, 123(3), August 1961.

[88] Yongtao Zou, Xintong Qi, Xuebing Wang, Ting Chen, Xuefei Li, David Welch, and Baosheng Li. High-pressure behavior and thermoelastic properties of niobium studied by in situ x-ray diffraction. *Journal of Applied Physics*, 116(1):013516, July 2014.

[89] Takemura Kenichi and Anil K. Singh. High-pressure equation of state for Nb with a helium-pressure medium: Powder x-ray diffraction experiments. *Physical Review B*, 73(22), June 2006.

[90] E. C. Bain and N. Y. Dunkirk. The Nature of Martensite. *Trans. AIME*, 70:25–35, 42, 45, 1924.

[91] L. Velterop, R. Delhez, Th. H. de Keijser, E. J. Mittemeijer, and D. Reefman. X-ray diffraction analysis of stacking and twin faults in f.c.c. metals: a revision and allowance for texture and non-uniform fault probabilities. *Journal of Applied Crystallography*, 33(2):296–306, April 2000.

[92] J. D. Honeycutt and H. C. Andersen. Molecular dynamics study of melting and freezing of small Lennard-Jones clustersy. *The Journal of Physical Chemistry*, 91(19):4950 – 4963, January 1987.

[93] Alexander Stukowski. Visualization and analysis of atomistic simulation data with OVITOthe Open Visualization Tool. *Modelling Simul. Mater. Sci. Eng.*, 18(1):015012, December 2009.

[94] Cynthia L. Kelchner, S. J. Plimpton, and J. C. Hamilton. Dislocation nucleation and defect structure during surface indentation. *Physical review B*, 58(17):11085, 1998.

[95] Kai Kadau, Timothy C. Germann, Peter S. Lomdahl, and Brad Lee Holian. Atomistic simulations of shock-induced transformations and their orientation dependence in bcc Fe single crystals. *Physical Review B*, 72(6), August 2005.

[96] Alexander Stukowski and Karsten Albe. Extracting dislocations and non-dislocation crystal defects from atomistic simulation data. *Modelling and Simulation in Materials Science and Engineering*, 18(8):085001, December 2010.

[97] M. van Thiel, T Michels, C MacNaughton, J. Shaner, and E. Salinas. COMPENDIUM OF SHOCK WAVE DATA. 1 - 3:109, June 1977.

[98] Stanley P. Marsh. *LASL Shock Hugoniot Data*. University of California Press, 1980. Google-Books-ID: FVaEv0TvJ‿gC.

[99] A. Higginbotham, P. G. Stubley, A. J. Comley, J. H. Eggert, J. M. Foster, D. H. Kalantar, D. McGonegle, S. Patel, L. J. Peacock, S. D. Rothman, R. F.

Smith, M. J. Suggit, and J. S. Wark. Inelastic response of silicon to shock compression. *Scientific Reports*, 6:24211, April 2016.

[100] Nicholas Hopps, Colin Danson, Stuart Duffield, David Egan, Stephen Elsmere, Mark Girling, Ewan Harvey, David Hillier, Michael Norman, Stefan Parker, Paul Treadwell, David Winter, and Thomas Bett. Overview of laser systems for the Orion facility at the AWE. *Applied Optics*, 52(15):3597, May 2013.

[101] Nicholas Hopps, Kevin Oades, Jim Andrew, Colin Brown, Graham Cooper, Colin Danson, Simon Daykin, Stuart Duffield, Ray Edwards, David Egan, Stephen Elsmere, Steve Gales, Mark Girling, Edward Gumbrell, Ewan Harvey, David Hillier, David Hoarty, Colin Horsfield, Steven James, Alex Leatherland, Stephen Masoero, Anthony Meadowcroft, Michael Norman, Stefan Parker, Stephen Rothman, Michael Rubery, Paul Treadwell, David Winter, and Thomas Bett. Comprehensive description of the Orion laser facility. *Plasma Physics and Controlled Fusion*, 57(6):064002, June 2015.

[102] Y. Kato, K. Mima, N. Miyanaga, S. Arinaga, Y. Kitagawa, M. Nakatsuka, and C. Yamanaka. Random Phasing of High-Power Lasers for Uniform Target Acceleration and Plasma-Instability Suppression. *Phys. Rev. Lett.*, 53(11):1057–1060, September 1984.

[103] D. L. Matthews, E. M. Campbell, N. M. Ceglio, G. Hermes, R. Kauffman, L. Koppel, R. Lee, K. Manes, V. Rupert, V. W. Slivinsky, R. Turner, and F. Ze. Characterization of laserproduced plasma xray sources for use in xray radiography. *Journal of Applied Physics*, 54(8):4260–4268, August 1983.

[104] Guang-Yue Hu, Jian Zheng, Bai-fei Shen, An-le Lei, Shen-Ye Liu, Ji-Yan Zhang, Jia-Min Yang, Yong-Kun Ding, Xin Hu, Yi-Xiang Huang, Hua-Bing Du, Rong-Qing Yi, and Zhi-zhan Xu. Characterization of a multi-keV x-ray source produced by nanosecond laser irradiation of a solid target: The influence of laser focus spot and target thickness. *Physics of Plasmas*, 15(2):023103, February 2008.

[105] John Lindl. Development of the indirectdrive approach to inertial confinement fusion and the target physics basis for ignition and gain. *Physics of Plasmas*, 2(11):3933–4024, November 1995.

[106] C. D. Bentley, R. D. Edwards, J. E. Andrew, S. F. James, M. D. Gardner, A. J. Comley, K. Vaughan, C. J. Horsfield, M. S. Rubery, S. D. Rothman, S. Daykin, S. J. Masoero, J. B. Palmer, A. L. Meadowcroft, B. M. Williams, E. T. Gumbrell, J. D. Fyrth, C. R. D. Brown, M. P. Hill, K. Oades, M. J. Wright, B. A. Hood, and P. Kemshall. ORION laser target diagnostics. *Review of Scientific Instruments*, 83(10):10D732, October 2012.

[107] G. Fiksel, F. J. Marshall, C. Mileham, and C. Stoeckl. Note: Spatial resolution of Fuji BAS-TR and BAS-SR imaging plates. *Review of Scientific Instruments*, 83(8):086103, August 2012.

[108] CXRO X-Ray Interactions With Matter.

[109] B. L. Henke, E. M. Gullikson, and J. C. Davis. X-Ray Interactions: Photoabsorption, Scattering, Transmission, and Reflection at E = 50-30,000

eV, Z = 1-92. *Atomic Data and Nuclear Data Tables*, 54(2):181–342, July 1993.

[110] David D. Clark, Robert Aragonez, Thomas Archuleta, Valerie Fatherley, Albert Hsu, Justin Jorgenson, Danielle Mares, John Oertel, Kevin Oades, Paul Kemshall, Philip Thomas, Trevor Young, and Neal Pederson. A new gated x-ray detector for the Orion laser facility. In *Target Diagnostics Physics and Engineering for Inertial Confinement Fusion*, volume 8505, page 85050K. International Society for Optics and Photonics, October 2012.

[111] D. F. Martin and A. L. Meadowcroft. A high-energy resolution x-ray spectrometer with interchangeable detectors (HEX-ID) for short-pulse laser-plasma experiments. In *2011 Abstracts IEEE International Conference on Plasma Science*, pages 1–1, June 2011.

[112] Frdric Girard. Review of laser produced multi-keV X-ray sources from metallic foils, cylinders with liner, and low density aerogels. *Physics of Plasmas*, 23(4):040501, April 2016.

[113] D. Babonneau, M. Primout, F. Girard, J.-P. Jadaud, M. Naudy, B. Villette, S. Depierreux, C. Blancard, G. Faussurier, K. B. Fournier, L. Suter, R. Kauffman, S. Glenzer, M. C. Miller, J. Grn, and J. Davis. Efficient multi-keV X-ray sources from laser-exploded metallic thin foils. *Physics of Plasmas*, 15(9):092702, September 2008.

[114] Anthony Meadowcroft. Analysis of HEX-ID spectrometer data for Academic Access campaign (York, 190118), March 2018.

[115] Jon T. Larsen and Stephen M. Lane. HYADESA plasma hydrodynamics code for dense plasma studies. *Journal of Quantitative Spectroscopy and Radiative Transfer*, 51(1):179–186, January 1994.

[116] Tane P. Remington, Bruce A. Remington, Eric N. Hahn, and Marc A. Meyers. Deformation and failure in extreme regimes by high-energy pulsed lasers: A review. *Materials Science and Engineering: A*, 688:429–458, March 2017.

[117] B. R. Maddox, H. S. Park, B. A. Remington, N. Izumi, S. Chen, C. Chen, G. Kimminau, Z. Ali, M. J. Haugh, and Q. Ma. High-energy x-ray backlighter spectrum measurements using calibrated image plates. *Review of Scientific Instruments*, 82(2):023111, February 2011.

[118] M Thoms. The dynamic range of X-ray imaging with image plates. *Nuclear Instruments and Methods in Physics Research A*, 389:437–440, October 1996.

[119] Dierk Raabe and K. Lcke. Rolling and Annealing Textures of BCC Metals. *Materials Science Forum*, 157-162:597–610, May 1994.